ISTANBUL TECHNICAL UNIVERSITY ★ GRADUATE SCHOOL

INVENTORY OF MASSWASTING AND SEDIMENT TRANSPORT FEATURES ON THE LIGURIAN MARGIN

M.Sc. THESIS

Rashid AHMADOV

Department of Geological Engineering

Geological Engineering Programme

JUNE 2022

ISTANBUL TECHNICAL UNIVERSITY ★ GRADUATE SCHOOL

INVENTORY OF MASSWASTING AND SEDIMENT TRANSPORT FEATURES ON THE LIGURIAN MARGIN

M.Sc. THESIS

Rashid AHMADOV
(505181325)

Department of Geological Engineering

Geological Engineering Programme

Thesis Advisor: Prof. Dr. Kürşad Kadir Eriş
Thesis Co-Advisor: Prof. Dr. Volkhard Spieß

JUNE 2022

ISTANBUL TEKNİK ÜNİVERSİTESİ ★ LİSANSÜSTÜ EĞİTİM ENSTİTÜSÜ

LİGURYA MARJİNİNDEKİ KİTLE HAREKETLERİNİN ENVANTERİ VE SEDİMENT TAŞINMA ÖZELLİKLERI

YÜKSEK LİSANS TEZİ

Rashid AHMADOV
(505181325)

Jeoloji Mühendisliği Anabilim Dalı
Jeoloji Mühendisliği Programı

Tez Danışmanı: Prof. Dr. Kürşad Kadir Eriş
Eş Danışman: Prof. Dr. Volkhard Spieß

HAZIRAN 2022

Rashid Ahmadov, a M.Sc. student of ITU Graduate School of Science Engineering and Technology student ID 505181325, successfully defended the thesis/dissertation entitled "INVENTORY OF MASSWASTING AND SEDIMENT TRANSPORT FEATURES ON THE LIGURIAN MARGIN", which he prepared after fulfilling the requirements specified in the associated legislations, before the jury whose signatures are below.

Thesis Advisor :	**Prof. Dr. Name SURNAME** İstanbul Technical University	.....
Co-advisor :	**Prof.Dr. Name SURNAME** ..... University	.....
Jury Members :	**Prof. Dr. Name SURNAME** Istanbul Technical University	.....
	Prof. Dr. Name SURNAME ..... University	.....
	Prof. Dr. Name SURNAME ..... University	.....
	Prof. Dr. Name SURNAME ..... University	.....
	Prof. Dr. Name SURNAME ..... University	.....

Date of Submission : 24 May 2022
Date of Defense : 28 June 2022

In memory of the victims of "Gunashli" oilfield disaster,

FOREWORD

First of all, I am thankful to my family for their belief in me throughout my education. Their continuous support to me was what sustained me this far.

I would like to thank both of my advisors Prof. Dr. Kürşad Kadir Eriş and Prof. Dr. Volkhard Spieß, for their invaluable support and time spent throughout this study. Their patience, motivation, and enthusiasm to share their experience, knowledge, and resources helped me in all the stages of my research.

Also I want to thank all other members of the MTU (Marine Technology / Environmental Research) working group from University of Bremen for continuous support and provided alternate perspectives.

June 2022

Rashid Ahmadov

(Graduate student)

TABLE OF CONTENTS

List of tables

List of figures

INVENTORY OF MASSWASTING AND SEDIMENT TRANSPORT FEATURES ON THE LIGURIAN MARGIN

SUMMARY

The Ligurian margin (NW-Mediterranean Sea) is a seismically and tectonically active margin, and lots of mass wasting processes and submarine landslides are known on the deeper slope. Based on multichannel seismic reflection data from the expedition of M73/1, LIMA-LAMO (Ligurian Margin Landslide Measurements & Observatory) 2007, this study attempts to have a better idea of the underground structure of the deepwater area of the Ligurian Margin, including the deeper slope (1500-2000 m water depth) west of the Var Canyon with several scars, landslide, and the Var Canyon zone with its channels, terraces, and flanks in down to roughly 2500 m water depth.

The region's high seismic activity is considered a potential trigger mechanism for further slope instabilities. The study area is a geologically complex region shaped by numerous canyons and steep-sided gully systems that create rough and irregular bathymetry. The obtained seismic data has several processing challenges regarding strong multiples, velocity analysis, and seismic migration. Therefore, a tailored processing flow has been developed that optimizes the attenuation of noise and allows a reliable migration of the seismic data.

The seismic-stratigraphic analysis and facies description of the processed 17 seismic lines allowed us to understand the connection between the deposits and deeper areas and the original deposits where the failure masses were coming from. There has been no study before this thesis about the collected deepwater survey data from the M73/1 2007 expedition. In brief, these seismic profiles can be used for future scientific works, and there is no need to repeat processing.

In terms of the interpretation part, each seismic unit's thickness map in s TWT (two-way traveltime) and identified surfaces depth map in s TWT were prepared and analyzed during the facies description. Then, collected mass wasting features and the processes were discussed.

It is well known that sea-level fluctuations have deeply influenced the stratigraphy of the region. However, at present, this study is not able to assign a geologic age to the deposition of sequences in relation to sea-level changes. The narrow continental shelf and steep gradients have minimized the effect of sea-level change. A more precise, extensive, and dense survey is needed to evaluate the event in the region.

LİGURYA MARJİNİNDEKİ KİTLE HAREKETLERİNİN ENVANTERİ VE SEDİMENT TAŞINMA ÖZELLİKLERI

ÖZET

Ligurya Marjini (KB-Akdeniz) sismik ve tektonik olarak aktif bir alandır, marjinin derin yamaçlarında çok sayıda kitle hareketi ve denizaltı heyelanları olduğu bilinmektedir. M73/1, LIMA-LAMO (Ligurya Marjı Heyelan Ölçümleri ve Gözlemevi) 2007 keşif gezisinden elde edilen çok kanallı sismik yansıma verileri ile Ligurya Marjininin derin alanının yeraltı yapısı hakkında daha iyi bir fikir edinme için bu çalışma yapılmıştır. Araştırma alanı Var Kanyonu'nun batısındaki derin eğimli bölgeyi (1500-2000 m su derinliği) ve yaklaşık 2500 m su derinliğine kadar inen Var Kanyon bölgesini kapsamaktadır.

Bölgenin sismik olarak çok fazla aktif olması, şev instabilitesi için potansiyel bir tetikleyici mekanizma olduğu kabul edilmektedir. Çalışma alanı, kaba ve düzensiz batimetri oluşturan çok sayıda kanyon ve dik kenarlı sel yatağı sistemleri tarafından şekillendirilmiş, jeolojik olarak kompleks bir bölgedir. Elde edilen sismik verilerin işlenmesi zamanı çeşitli sorunlar ile karşı karşıya kalınmıştır. Bu nedenle, gürültüleri sismik verilerden temizlenmesine yardım eden ve verilerin güvenilir bir şekilde işlenmesini sağlayan özel bir sismik veri işleme akışı geliştirilmiştir.

17 sismik yansıma verisinin sismik-stratigrafik analizi ve fasiyes tanımı, derin alanlardaki çökeller ile çökmüş kütlelerin geldiği orijinal çökeller arasındaki bağlantıyı anlamamızı sağladı. 2007 de yapılmış bu keşif gezisinden toplanmış derin deniz sismik verileri üzerinde daha önce herhangi bir çalışma yapılmamıştır. Kısacası, işlenmiş bu sismik yansıma profilleri gelecekteki bilimsel çalışmalar için kullanılabilir.

Yorum kısmında, fasiyes tanımlaması sırasında her bir sismik birimin kalınlık haritası ve tespit edilen yüzeylerin derinlik haritası hazırlanmıştır. En sonda deniz altı toprak kayması veya heyelan olduğu düşünülmüş veriler ve buna sebep olan süreçler tartışılmıştır.

Deniz seviyesi değişimleri bölgenin stratigrafisini derinden etkilediği iyi bilinmektedir. Bununla birlikte, şu anda, bu çalışma, deniz seviyesi değişimlerini baz alarak ilgili sismik birimlere jeolojik bir yaş tayin edememektedir. Dar kıta sahanlığı ve aşırı dik eğimler, deniz seviyesi değişiminin etkisini en aza indirmiştir. Bölgedeki deniz seviyesi değişimleri olayını daha iyi değerlendirmek için kapsamlı ve yoğun bir çalışmaya ihtiyaç vardır.

1. INTRODUCTION

1.1. Motivation

Submarine landslides are expected on inclined areas of the seafloor, often in circumstances where weak geologic layers such as fine-grained sediment or fractured rock are subjected to strong environmental stresses induced by earthquakes, large storm waves, or high internal pore pressures. Submarine landslides are primary mechanisms through which sediments are transported along the continental slope to the deeper ocean.

Submarine landslides can cause tsunamis and impact coastal and offshore infrastructures. In 1979 a catastrophic event left 23 people dead and caused considerable loss of material goods; during the construction of a new harbor adjacent to the International Airport of Nice, France, part of the new land reclaimed collapsed into the ocean generating a 2-2.5 m tsunami and the mass movement of approximately 8 x 106 m3 of sediments (Migeon et al. 2006). Understanding the mechanisms behind mass wasting processes is necessary to operate the results for better hazard assessments. Submarine landslides occur in all geological settings and are generated in water depths from the shoreline to the open slope (Förster 2011). The existing knowledge about the mechanics and evolution of submarine mass wasting processes and their related trigger mechanisms comes from several case studies, international campaigns, and drilling programs.

Nevertheless, more research has to be done to understand the process involved with the phenomenon. The occurrence of this event in 1979 has forced scientists' attention, leading to extensive research in the area. The present work contributes to this cause and provides evidence to test hypotheses on triggering mechanisms that could have occurred during the 1979 Nice airport event. During the Cruise M73/1 "LIMA-LAMO" the German vessel R/V METEOR surveyed the western Ligurian Margin offshore the city off Nice, France.

Among the datasets gathered during this cruise, a collection of bathymetry data from EM710 and EM120 Kongsberg echosounders and seismic data from a 2*0.1 L custom-made Micro-GI Gun and a 2*1.7 L GI Gun were used for this master thesis dissertation. A very high resolution data provided by GI Gun was collected from 1)the deeper slope, 1500-2000 m water depth, west of the Var Canyon with several landslide scars; 2) the Var Canyon region with its terraces, flanks, and channels in down to the about 2500 m water depth.

1.2. Landslides – General Aspects

Landslides can occur on land as well as under the water and are quite frequent. Along many similarities between landslides above and below sea level, they show differences as well. Submarine landslides are often more extensive and may involve larger volumes of material, when compared to subaerial landslides (Locat, 2001). This study will mainly focus on submarine landslides.

1.2.1 Mass wasting processes

An essential factor in the transportation and deposition of sediments in deeper water environments is mass wasting or gravity-driven processes occurring mainly on continental margins and island flanks. While continental margins are typically characterized by a low slope gradient with gentle topography, ocean islands such as the Canary Islands have great relief with steep slopes up to 15° (Masson et al. 2006). Various classifications of the different mass wasting processes have been conducted, and several end-members have been identified as slides, slumps, debris flows, and turbidity currents (Figure 1.1).

1.2.2 Slides

A slide - is a coherent mass of sediment that moves along a planar glide plane and shows no internal deformation (Figure 1.1). Slides represent translational movement. Submarine slides can travel hundreds of kilometers. For example, the run-out distance of Nuuanu Slide, offshore Hawaii, is 230 km (Normark et al. 1993). Submarine slides are common in fjords because the submerged sides of glacial valleys are steep and because the rate of sedimentation is high due to sediment-laden rivers that drain glaciers into fjords (Shanmugam 2006).

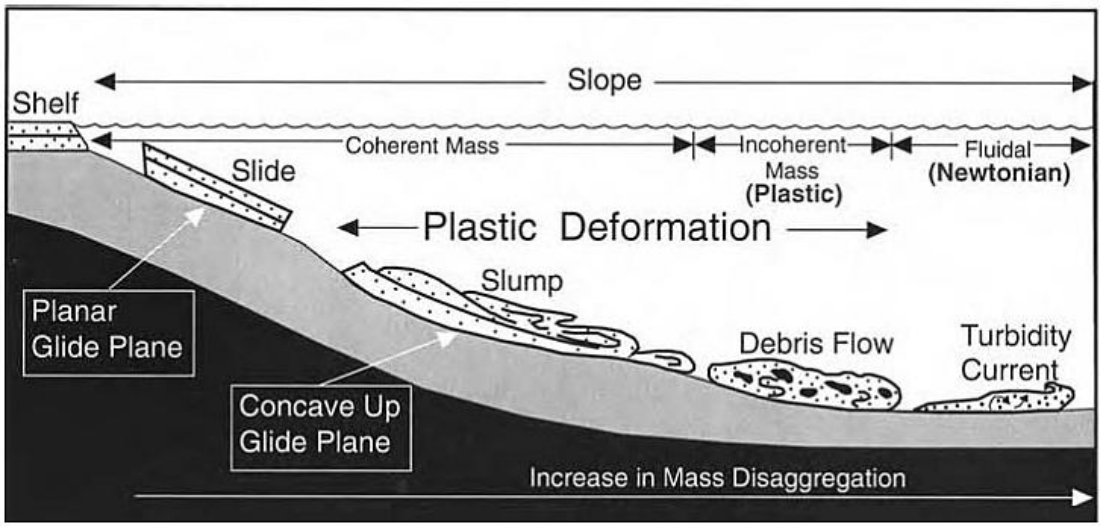

Figure 1.1 Schematic diagram showing four common types of gravity-driven processes that transport sediment into deep-water environments (After Shanmugam 2006)).

1.2.3 Slumpes

A slump is a coherent mass of sediment that moves on a concave-up glide plane and undergoes rotational movements causing internal deformation (Figure 1.1). In practice, distinguishing slides from slumps can be difficult. Slumps present basal zones of shearing,

upslope areas with tensional faults, and downslope edges with compressional folding or thrusting (Shanmugam 2006).

1.2.4 Sediment flows

Some terms have been used to describe processes that could be considered a transitional type between slumps and debris flows. Terms such as flow slide have been used for high-velocity subaerial processes. A debris slide is used when a slow-moving mass breaks up into smaller blocks as it advances, whereas a fast-moving mass that breaks up into smaller blocks as it advances is called a debris avalanche. Catastrophic (fast-moving) debris flows are called sturzstrom, the term creep refers to a slow-moving mass movement. These velocity-based terms are subjective because the distinction between a 'fast-moving' and a 'slow-moving' flow has not been defined using a precise velocity value. Thus these terms are not practical in process sedimentology (Shanmugam 2006). As a consequence of such ambiguities, the use of the rheology of fluids has come up as an important property to distinguish debris flows and turbidity currents; it can be expressed as a relationship between applied shear stress and the rate of shear strain. Newtonian fluids, like water, will begin to deform the moment shear stress is applied, and the deformation is linear. In contrast, some naturally occurring materials will not deform until their yield stress has been exceeded; and then, deformation is linear. Using rheology as the basis, deep-water sediment flows are divided into two broad groups, namely, Newtonian flows, which represent turbidity currents, and plastic flows which represent debris flow (Shanmugam 2006).

A *Debris flow* is a sediment flow with plastic rheology and a laminar state where shear stress is distributed throughout the mass and from which deposition occurs through freezing en masse. A *turbidity current* is a sediment flow with Newtonian rheology and a turbulent state in which sediment is supported by turbulence and from which deposition occurs through suspension settling (Shanmugam 2006).

1.2.5 Submarine mass-movement mechanics

The basic aspects of submarine mass movement processes are not well understood yet. For years, researchers have still explored the role of pore pressure and fluid gas migration in slope instability. Elevated pore pressures are often essential for mass movement initiation. Sediments may be pre-conditioned for failure by the processes that originally deposited them. Continental margin development might also result in focused fluid flow and elevated pore pressures where sedimentation rates are not extremely high, suggesting that margin architecture also recreates an important role in overpressure and is the most likely place for the occurrence of submarine slope failures (Mosher et al. 2010). A historically common trigger for submarine mass movements is ground accelerations due to earthquakes; nevertheless, the majority of submarine mass movements and the largest recognized submarine mass movements happen along passive continental margins, where seismicity is not that much expected. Horizontal and vertical accelerations during earthquakes increase loads and cause pore pressure responses in specific geologic horizons. The actual trigger mechanism has no importance for some slopes; rather, an environment for failure results from a series of pre-conditioning factors. So the slope may fail under relatively small external loads (Mosher et al. 2010). The second most common trigger mechanism for known historic submarine mass movements has been anthropogenic (Mosher et al. 2010). For instance, heavy rainfall also might be the main trigger mechanism for landsliding at the Nice airport event in 1979 too, but at the same time, two other combination factors can be taken into consideration as well, like the presence of sensitive, weak “quick clays” and an additional load on the upper slope due to coastal construction without consideration for the local geological and geotechnical conditions (Dan et al. 2007). Other submarine mass movement trigger mechanisms have been hypothesized that include elevated pore pressures related to gas accumulation, such as might be provided by dissociation of gas hydrate. Gas hydrate dissociation results in

loss of solid material, production of free gas, and increased fluid pressures, all of which have the effect of decreasing sediment strength (Mosher et al. 2010).

Reducing strength of the sediment	Increasing stress on the sediment
Fluid flow (include seepage)	Sedimentary loading
Sedimentary loading	Erosion (include undercutting)
Weak layers	Earthquakes
Gas discharge	Storm wave loading
Gas Hydrate dissociation	Tectonic movement
	Volcanic island collapses
	Human impact (point loading)

Table 1.1 Factors for the destabilization of sediments characterized by increasing stress or strength reduction (Masson et al. 2006).

These triggering mechanisms (Table 1.1) have been classified by Masson et al. (2006) as factors that increase stress on the sediment and factors that reduce the strength of the sediment.

Some terms have been used to describe processes that could be considered a transitional type between slumps and debris flows. Terms such as flow slide have been used for high-velocity subaerial processes. A debris slide is used when a slow-moving mass breaks up into smaller blocks as it advances, whereas a fast-moving mass that breaks up into smaller blocks as it advances is called a debris avalanche. Catastrophic (fast-moving) debris flows are called sturzstrom, the term creep refers to a slow-moving mass movement. These velocity-based terms are subjective because the distinction between a ‘fast-moving’ and a ‘slow-moving’ flow has not been defined using a precise velocity value. Thus these terms are not practical in process sedimentology (Shanmugam 2006). As a consequence of such ambiguities, the use of the rheology of fluids has come up as an important property to distinguish debris flows and turbidity currents; it can be expressed as a relationship between applied shear stress and the rate of shear strain. Newtonian fluids, like water, will

begin to deform the moment shear stress is applied, and the deformation is linear. In contrast, some naturally occurring materials will not deform until their yield stress has been exceeded; and then, deformation is linear. Using rheology as the basis, deep-water sediment flows are divided into two broad groups, namely, Newtonian flows, which represent turbidity currents, and plastic flows which represent debris flow (Shanmugam 2006).

2. AREA OF WORK

2.1. Tectonic circumstances and Seismicity

The Ligurian Margin is located at the termination of the Southern French Alps between the high elevation crystalline massif of the Argentera and the low topographic Ligurian oceanic basin (Figure 2.1) (Shanmugam 2006). In the western Mediterranean region, the deformations result primarily from (1) the convergence between the Africa and Eurasia plates since 100 My and (2) the opening of the narrow Liguro-Provençal oceanic basin. The convergence between the two plates happens at a rate of 6.2+/-0.5 mm/yr in a 163N+/-9° direction at the longitude of the Western Alps, according to the Nuvel-1A plate movement model (DeMets, Gordon, Argus, & Stein, 1994).

The Southern Alps-Ligurian basin junction is a highly complicated geological region where several major geological units are joining: (A) the crystalline unit of the Argentera massif; (B) the sedimentary units of the southern sub-alpine massifs (or «Nice» and «Castellane» arcs) over thrusting their foreland southward; (C) the Helminthoides flysch (internal alpine nappes); (D) the Penninic alpine nappe; (E) the Tethyan phiolitic nappes; (F) the upper and lower continental margin; (G) a transitional crust and (H) an atypical oceanic crust (Larroque et al. 2010). The sub-alpine nappes were previously the sedimentary cover of the Argentera massif. In the Southern Alps-Ligurian basin junction, the building of relief arose during two main steps since Oligocene time: (1) Extensive phases, affected by a counter-clockwise rotation of the Corsica-Sardinia block, directing to the opening of the Ligurian oceanic basin from 28 to 18 My (Larroque et al. 2001). (2) Compressive phases led to the emplacement of the Argentera massif, of the Castellane and Nice arcs from 15 My (Larroque et al. 2001), and to the development of the Valensole and Var basins.

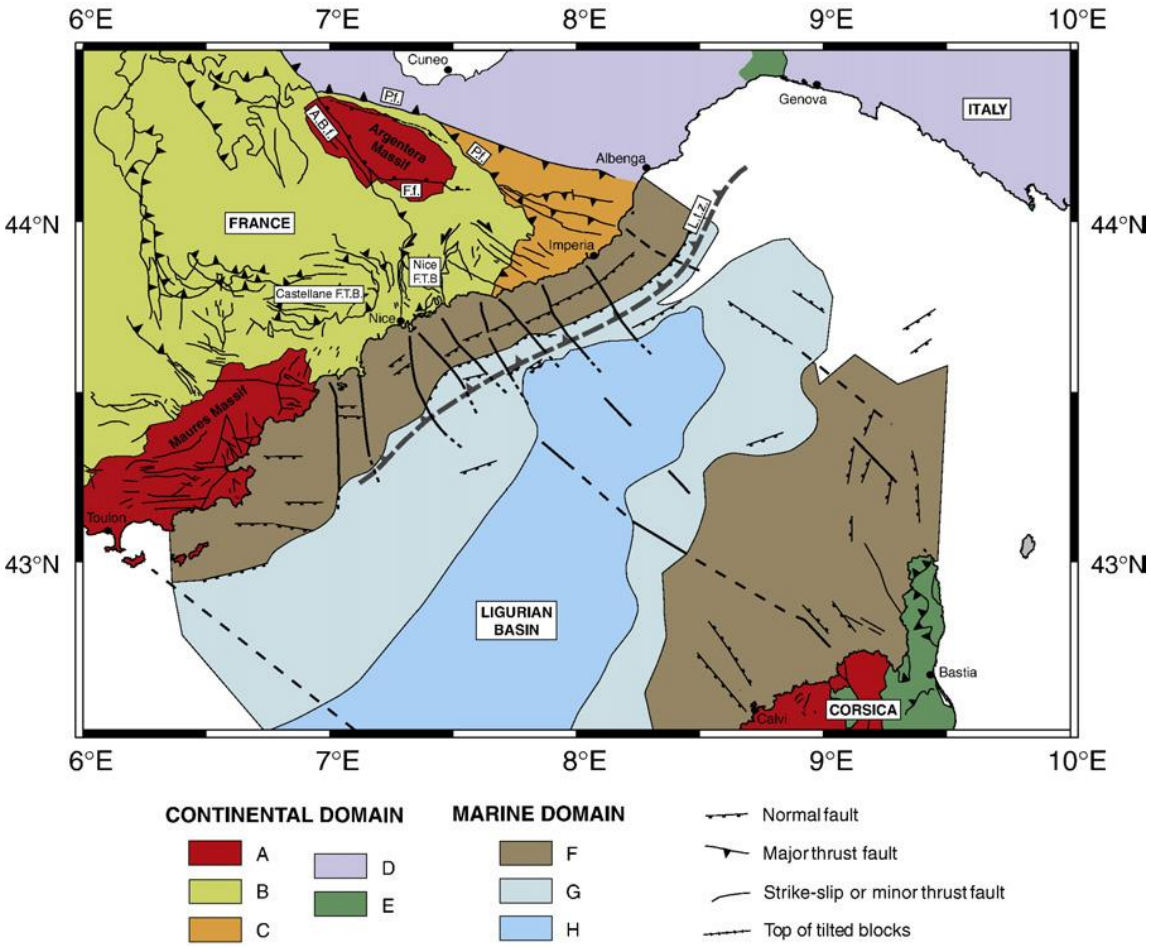

Figure 2.1 Structural sketch of the Southern Alps-Ligurian basin junction. A.B.f. Argentera-Bersezio Fault; F.f.Fremamorte Fault; P.f. Penninic Front; L.t.z. Ligurian thrust zone (Larroque et al. 2001). Red box represent the study area.

The northern Ligurian margin shows typical features of a rifted continental margin, with tilted blocks bound by southeast dipping listric faults (Larroque et al. 2001; Gidon 1992). Several uplift events have been recorded since 23 My. As (Larroque et al. 2010) pointed out, a recent uplift acceleration since 3.5 My is certainly related to the tectonic process (Figure 2.2).

Although Western European countries are presently considered as areas of low- to moderate Seismicity, the kinematic of the present-day deformation within the Africa-Eurasia plate boundary in the Western Mediterranean remains poorly known (Figure 2.3).

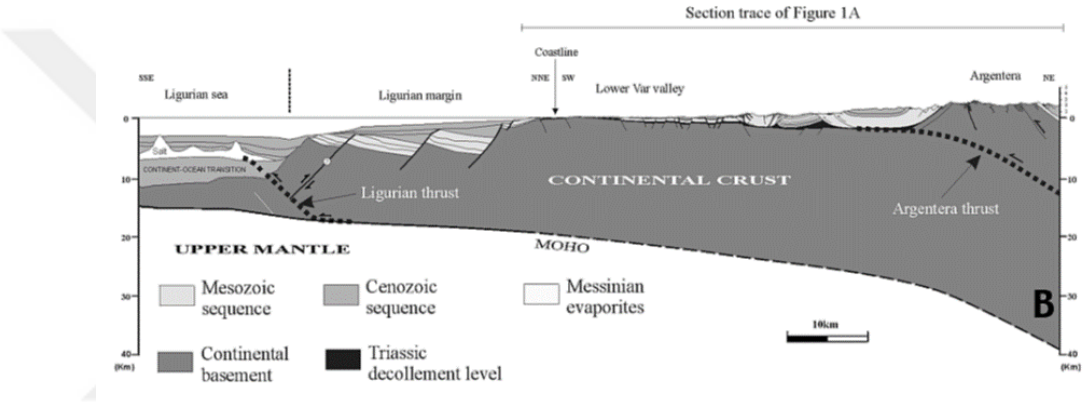

Figure 2.2 Cross-section of the Southern Alps and Ligurian basin (Mallace 2005).

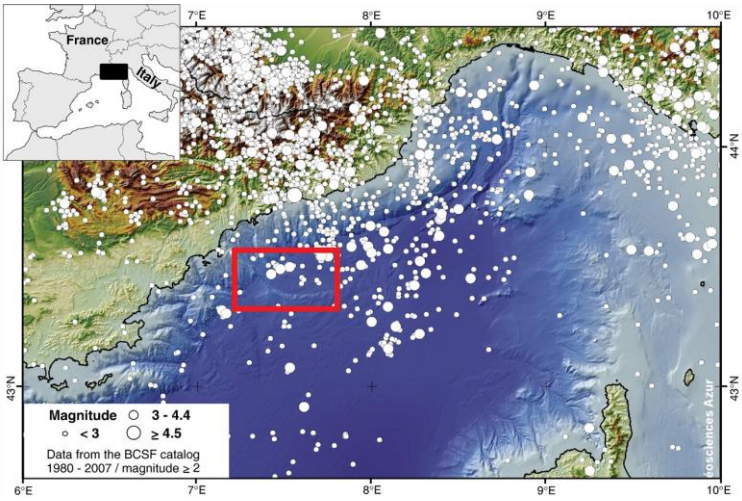

Figure 2.3 Seismicity map of the Alps and Ligurian Basin recorded from 1980 to 2009. Red box represents the study area. (Larroque et al. 2010)

2.2. Geomorphology

The present-day large-scale geomorphology of the Ligurian Margin is dominated by sharp relief: only 80 km separate the coastline from the summits of the Argentera massif (3000 m). Onshore, gorges with current depths up to several hundred meters incise the topography (Klaucke et al. 2000) (Figure 2.4). Offshore, there is no continental shelf. The shelf-slope system is so narrow and steep that most of the sedimentary load bypasses the slope and arrives directly on the bathyal plain of the margin. The depocentre of the sediments is situated at the foot of the Ligurian slope (Lofi et al., 2011), and the width of the shelf ranges from a maximum of 2 km to less than 200 m (Migeon et al., 2011).

The shelf break is therefore located close to the coastline, at 50-100 m of water depth on average but could be much shallower, i.e., less than 20 m of water depth, like in front of the Nice airport (Dan et al. 2007). The continental slope is the steepest in the world according to Harris (2011) an average slope gradient of 8º and a maximum of 20º down to the 2200 m isobath (foot of the margin) at 24 kilometers from the coastline. The slope base is characterized by a sharp decrease of the slope angle to less than 3° (Vietti et al. 2010). This continental slope is cut by large, deep, and closely spaced sub-marine canyons such as the Var and Paillon canyons. These canyons were initiated during the Messinian salinity crisis as a consequence of the lowering of the sea level (Larroque et al., 2010; Lofi et al., 2005). The steep continental slope is affected by numerous scarps that are related to sediment failures and sub-marine landslides (Migeon et al., 2011).

The main sedimentary accumulation of the Ligurian Margin is the Var turbidite system, extending from the coastline offshore Nice to the Corsica island (Migeon et al. 2006; Savoye et al. 1993). Particles are delivered to the Var system through two canyons, the Var and Paillon canyons, directly connected to rivers on land. Sediments are then distributed on the slope via gravity-flow processes (Migeon et al. 2011). The Var and

Paillon canyons coalesce at 1600 m of water depth and merge into a single submarine valley about 170 km long (Migeon et al. 2006).

In its middle part, the Var Valley exhibits an East-West trend, and it is bordered to the south by a thick sediment accumulation, the Var Sedimentary Ridge.

Although the present-day morphology of the margin mainly results from Plio-Pleistocene sedimentary processes, it has also been shaped by the sea-level drop of the Messinian Salinity Crisis (Migeon et al., 2011).

2.3. Site location

The area of interest is located in the northeastern part of the Mediterranean Sea, in the western Ligurian Margin off Southern France (Figure 2.4). The data for this study was acquired during the Cruise M73/1 “LIMA-LAMO” with R/V METEOR in the year 2007.

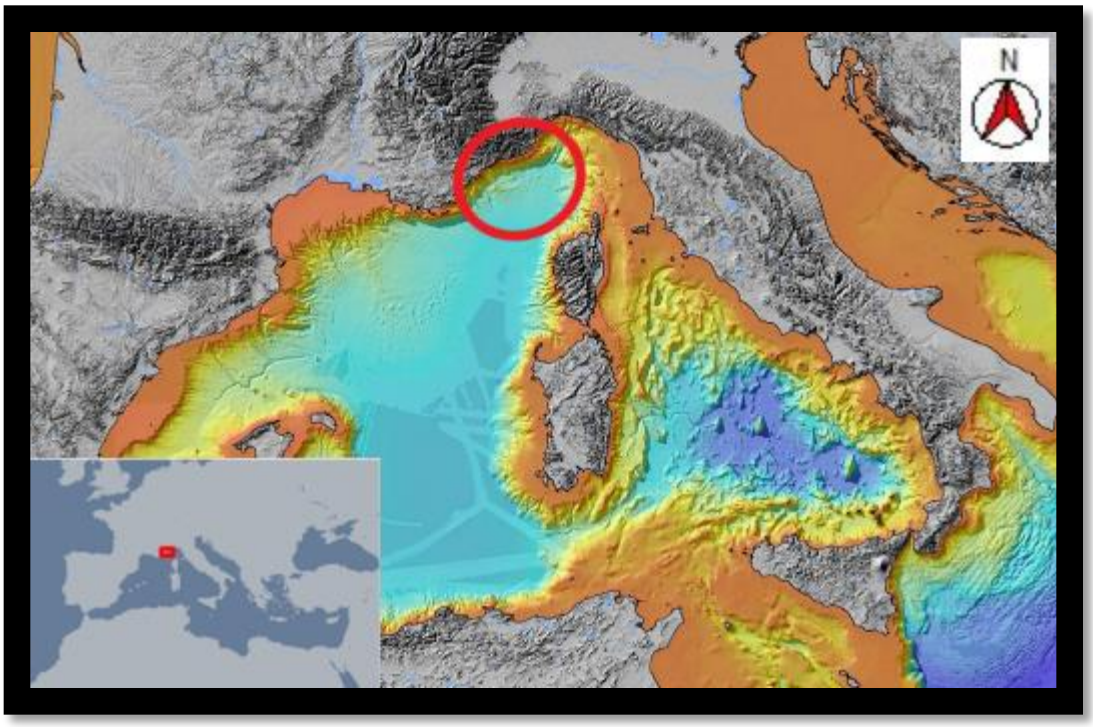

Figure 2.4 Bathymetric map illustrating the morphology of the northern Ligurian Margin, Red area represents the study area (modified from CIESM 2011a).

The present study is centered in two areas (Figure 2.5): 1)The deeper slope, 1500-2000 m water depth, west of the Var Canyon with several landslide scars; 2) The Var Canyon region with its terraces, flanks, and channels in down to the about 2500 m water depth.

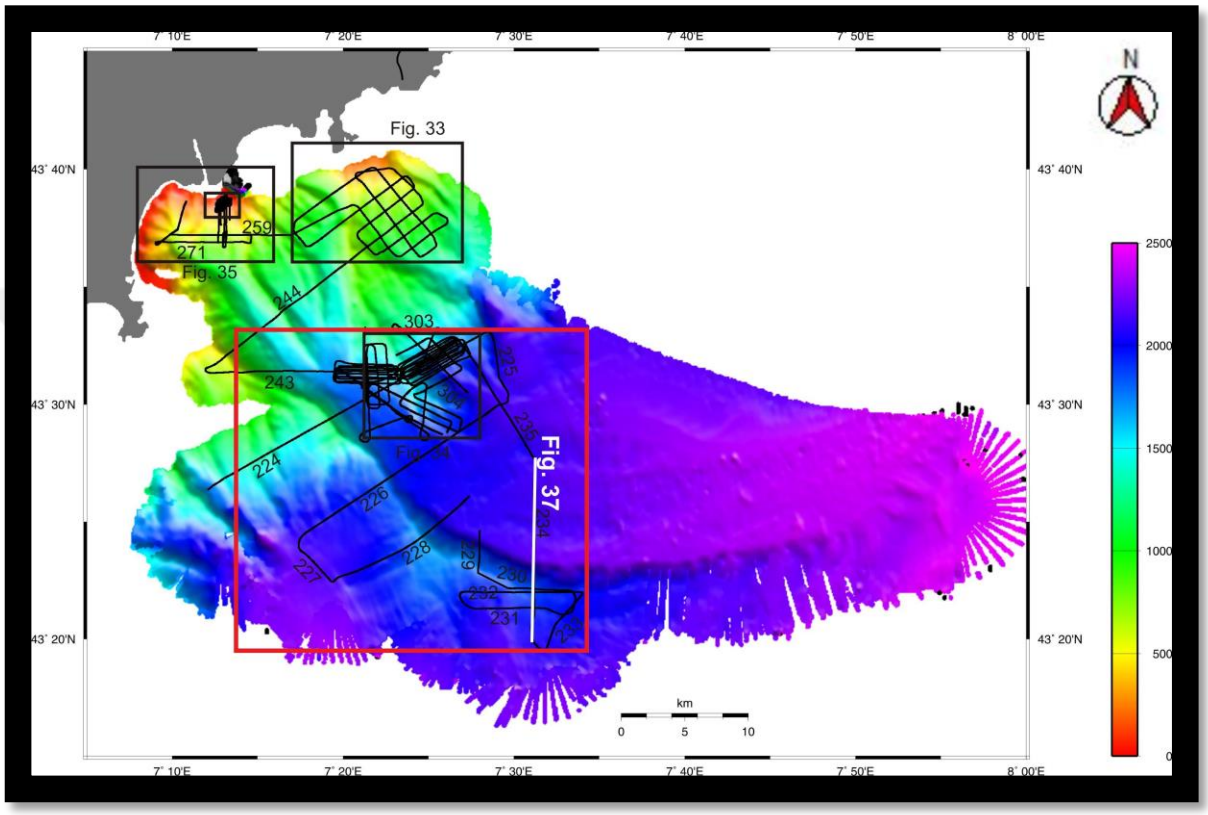

Figure 2.5 Track lines of the cruise M73/1 which acquired the seismic data for the present study. Red box represent the studied areas.

2.4. Scientific Questions

In the context above expressed, this master thesis aims to solve the following scientific questions:

- While the upper slope and shelf survey data sets have been processed and interpreted in various theses and publications, the deepwater survey has not been touched except for one seismic line used in the paper of Förster et al. (2010). Processing the deepwater survey data, doing seismic description properly, talking about distribution of facies type in the region, and trying to find out if there is a certain pattern.
- A better understanding of the internal structure of slide masses and the reconstruction of their development. Retrogressive failure may initiate slope instability from the deepest part, while normal slope failure may be caused by sediment loading and overstepping or by the presence of weak layers, e.g., volcanic ashes. So, which processes control the sliding?
- Since side echoes, chaotic facies, and threedimensional structures affect the overall imaging quality, the data set was therefore designed as a relatively dense grid of cross lines with very few lines along the axis of the slump (because of side echoes). As the third objective, it should be evaluated how well the imaging of such complex structures works in this steep margin setting.
- In the vicinity of the Var Canyon, a sedimentary fan has developed. A set of seismic lines images this transition zone between channeling to widening, the development of levees, and the interaction of the downslope flow with potential bottom currents. Can this interaction be imaged and characterized?

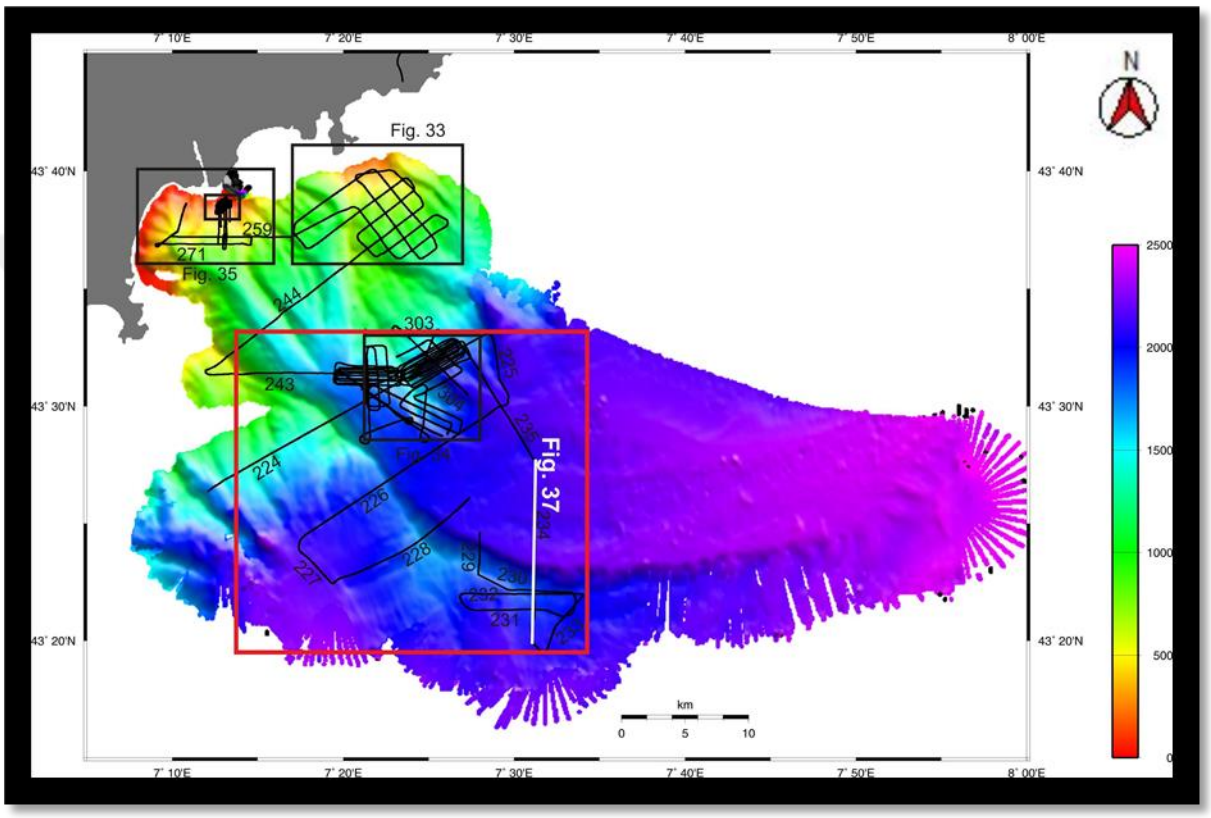

Figure 2.5 Track lines of the cruise M73/1 which acquired the seismic data for the present study. Red box represent the studied areas.

3. DATA

Figure 3 illustrates the concept of marine multichannel seismic measurements. The process uses seismic reflections caused by geological interfaces to make inferences about the subsurface. The impedance contrast at the interface directly determines the strength of reflection. This contrast is a function of the two material properties, density, and acoustic velocity. The higher the difference at a given interface, the stronger the reflection at the interface.

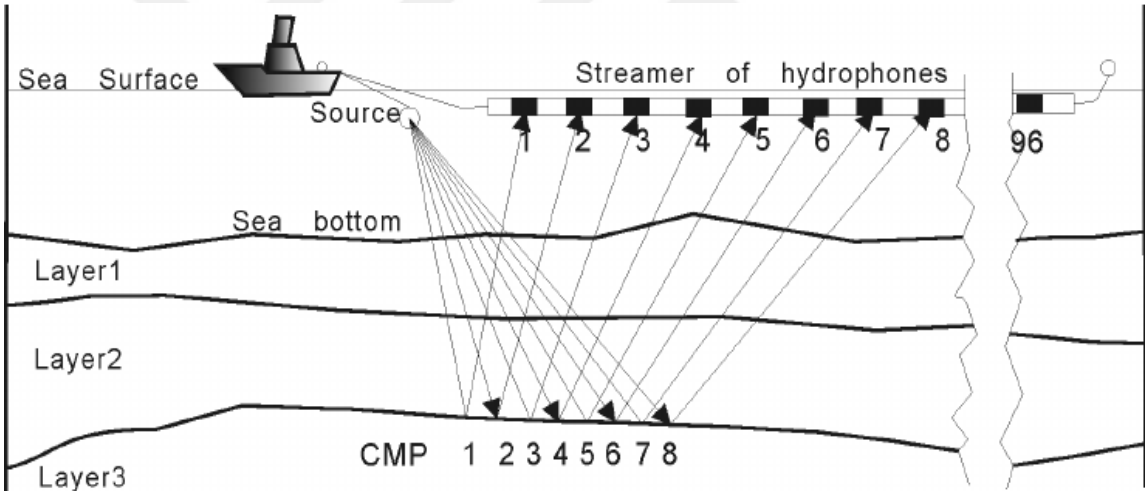

Figure 3.1 Schematic illustration of the marine multichannel reflection seismic acquisition method

Firstly, during the survey, an acoustic signal is emitted into the water column using a specific source. The emitted signal shows a three-dimensional model and direction of propagation. It travels through the water column at about a constant 1500 m/s and finally reaches the seafloor. There, the signal meets the first geological interface. The high impedance contrast leads to the reflection of a fraction of the signal. The reflected acoustic signal travels back to the surface and is acquired by hydrophones (Figure 3.1). Within the

hydrophones, the acoustic signal is converted into an electric signal and sent to the ship. This electric signal incorporates information about when the signal took to the interface and back to the water surface. It is digitized using special software. The specific travel time and amplitude of the recorded reflection measure the depth position and characteristic parameters of the recorded geological interface (Yilmaz, 1987). The part of the signal that is not reflected by the first interface travels deeper into the subsurface. At the second geological interface possessing an impedance contrast, the signal is partially reflected and travels to the surface to be recorded (BGR, 2016).

The dataset received through this procedure contains a wealth of information. Each time the gun is triggered is called a shot. Shots are numbered and stored in the software, and the data is recorded for the returning signal. The full dataset consists of a series of shots, and for each shot, the received signal amplitudes and times are recorded for all hydrophones in the streamer separately.

Consequently, for an 80-channel streamer, a one-shot consists of 80 traces. The duration of the trace stored for each channel is defined by the recording length set within the software because storage space is limited.

The dataset itself may consist of thousands of shots, depending on the shot rate and the length of the surveyed line. Shot time and date are recorded to allow further processing. Processing, which includes the rearrangement, enhancement of signal quality, and various data corrections, is vital to enable geological interpretation of the acquired seismic dataset.

3.1. Seismic Reflection Profiling Data

In this study, one multichannel seismic data set and one multibeam bathmetry data was used. The data collected during the expedition R/V Meteor Cruise M73/1: LIMA-LAMO (Ligurian Margin Landslide Measurements & Observatory), from 22.07.2007 to 11.08.2007 (Table 1.3).

Table 3.1 Details about seismic and multibeam data sets.

Area	Data type	Description
Var Canyon area	Seismic lines	2*1.7 L GI gun, 30ms Delay. 500m streamer 80 channel.
Eastern and Western Landslide area	Seismic lines	2*0.1 Micro GI gun, 25ms Delay. 500m streamer 80 channel.
Whole area, water depth between 15m and >2000m	Bathymetry	EM710 Kongsberg echosounder, operating frequency: 70 to 100 kHz. EM120 Kongsberg echosounder, operating frequency: 12 kHz.

The upper slope and shelf survey data sets have been processed and interpreted in various theses and publications but the deep water survey has not been touched. So, 17 multichannel seismic lines were processed and interpreted in this thesis study. The total length of seismic lines is 169km which covers the 400km^2 area (Figure 3.2).

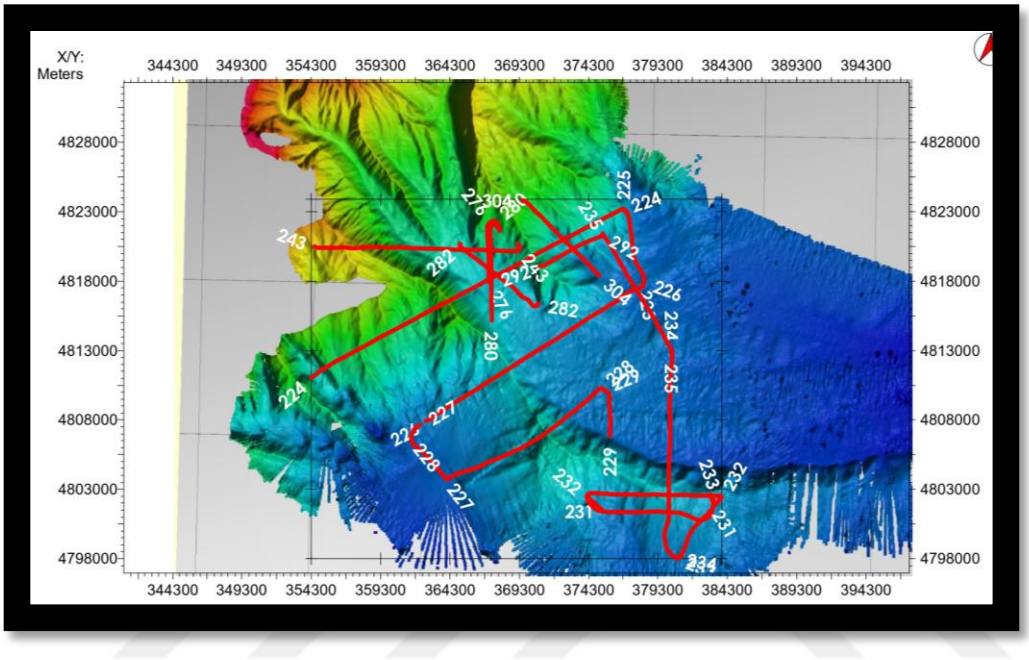

Figure 3.2 Location of the 17 processed seismic line for this thesis.

3.2. Seismic Data Acquisition

By the help of MaMuCS-System (Marine Multi Channel Seismic Acquisition System) which was established at Bremen University all data were recorded. This system allows digitizing up to 96 channels, demultiplexing and storage in SEG-Y format on the internal hard disk drive. Data were recorded at a sampling frequency of 8 kHz. Brute stacks are prepared from the system and displayed on monitor. Recoding length was between 0.8s and 4.5s depending on shooting rate, source and water depth. The delay was adjusted to the water depth. The MaMuCS-PC was also used for logging the ship's GPS data and also for distribution the GPS data to other PCs via the network.

3.3. Seismic Sources

As a seismic source a Mini-GI Gun (2*0.25l), a Micro-GI-Gun (2*0.1l) and GI-Gun with normal chamber volume (2 x 1.7 L) were used in this expedition. But the processed seismic lines in this thesis were shoted only by a Micro-GI-Gun (2*0.1l) and GI-Gun with normal chamber volume (2 x 1.7 L)(Table 3.2). The Micro-GI-Gun and Mini were towed from the port side crane roughly 10m behind the ship's stern (Figure 3.3). Most of the time during the seismic surveying the Micro-GI-Gun was used.

The range of frequency at the Micro-GI-Gun shows higher main frequency ~300Hz, also higher frequencies up to ~600Hz. These numbers change in GI-Gun with a range of ~30-400Hz and main frequency ~200Hz.

Table 3.2 Processed profiles with individual streamer and source settings.

Profiles	Streamer	Source
GeoB07_224-GeoB07_235, GeoB07_243	500m Deep Water	2*1.7l GI-Gun, 30ms Delay
GeoB07_276, GeoB07_280, GeoB07_282, GeoB07_292, GeoB07-304	500m Deep Water	2*0.1L Micro-GI, 25ms Delay

At the Mini- and Micro-GI-Gun the gun delay is 25ms for most profiles, which was the perfect value for eliminating bubles. 2*1.7l GI-Gun was towed from the starboard side crane roughly 17 m behind the ship's stern. Guns were connected to a bow hanging on two

chains 40 cm beneath. An elongated buoy, which keeps the guns in a horizontal way in a water depth of ~1.2 m, was connected to the bow with two rope loops.

The Injector was triggered with a delay of 30 ms or 50ms at GI-Gun which helped to eliminate the bubble signal. Guns were shot a 140bar. The shooting interval was specified based on water depth. The maximum shooting interval in deep water was 5s, which resulted 4 knots cruising speed with shot point spacing of approx. 8m. The deck plan is shown in Figure 3.3.

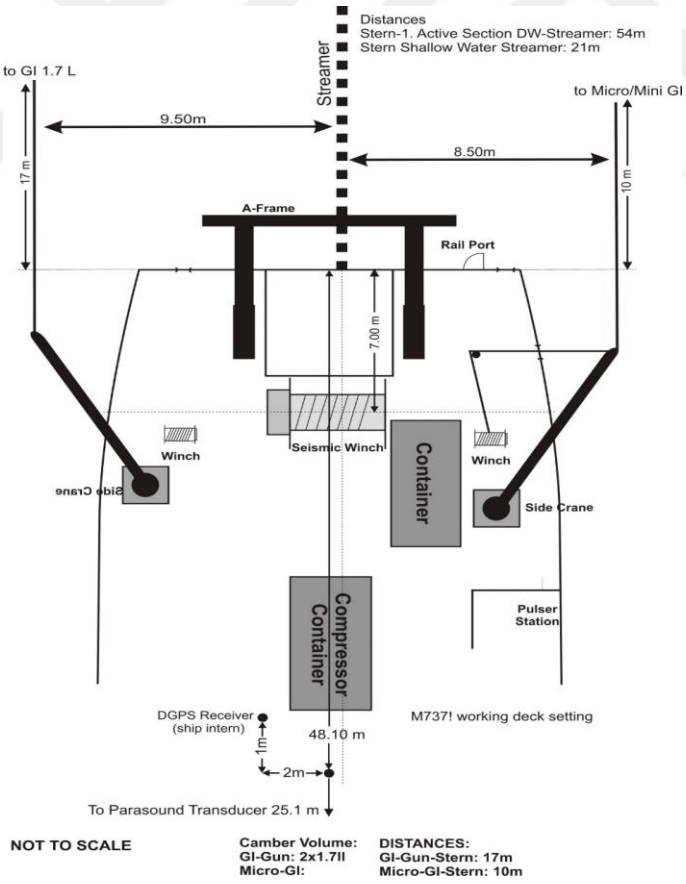

Figure 3.3 Deck plan.

3.4. Streamers

During in the expedition two streamers were used for recording a data: a 500m long 80-channel streamer for deep water depth and a 50m long 48-channel streamer for shallow water depth(less than 400m). In this study processed seismic profiles recorded only by 500m long 80-channel streamer (Figure 3.4).

The 500m long 80-channel streamer or SYNTRON consists of 10 active sections each 50m in length and included a lead-in of 54m. These 50-m-sections are subdivided into 8 hydrophone groups. Each 6.25m extended hydrophone group was divided into 5 subgroups of different lengths. All channels from 1 to 80 connected to the recording system of MaMuCS, independent of the hydrophone group length. Depth control of the streamer was achieved by four DigiBird Remote Units. The defined streamer depth was 3m.

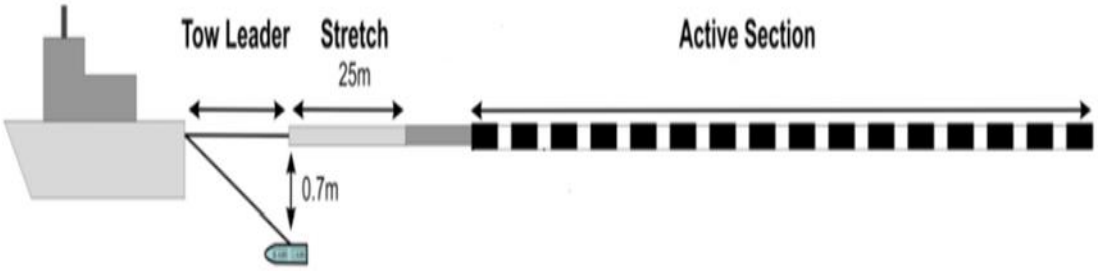

Figure 3.4 Schematoc view of the aigun and streamer equipment.

For shallow water work <400m, a 50m-long 48-channel streamer was used. Each group consists of a single hydrophone; the space between hydrophones is 1m, and the space to the first hydrophone is 1m. Again MaMuCS-System was used to record seismic data. To check the depth in the shallow water streamer, small buoys connected to the streamer by

a 1.5m elongate elastic rope, resulting in a towing depth of the streamers of ~1m. Both streamers were deployed close to the ship's axis.

3.5. Multibeam Swathmapping Data

Two multibeam systems from KONGSBERG MARITIME were installed on the cruise during this expedition. One of them is used for shallow water EM710, and another one for deepwater EM120 system.

The EM710 lodged is a new 1-by-1-degree broadband multibeam echosounder that performs in the 70-kHz to the 100-kHz band. The system utilizes CW (continuous wave) vibrations in shallow modes and FM (chirp) vibrations in deep modes. For the EM710, the most efficient depth scope is less than 500m because, at this depth, it has a good resolution than the EM120, but it can work even at maximum depth up to 1500m to 2000m. The EM120 system was operated for deepwater. To get a better explanation of the systems, please check the Weinrebe et al. (2006).

The EM120 has a grid spacing of 25m, and this number for the EM710 is 10m. The EM120 system recorded ~2000 km2 area from 10m – 2500m below sea level during the whole expedition time. There are many gaps in the data for deep waters, which implies an unstable data acquisition due to vessel speed(Figure 3.5). The data received by the EM710 system also shows some problems(Figure 3.6), the limited range of the system, duration of the multibeam signal, and errors with increasing water depth affected the South part of the track.

Data of both operating systems show the specific canyon structures with ridges of the slope south of Nice in shallower waters up to 800 m depth. The Var canyon is visible from the NW coast to the southeast on both data sets. Only the EM120 system could supply the data of Var Canyon's continuation and expire at the abyssal plain. At the slide areas, a dense grid of seismic profiles was shot.

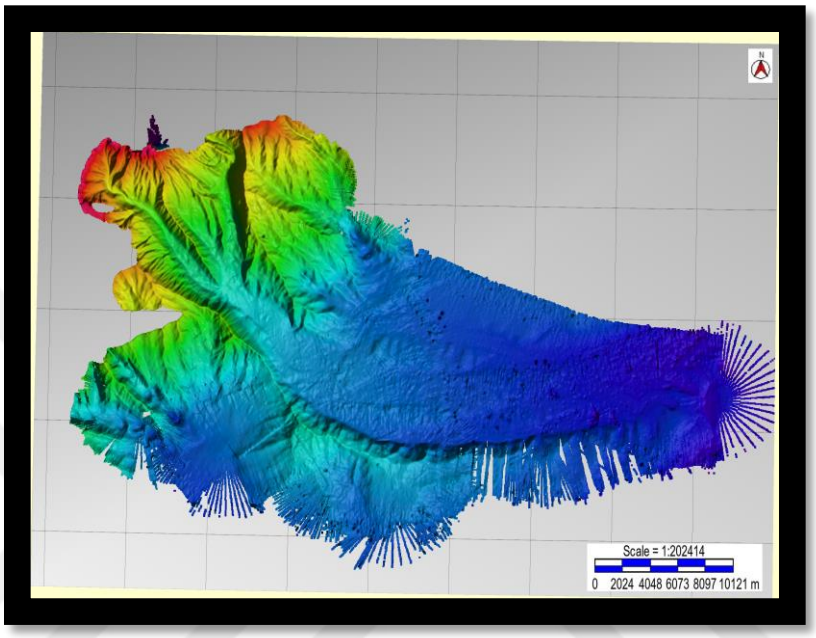

Figure 3.5 The EM120 multibeam system data.

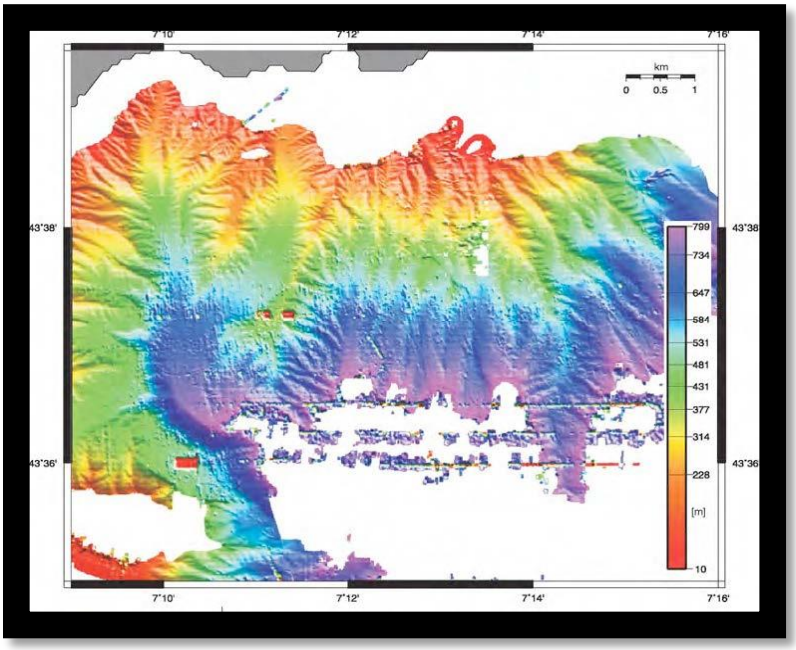

Figure 3.6 The EM710 multibeam system data.

4. METHODS

In the following chapter, the information presented for the different steps containing the processing routine is based on *seismic data processing* by Özdogan Yilmaz (1987) and supported by the help tutorial of VISTA Seismic Processing 2016 owned by the Schlumberger Company.

The goal of seismic data processing is to transform the acquired seismic data into an interpretable geologic area of the earth. Numerous factors change the signal on its path down and back up to the hydrophone. Seismic processing aims to restore as many of these effects as possible and improve the seismic data's signal-to-noise ratio. It is vital to know and understand the regional geology of the working area to apply proper processing steps. There is no single "right" processing routine for seismic data. Judgments have to be made at different stages, which are often subjective and rely on the processer's background(Gadallah&Fisher, 2009).

4.1. Seismic Data Processing Sequence

The crucial tasks here are selecting a proper sequence of processing steps which is suitable for the data, choosing the right options for the per processing step, and assessing the resulting output from each processing step.

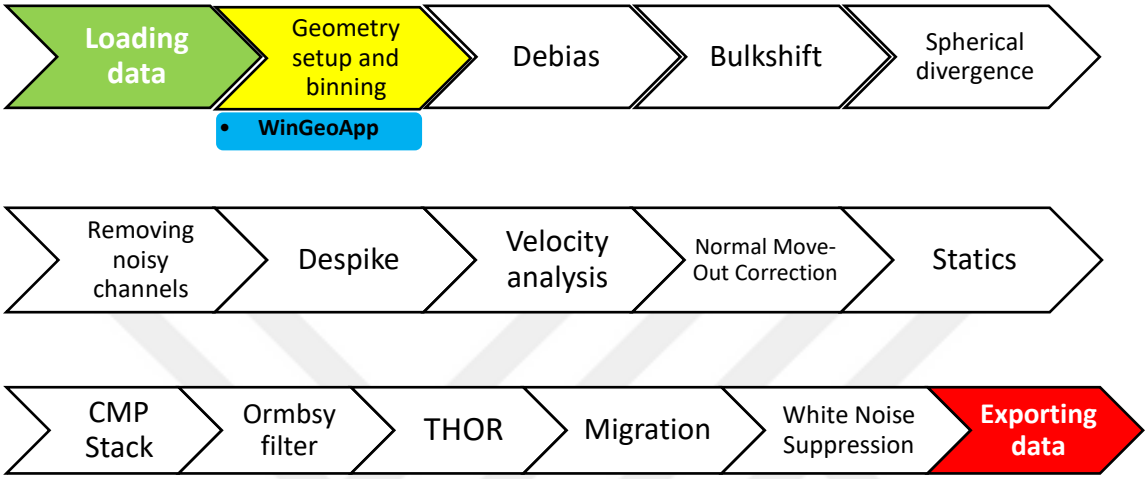

Figure 4.1 Processing steps that were applied seismic dataset in this study.

4.1.1. Loading data

Every SEG-Y dataset represents one seismic profile, which must be loaded into the software. If a recording of one survey line exceeds 4GB maximum file, a combination of multiple files respectively is performed. Behind that, the data format changed from IBM to their actual format, IEE (Figure 4.2).

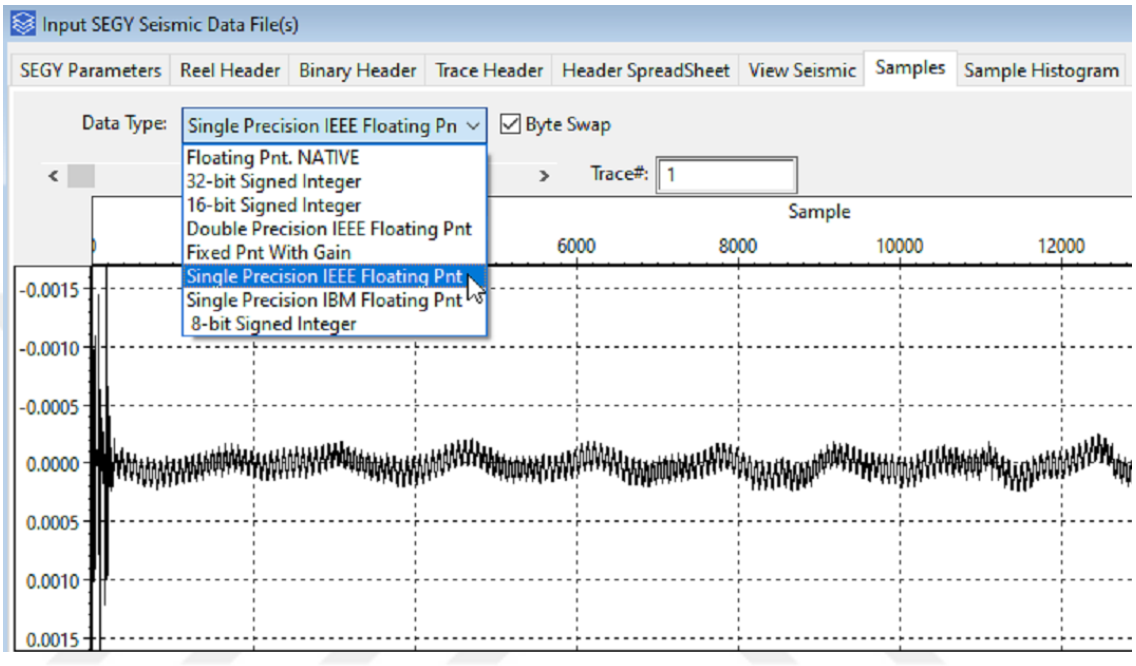

Figure 4.2 Loading one trace seismic raw data into software.

4.1.2. Geometry setup and binning

For geometry setup, the program WinGeoapp (Geometry calculation for marine multichannel seismic), version 2021, written by Dr. Hanno Keil from the Marine Technology and Environmental Research working group at the University of Bremen, was operated. To make calculations, it is vital to know the positions of the hydrophones and the gun to the ship's GPS for every shot using the deck's plan (geometry) and the shot times. These steps have to be followed: firstly, header information was extracted with the help of job flow (Figure 4.3). The header information includes geographical coordinates, time, channel number, and shotpoint number. Then in WinGeoApp, header information, acquisition system geometry, and navigation data recorded in NMEA format using the GPS antenna, were combined. Geometry setting is necessary for the whole process.

The geometry settings contain the exact positions of the source and receiver relative to the vessel's GPS antenna. Then the coordinate system was projected (UTM coordinate zone 32, northern hemisphere), and a new generated ASCII table file was imported into the seismic data headers in Vista with a new job flow.

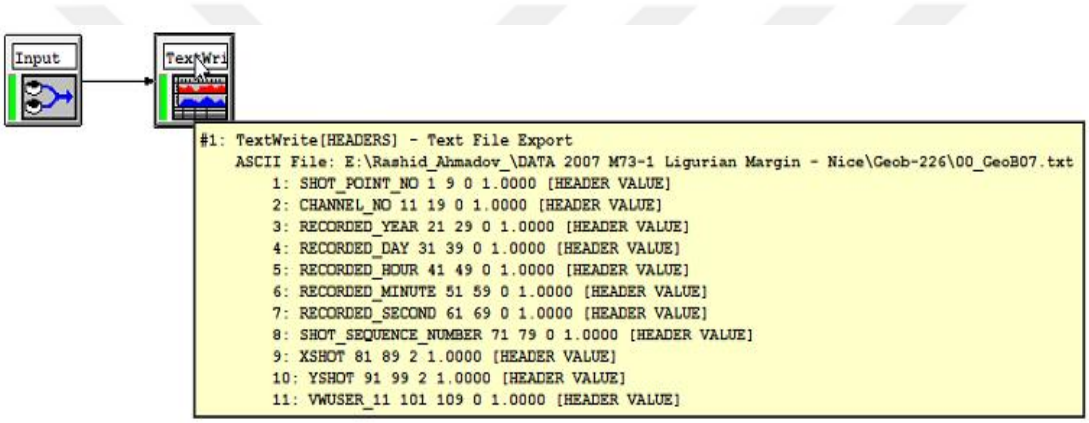

Figure 4.3 Job flow of extracted Header Informations from Vista.

Each shotpoint number must be uniquely assigned to the entire dataset during the binning process. To allow data stacking afterward, binning was done in Vista using an interactive geometry window display. It helps to visualize the geographical positions of all shots, receivers, and midpoints. The bins were positioned on the automatically calculated "surface line," then the size of the bins was set in in-line direction and cross-line direction with the function of bin grid layout (Figure 4.4). The bin size was 4m in my case. The function that "calculate fold/offset" was used to get the resulting fold of coverage. After calculations, the function Display Fold was used to visualize the fold (Figure 4.5).

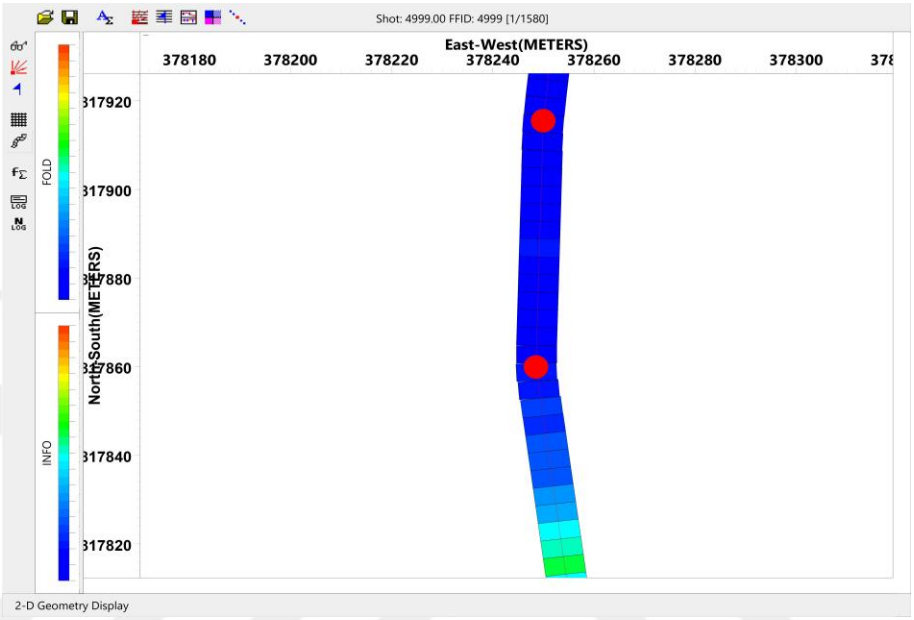

Figure 4.4 Example of a 2D Geometry Window with the illustration of the bins and the surface line.

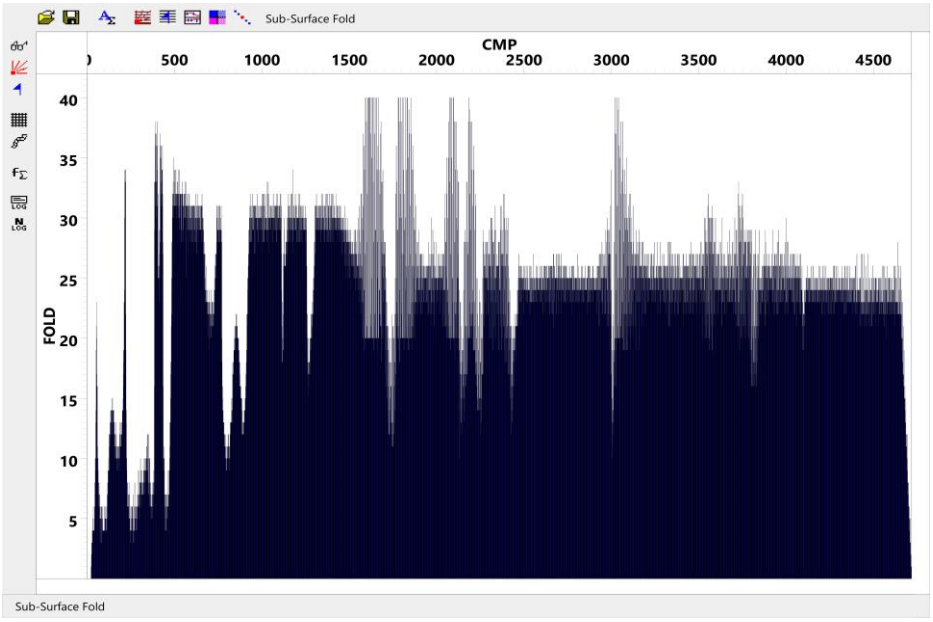

Figure 4.5 Example of the typical fold variation.

4.1.3. Debias

A debias procedure was applied to all traces to shift the trace's bias to zero (Figure 18). The signal received on individual hydrophones revolves around zero, and DC offsets are eliminated from all affected traces. The debiased trace is comparable to other traces in terms of the negative and positive amplitude of the signal. Therefore, stacking the "empty noise amplitude" will not temper the overall uniform signal. Without application, the empty noise would very lower the signal-to-noise ratio of the data at hand (Figure 4.6).

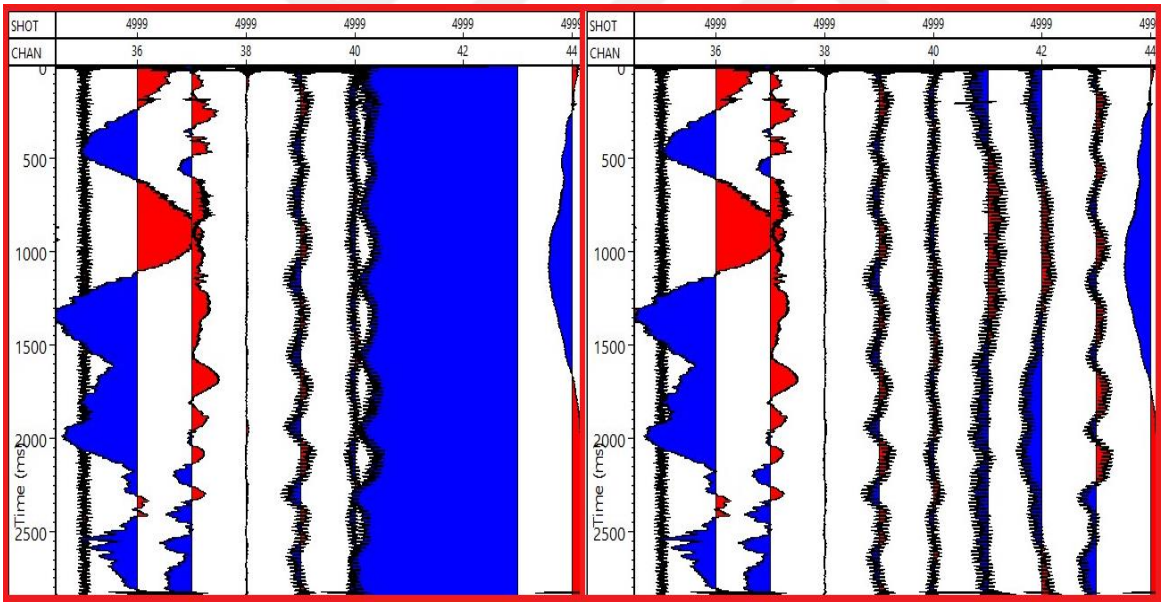

Figure 4.6 The effect of debias, before(left) and after(right) on traces.

4.1.4. Bulkshift

During a marine seismic acquisition, the timing of shot and data recording is calculated accurately and should be the same to get a correct image of the seafloor.

But, the actual release of energy is delayed by a few milliseconds due to the transmission of the gun trigger signal and gun mechanics. Therefore, the data recording starts a few milliseconds before the actual shot, resulting in great depths for the reflections. To delete this time discrepancy, the Gun delay (accounts for the delay between the electrical and mechanical triggering of the GI gun) function was applied to the data. It is determined graphically by analyzing the intersection of the direct wave with the time axis at zero offsets and could be corrected by using the Bulkshift job flow in VISTA (Figure 4.7).

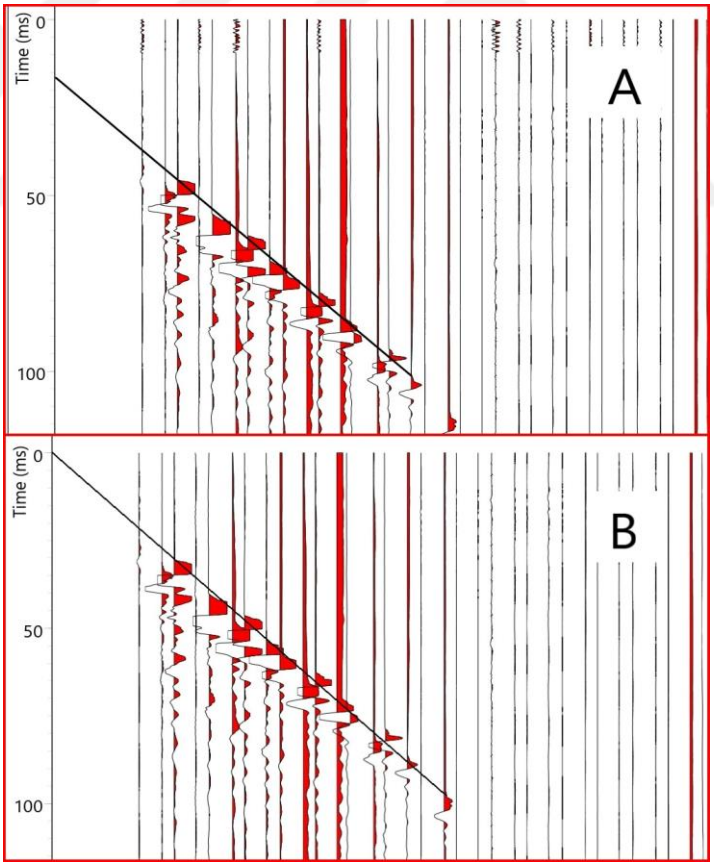

Figure 4.7 Before (A) and after (B) application of Bulkshift module. After the gun delay correction, the direct wave intersects the time axis at 0 seconds.

4.1.5. Spherical divergence

Energy losses due to intrinsic attenuation in rocks affect the wave amplitude and reflection coefficient (Claerboiit, 1985; Brown, 1999; Onajite, 2014). Since seismic amplitude data supply information about the relative impedance changes across reflector boundaries and other material parameters of the earth's subsurface, it is necessary to preserve them by correcting the energy losses (Wang & McCowan, 1989). To solve the problem, a Spherical Divergence Correction is used to balance the data in the time domain.

The Spherical divergence is described as the noticeable loss of energy from a source wavelet spreading through the subsurface. While the wave propagates, the same energy is spread out over a larger surface, decreasing energy density. The Spherical divergence modification was applied using a new Job Flow to restore these energy losses with depth. As input data, the gun delay corrected seismic dataset was applied. Consequently, the deeper parts of the seismic section displayed an increase in amplitude (Figure 4.8).

4.1.6. Removing dead channels

Different factors can impact the recording quality of each channel and the entire streamer. Channels showing transient noise peaks or frequent mono signals are deleted from the dataset, and channels showing no signal. Thereby the overall signal strength compared to the noise strength will be improved.

Firstly, the seismic data was analyzed in the Shot sort order to define and eliminate these inaccurate channels. During analysis, 39 channels (1, 4, 17, 18, 20, 21, 22, 23, 24, 25, 26, 28, 29, 31, 34, 38, 39, 40, 46, 48, 50, 58, 60, 61, 62, 63, 66, 68, 69, 70, 71, 73,74, 75, 76, 77, 78, 79, 80) were eliminated from line M73-1-GeoB07-226. These channels contained no signal at all and much noise. After determining the noisy channels, a new Job Flow operated to delete them.

In the end, 41 channels were left, and on these channels, the next processing flow was applied. Figure 4.9 shows two separate datasets which contain the seismic dataset with and without dead channels. Figure 4.10 illustrates stacked section of seismic line M73-1-GeoB07-226 before and after removing dead channels.

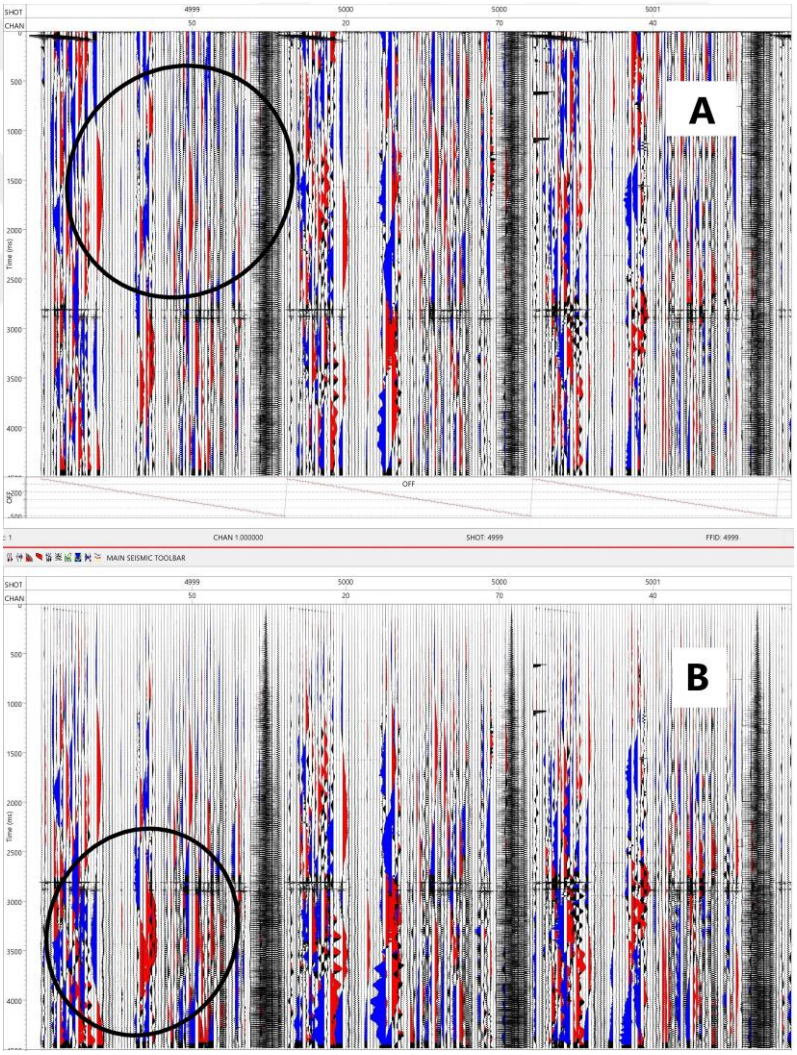

Figure 4.8 The effect of Spherical divergence modification, before(A) and after(B)

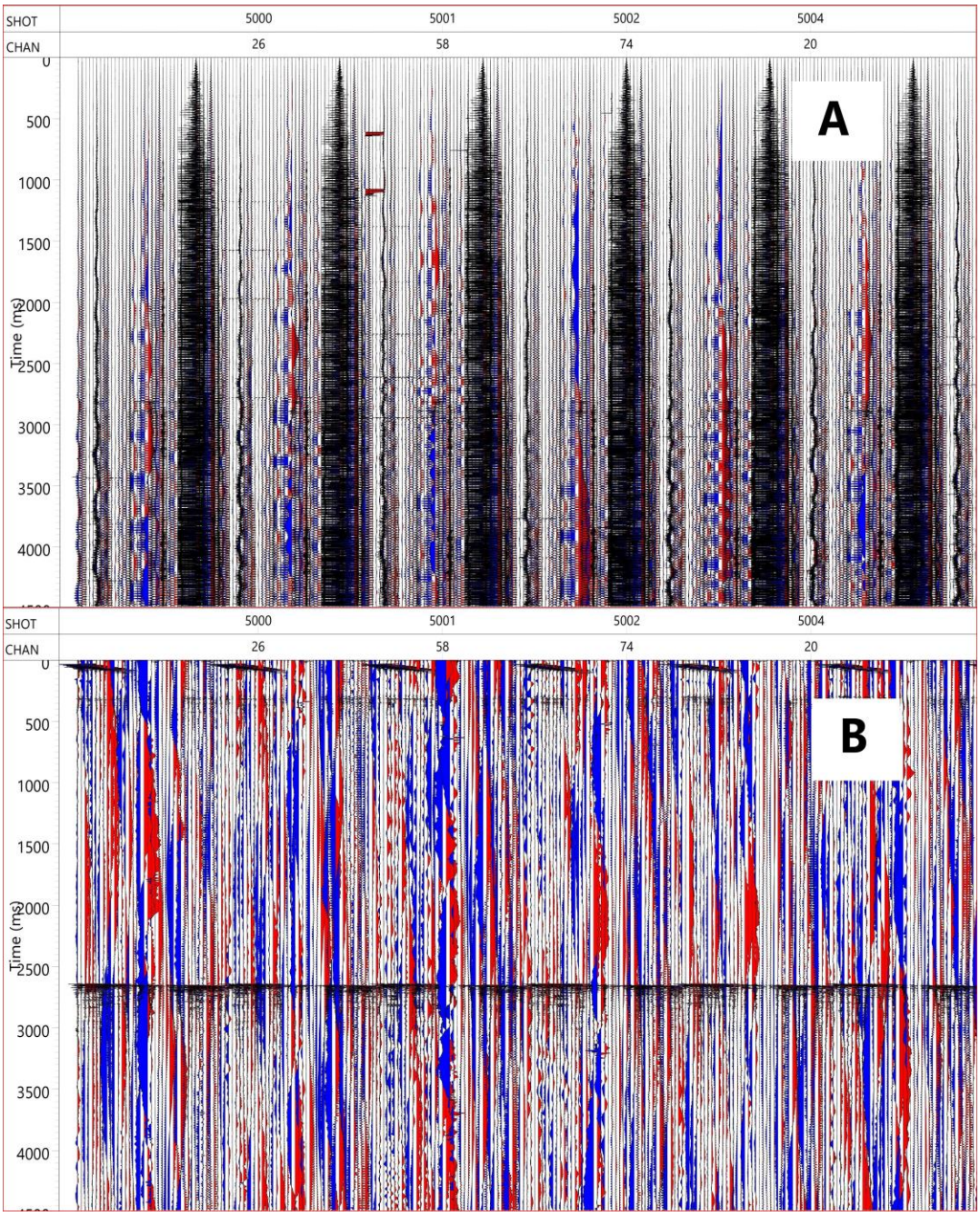

Figure 4.9 Unstacked view of line M73-1-GeoB07-226. Only dead channels (A) and good channels (B).

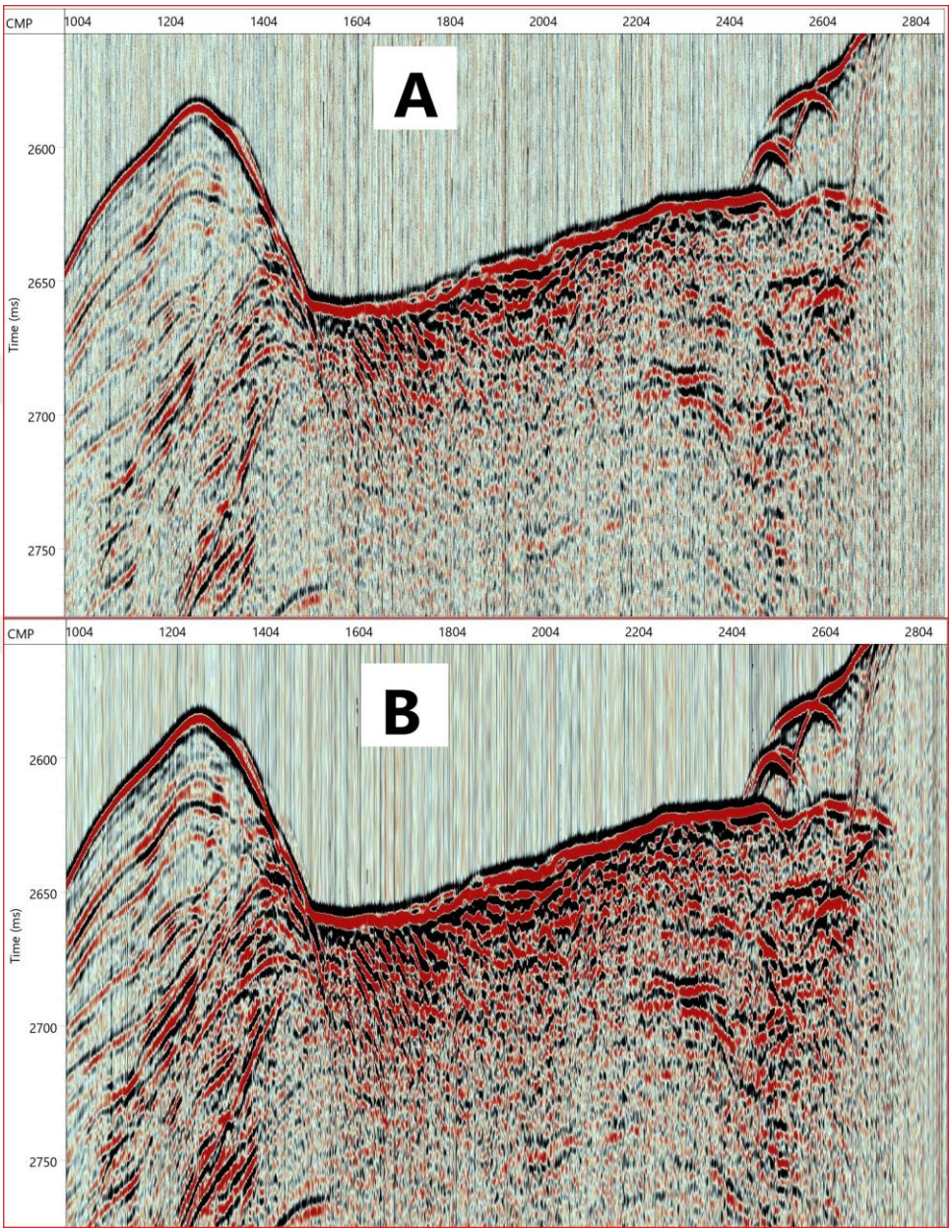

Figure 4.10 Stacked seismic section of profile M73-1-GeoB07-226, A) with dead channels and B) without dead channels.

4.1.7. Despike

Marine seismic data are always infected with noise, which results in unwanted features in the data. This noise can be high-amplitude bursts or spikes spread randomly in the seismic data. High-amplitude spikes in the data can generate "smiles," which appear as multiple small-amplitude bursts unsystematically scattered throughout the section. The suppression of high amplitudes can be done using a Despiking function in VISTA. The function calculates the mean background amplitude in a specified time window and compares the outcome with the actual trace amplitude. If the amplitude of the trace exceeds the calculated background amplitude by a user-defined threshold value, the trace is scaled down. The 2D Despike function was applied to the latest 2D seismic dataset. Parameters of the module are outlined in Table 4.1

Table 4.1 Parameters of the 2D Despike function

User settings	Parameters
250 ms	Time window
15%	Window overlap
7	#Traces in Gate
Mean Amplitude	Operation
1.5	Spike Threshold

Figure 4.11 shows before and after the application of the Despiking module. The suppression of the high-amplitude spikes and the noise can be observed while the valid seismic signal is maintained. 2D Despike module helps to significantly suppress much of the high-amplitude bursts and improve the data quality.

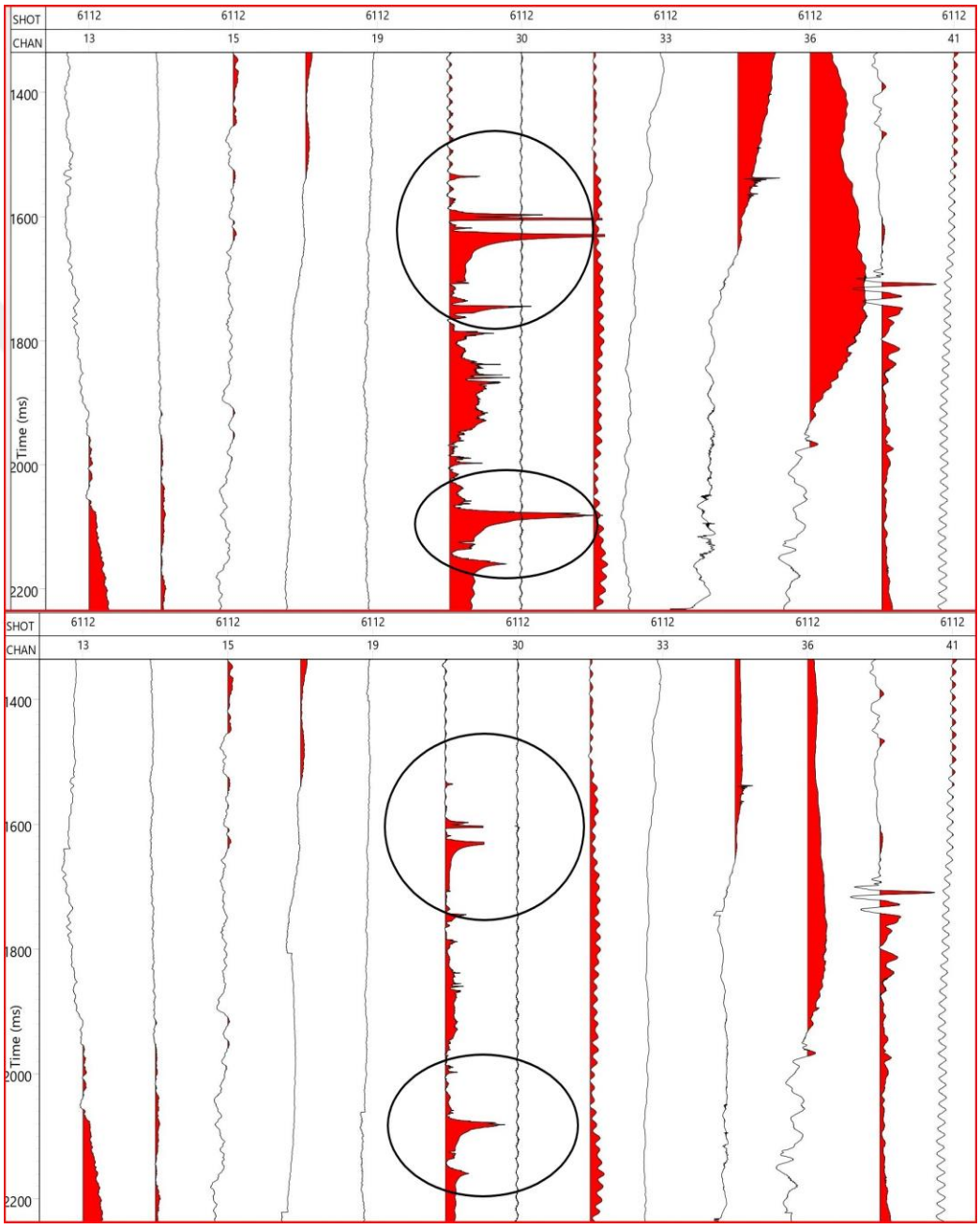

Figure 4.11 Result of 2D Despike module, before (up) and after (down)

4.1.8. Velocity analysis

One of the fundamental steps of processing marine seismic data is velocity analysis. Obtained velocities are generally used for normal moveout correction, stacking, and migration. The velocity analysis was performed using the Interactive Velocity Analysis tool in VISTA.

First of all three output datasets (Constant Velocity Stack, Offset Sort Record/Stack, and Semblance Analysis) were created for the velocity analysis using a new Job Flow (Figure 4.12).

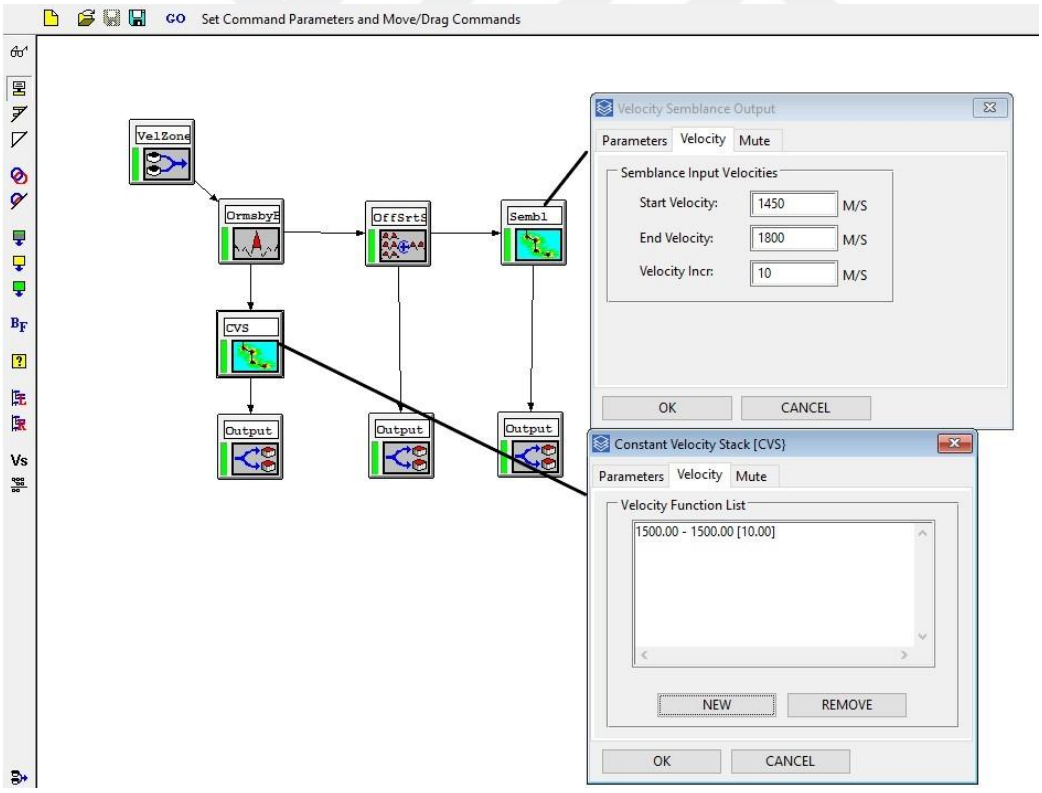

Figure 4.12 Velocity analysis Job flow from VISTA.

As input data, the 2D Despike dataset was used. The Constant Velocity Stack module was operated to stack the seismic data with a constant velocity.

The Offset Sort Record/Stack command worked by sorting CMP ordered traces into offset order and later stacking these sorted traces by offset. The Semblance Analysis module calculates the average energy, which is created using the specified velocity range(1450-1800 m/s Vel. Increment 10 m/s). The semblance analysis window displays high and low average velocities (Figure 4.13 A). Then to get the best velocity fit of individual layers, velocity points are selected by combining all information from three sections of the Interactive Velocity Analysis window (Figure 4.13). Depth and velocity information from adjacent inlines help to decide to choose suitable velocity picks. Figure 4.14 displays the velocity file.

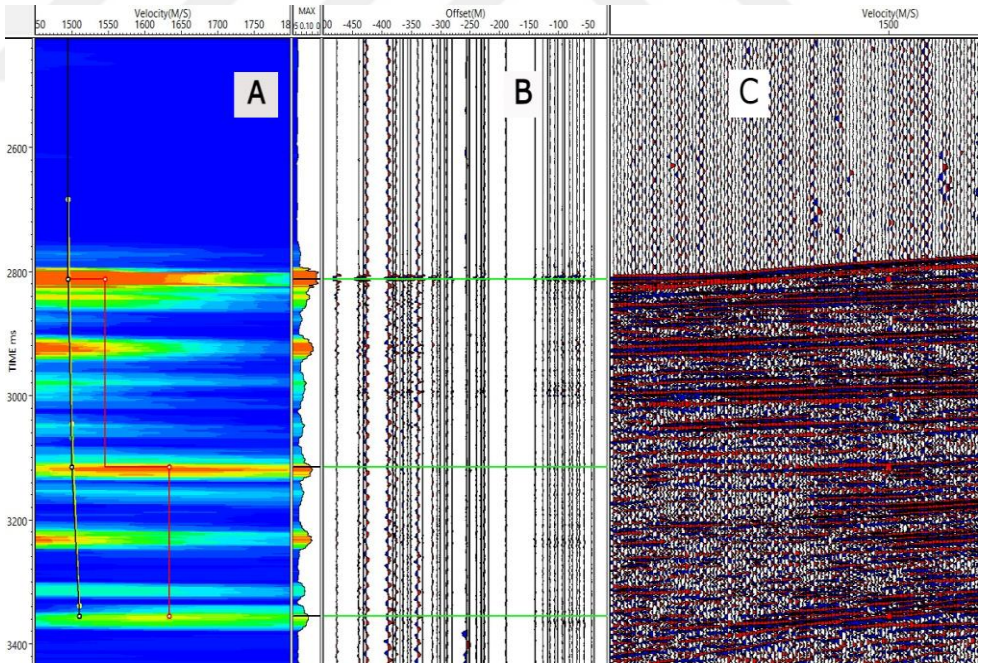

Figure 4.13 Example from Interactive Velocity Analysis window. (A) Semblance window with the energy distribution. Red areas indicate high energy. Black lines indicate picked velocities. (B) Offset gather display showing the sorted traces. (C) Constant velocity stack display demonstrates the result of stacks using various velocities.

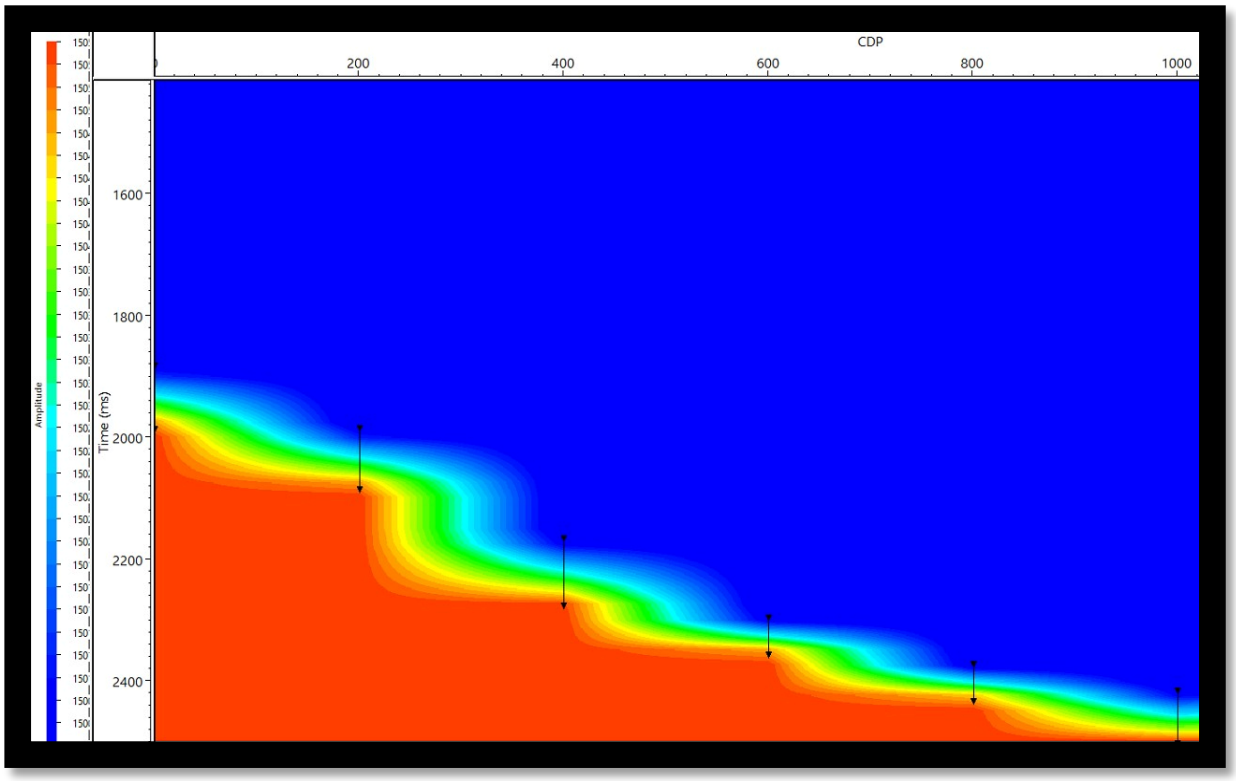

Figure 4.14 Example from Velocity Display window

4.1.9. NMO correction

The time difference between a signal at zero offset (at the distance x = 0) and the same signal at offset x is the normal move-out. The normal move-out correction allows the subsequent stacking of the data. In order to be appropriately stacked, all traces within a CMP have to be zero offset traces. However, offset between the source and other receivers yields a delay in the arrival time of a reflection from a horizontal surface at depth. A plot of arrival times versus offset delivers a hyperbolic shape (Figure 4.15A). The NMO correction removes the normal move-out of each reflection hyperbola on every CMP gather, using the velocity analysis file.

Therefore, the NMO correction can be assumed a standard of the quality of the velocity model. The reflection hyperbola becomes flattened, lower or higher velocities result in the over-and-under correction of the data, respectively.

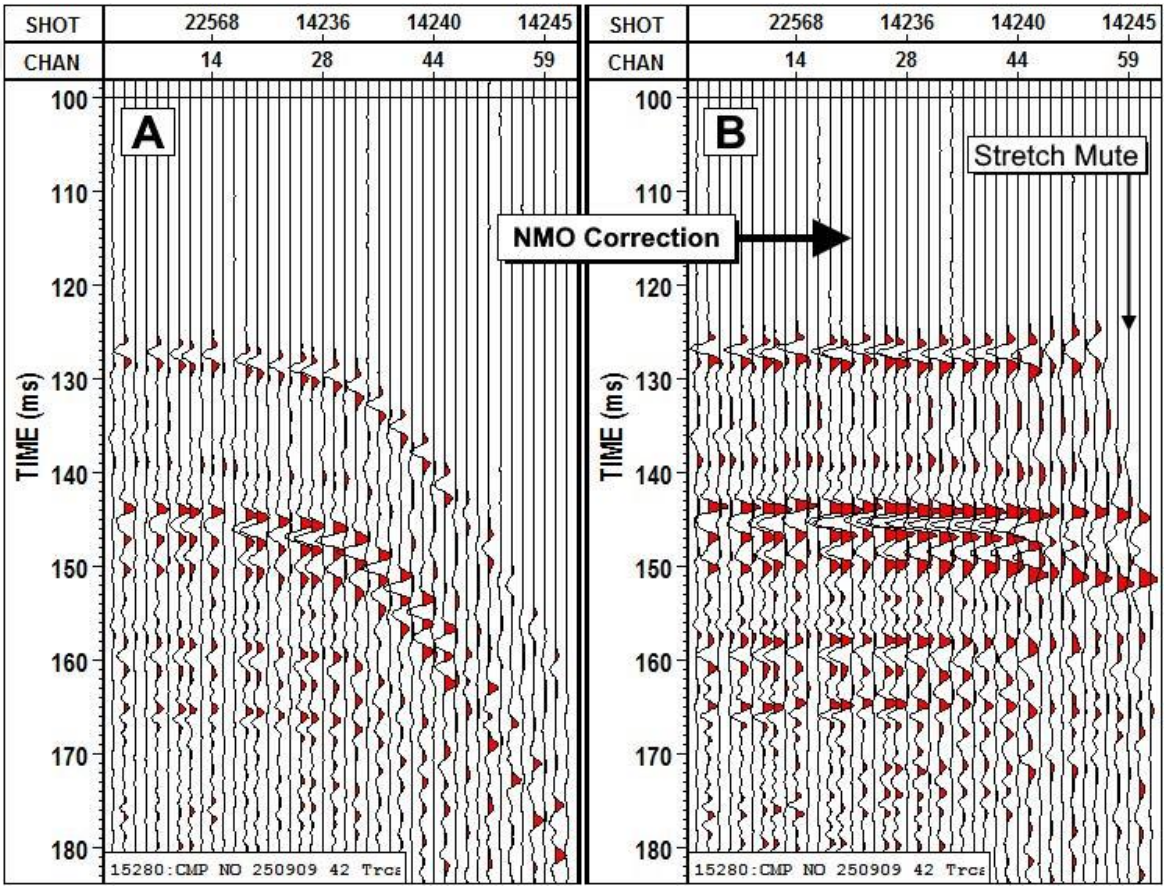

Figure 4.15 The effect of NMO correction before A) and after B).

The stretch mute function was not applied neither before nor after NMO correction. The NMO correction for the 2D seismic dataset was performed using a new Job Flow in

VISTA. All parameters of the NMO module are displayed in Table 4.2. The NMO correction was applied to the latest version of the 2D seismic dataset.

Table 4.2 NMO function's parameters.

User settings	Parameters
Picked velocity model	NMO velocity file
100%	Percent of RMS to use
on	Mute velocity inversions
off	Apply NMO strecth mute
on	Scan from top for strecth mute

4.1.10. Static correlation

During the acquisition of marine seismic data, vertical depth variations of the streamer caused by wave movement, tides, or an incorrect depth control can result in delayed signal travel times. These time delays can produce vertical shifts between traces within an NMO corrected CMP. A vertical shift between traces results in harmful interference during the stacking process, reducing the quality of the stack. In stacked data, the vertical time shifts are often noticeable by a seafloor because the traces are not summed up perfectly.

Statics Correction was applied to the seismic data to balance travel time differences using a new Job Flow(Figure 4.16) and the module is Model Correlation. The method is based on assessing the stacked section as a function of a static model. The Statics correction module was operated in two different steps.

The first step is to calculate the static shift using the module Model Correlation. The number of iterations and the maximum vertical shift are essential parameters to specify. Then the output file of this step is saved in an *SRS* file format.

The next step was applying the previously created statics model to the seismic data. This is realized using the module Read Static Shift in a New Job Flow. All setting parameters are summarized in Tables 4.3.

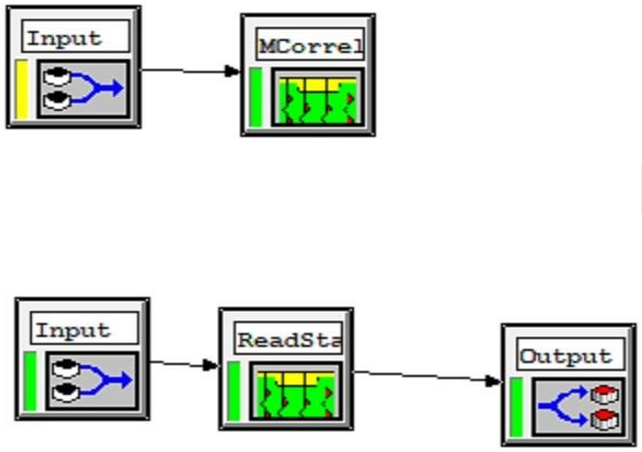

Figure 4.16 Job flows of Static Correlation processing step

Table 4.3 Summarized parameters of the Module Correlation module

User Settings	**Parameters**
NMO corrected unstacked data	Data Input
20 ms	Correlation Window
7 ms	Pick Window
On	Band-Pass Correlation
5	# of iterations
CVC stack	Input model
Gauss-Siedel	Solution method

Figure 4.17 shows a CMP stacked version profile before and after applying the static correction. It can be observed that the statics correction caused a important effect especially in the seafloor reflection. The statics correction was carried out several times with different parameters regarding the number of iterations and maximum vertical shift.

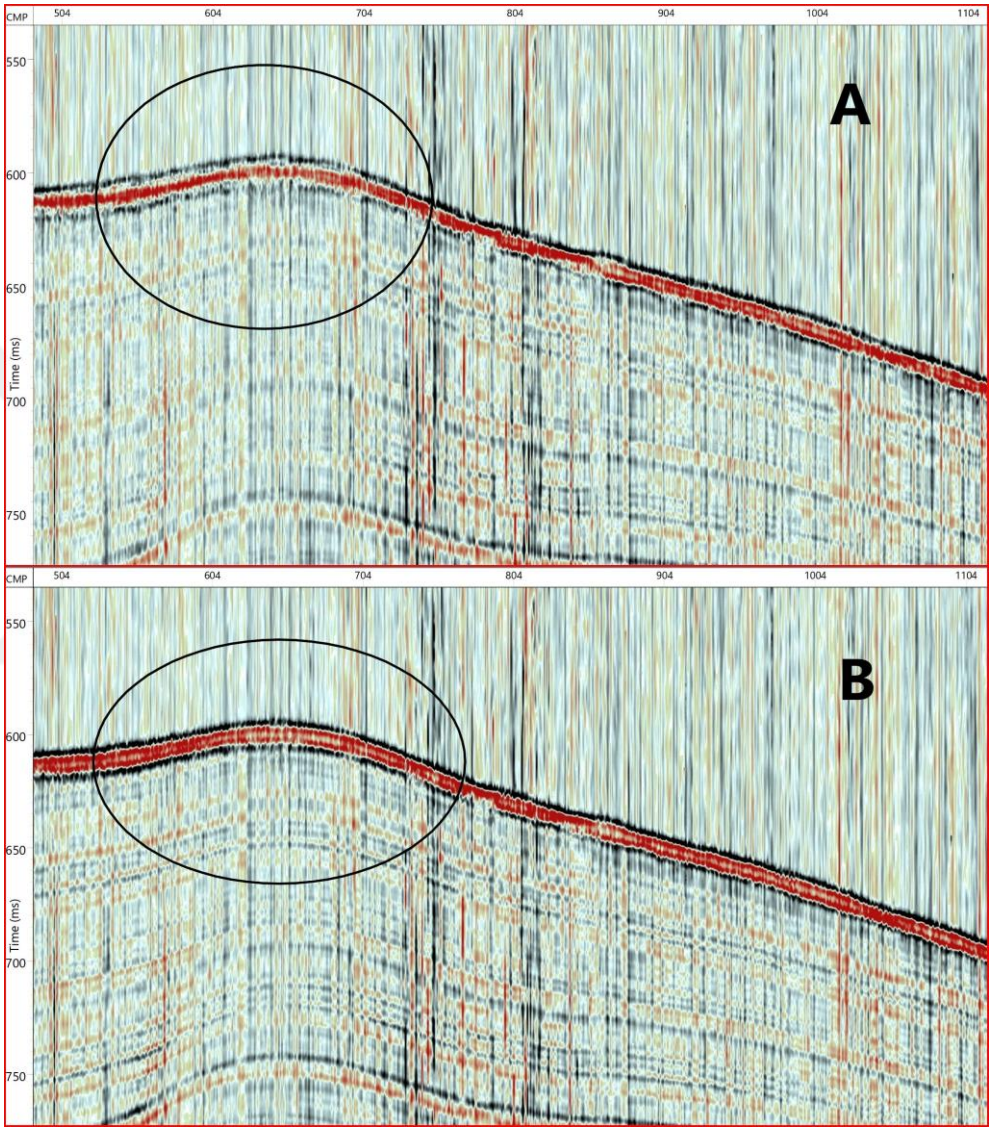

Figure 4.17 Before (A) and after (B) the application of Static Correlation

4.1.11. CMP stack

Common-Mid-Point (CMP) stacking is a vital process to improve the signal-to-noise ratio in the seismic dataset. The stacking process is typically performed after the normal

moveout and static correlation steps. CMP stack worked by stacking traces within each CMP, resulting in one trace per CMP after stacking. Incoherent noise, acquired only on single traces, was reduced, while the signal representing the targeted geology visible on each trace was preserved. Therefore, the signal-to-noise ratio is greatly improved, and the seismic image has become more accurate. After the stacking process, the amount of data is reduced significantly. The stacking is carried out in VISTA using the CMP Stack module with all default parameter settings. The input seismic data was sorted by CMP number. After stacking the data, a trace padding function was usually applied when the data can contain data gaps because of empty CMP bins, but this step wasn't operated in this processing sequence. Figure 4.18 shows an example of the seismic data after the CMP stack.

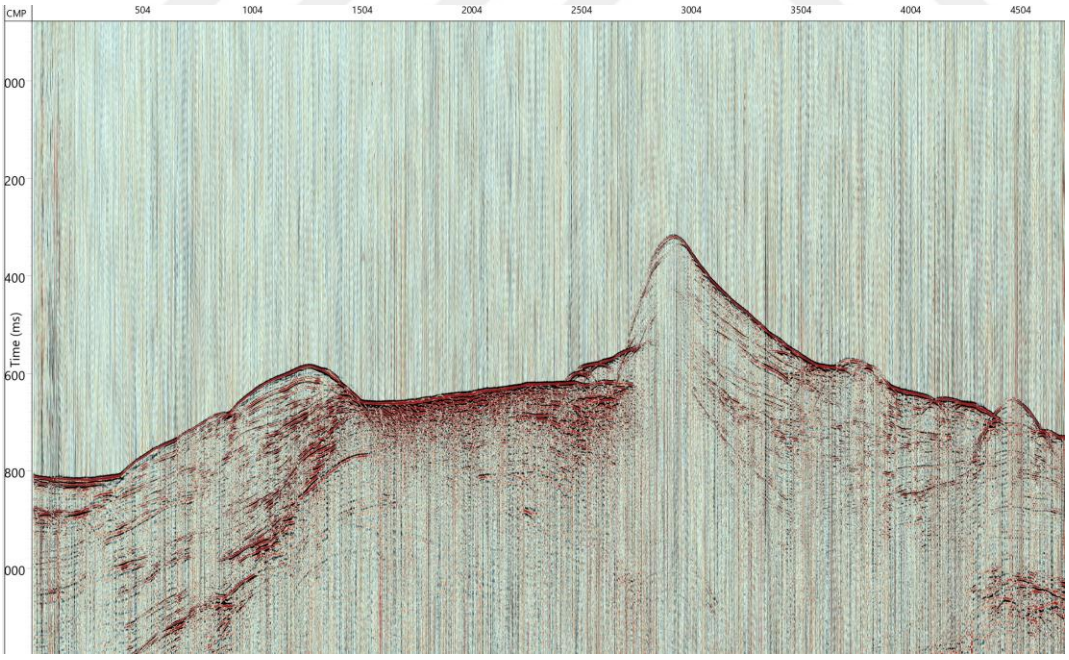

Figure 4.18 Illustration of CMP stacked data. Profile M73-1-GeoB07-226

4.1.12. Ormbsy Bandpass filter

Marine seismic data mainly contains two types of noise classified in coherent and random noise. A frequency spectrum window displays that the 2D seismic dataset is highly affected by low and high-frequency noise (Figure 4.19).

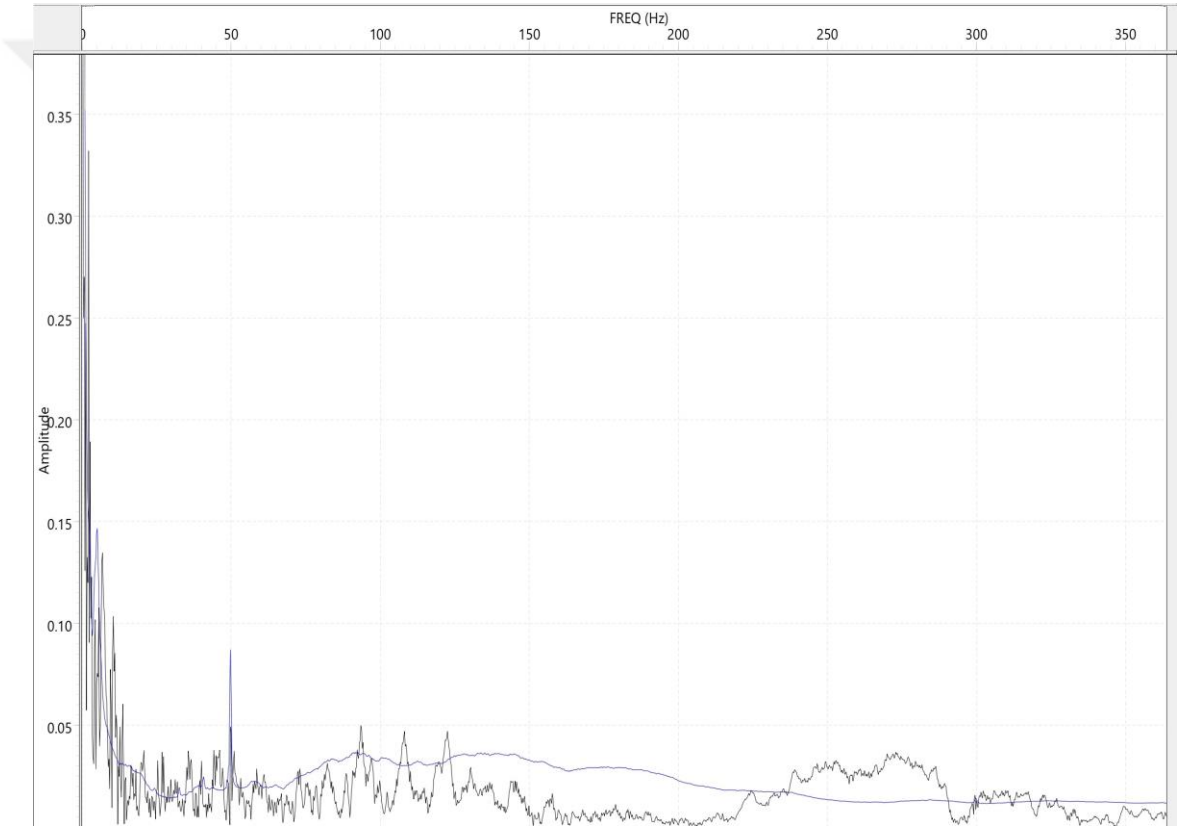

Figure 4.19 Illustration of the seismic frequency spectrum

From different filter mechanisms, here the Ormsby filter was applied to the data. This is due to the specific frequency spectrum of both noise and signal recorded by the hydrophones. The Ormsby band-pass filter consists of four fundamental frequencies (f1, f2, f3, f4). Amplitudes falling below f1 are muted along the entire trace, likewise frequencies exceeding f4.

Therefore, a framework for filtering is built. f2 and f3 define frequencies passing the filter at 100% of their initial amplitude. The frequencies between f1 and f2 and f3 and f4 define frequencies whose amplitude is decreased by filtering. Between f1 and f2, also between f3 and f4, the filter displays a linear function, which describes the residual percentage for the affected frequencies. An Ormsby band-pass filter was applied to remove the noise components using a new Job Flow. For the profile M73-1-GeoB07-282, the used filter settings are summarized in Table 4.4.

Table 4.4 Defined parameters for the Ormbsy band-pass filter.

Used settings	**Parameter**
10	Low Truncation Frequency
55	Low Cut Frequency
90	High Cut Frequency
600	High Truncation Frequency

Due to the late processing stage, the filter is designed not very broad because of losing data. After the filtering process, the results of the frequency filtering are illustrated in figure 25. It can be observed that the overall data quality was improved significantly through the application of the band-pass frequency filter. Especially the lower intervals of the seismic data show an apparent increase in resolution due to the removal of low-frequency noise (Figure 4.20).

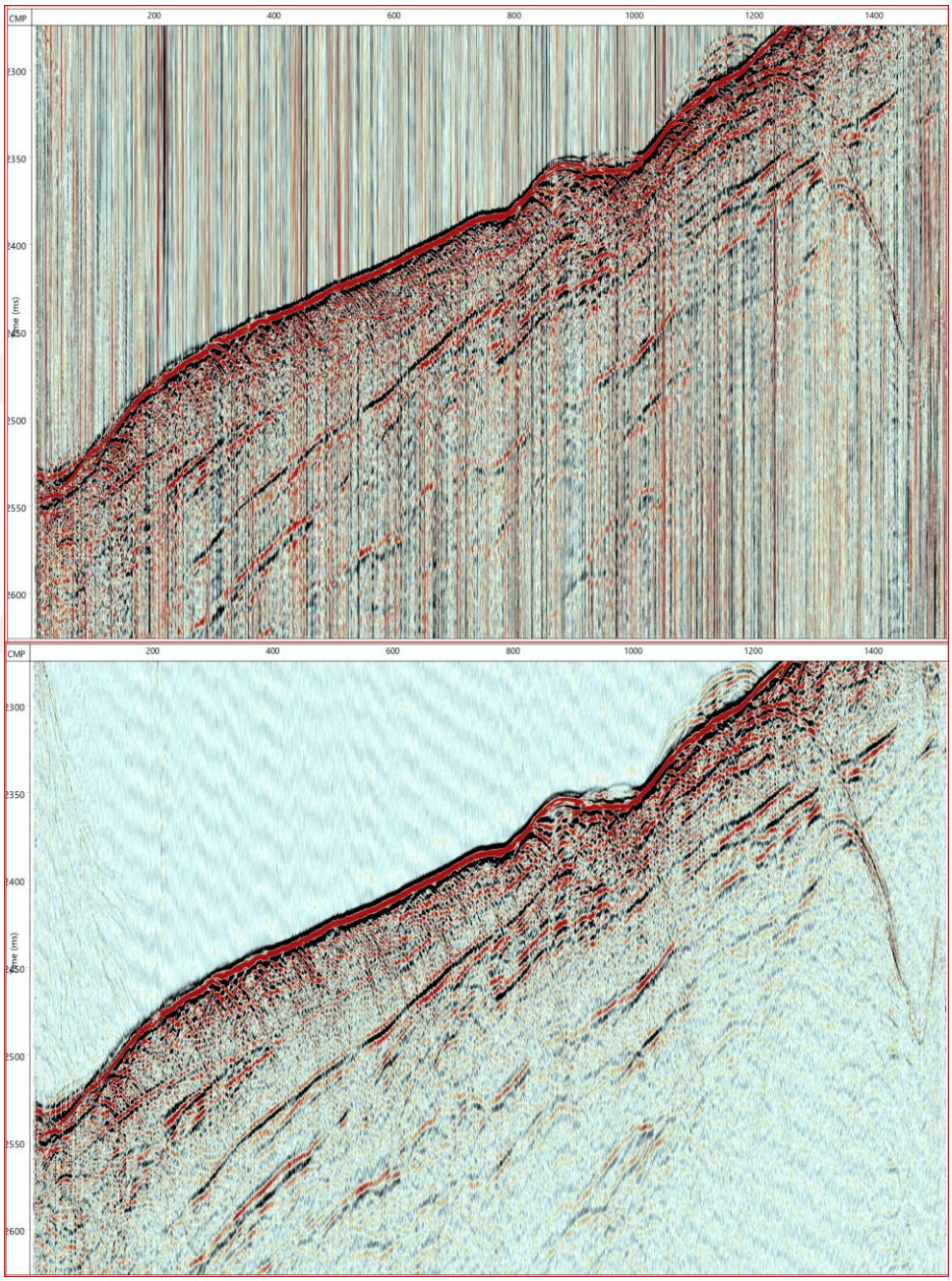

Figure 4.20 CMP stacked profile before (up), and after (down). Profile M73-1-GeoB07-282

4.1.13. Notch filtering

During the marine seismic data acquisition, on-board generators have powerline noise. Then this noise is shown in the amplitude spectrum of the data as spike-like characteristics at 50 Hz frequency. Within a CMP bin, these channels appear as monofrequent noise bursts, often characterized by a much higher amplitude than the background signal. The single-frequency harmonic noise can be eliminated by operating narrow notch filters, which cut out a very narrow frequency band. However, the use of such a filter function can produce so-called "notches" and ringing effects in the amplitude spectrum, which may generate problems during the following processing steps.

Another method to suppress the harmonic noise is THOR module in the VISTA. In THOR, noise is detected by the wavelet's incoherency and a specified time slice throughout a user-defined number of CMPs. Since the targeted noise mainly possessed specific frequencies, THOR was developed to focus on these frequencies (Butler, 2012).

The command works by performing a Fast Fourier Transformations in short time windows to transform the data into the frequency domain. Secondly, the algorithm calculates the median amplitude at each sample and compares it to the actual amplitude value of the trace. If the difference in amplitude exceeds a specified threshold, the trace is replaced by the median value. Therefore, all events that are horizontal and have similar amplitude within a CMP are considered valid signals. A noisy signal is detected by its incoherence and extracted from the data (Figure 4.21).

The THOR module was operated using a new Job Flow and was applied to the latest 2D seismic dataset, the CMP stack. The most critical parameters to specify are the window length, median length, and the analyzed frequency range. All setting parameters of the THOR module are summarized in Table 4.5. Comparing data prior to the application of THOR to data afterward, a significant improvement in both signal-to-noise ratio and a vertical resolution was detectable.

By eliminating the most prominent noise bursts from the dataset, merely background noise emitted from the ship remained. Figure 27 shows that the seismic data is affected by noise.

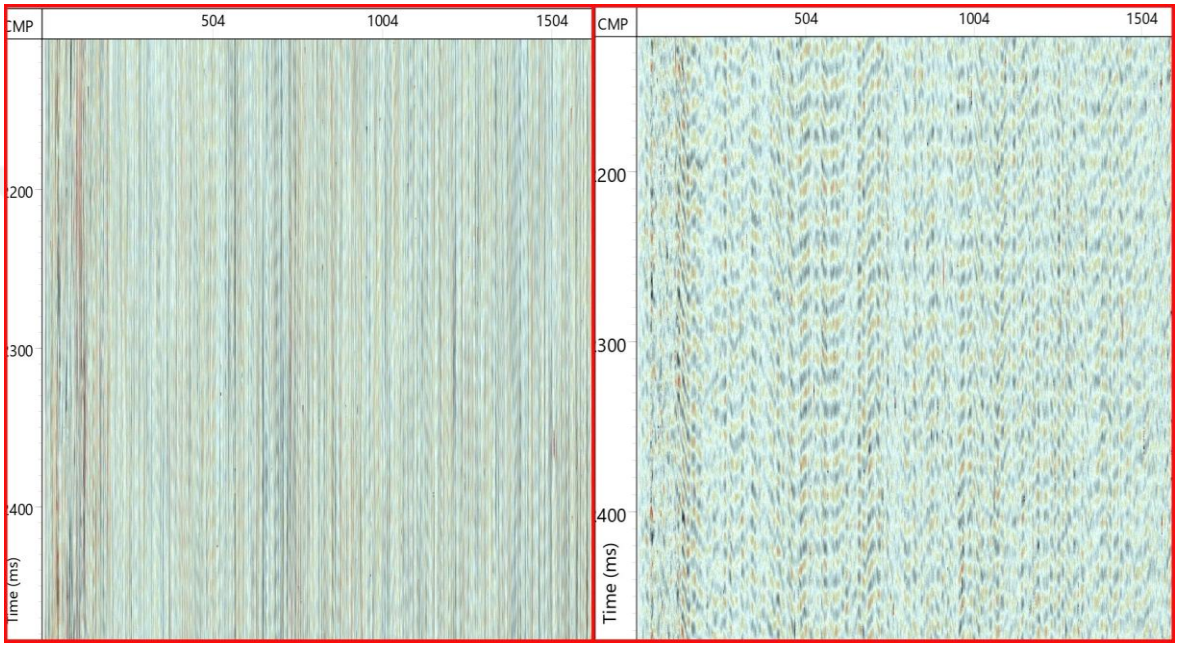

Figure 4.21 Water column of the seismic data. Profile M73-1-GeoB07-226, before (left) and after (right) THOR application.

Table 4.5 Summarized parameters of the THOR function.

Used Setting	Parameter
20 ms	Window Length
3	# of CMP to smash
13	Median Length
3	Attenuation Multiplier
0 Hz	Min. Apply Frequency
800 Hz	Max. Apply Frequency

Figure 4.22 shows that the seismic data is affected by noise. The THOR process was carried out several times using different parameters regarding window length and applied frequency, but still, noticeable artifacts were present in the shallower part.

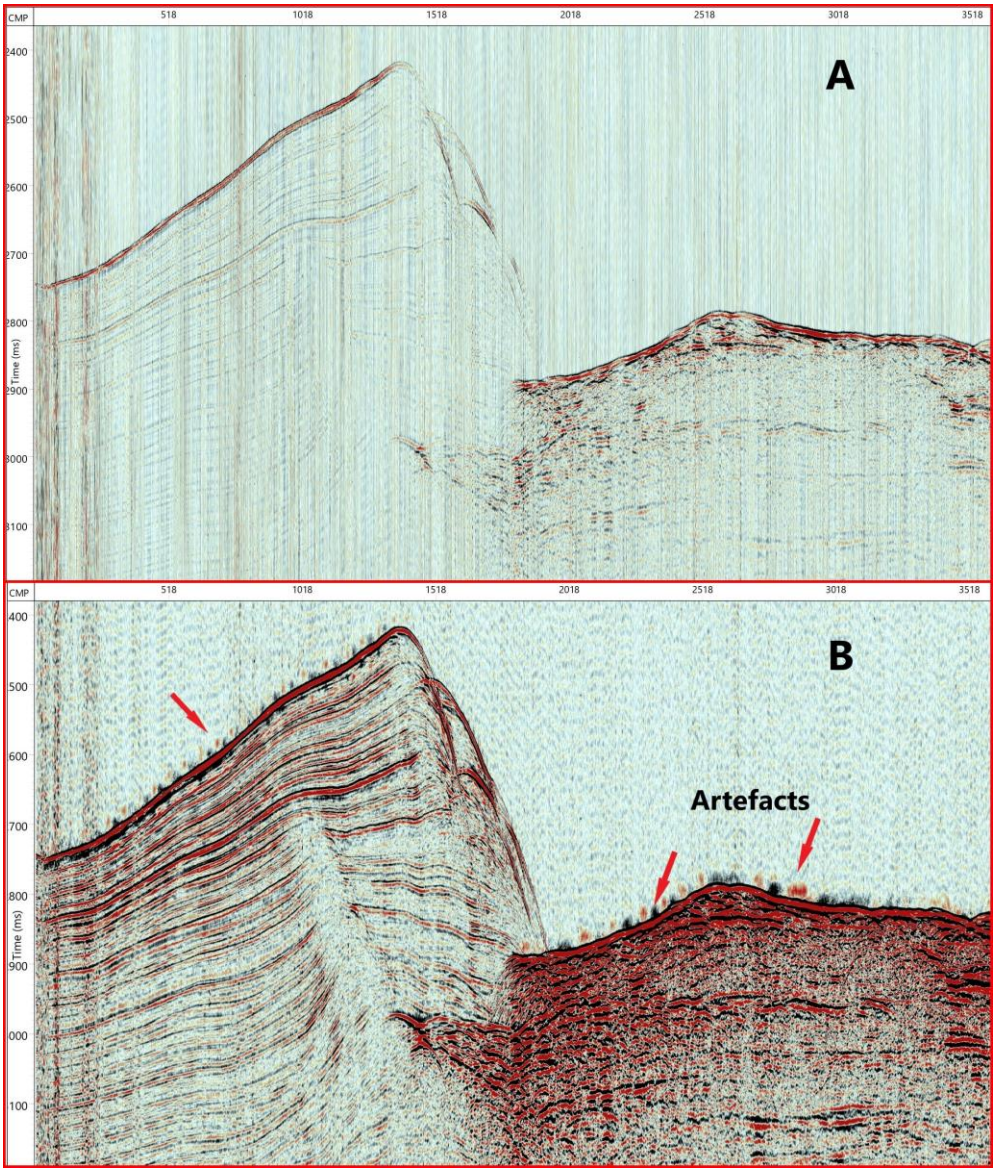

Figure 4.22 Before (A) and after (B) the application of the THOR. The THOR function produced additionial artefacts.

4.1.14. Migration

One of the most crucial steps of seismic data processing is migration. The seismic migration is a process that geometrically re-locates the reflection events in the seismic data to their true subsurface locations in both space and time. After migration, the resulting seismic section typically has an increased spatial resolution due to the collapse of the diffraction pattern(Bonomi & Cabitza, 1993; Yilmaz et al., 2000; Kearey et at., 2002). Further, the length of a reflector is reduced, and the dips are generally increased. Energy, which is smeared along the flanks of a diffraction hyperbola, is recalculated to its true reflection point. The migration process demands a very precise velocity model that optimizes the repositioning of the reflected energy to the correct locations.

There are several different migration algorithms implemented in time or depth domains, which can be applied to seismic data in different processing stages, before or after stacking (Dondurur et al., 2018). The most common migration algorithms in an academic environment, the Kirchhoff Migration and Finite-Difference Migration, were applied to the final stack of the 2D seismic dataset.

The Kirchhoff Migration is based on the summation of amplitudes along the diffraction hyperbola. However, the Kirchhoff migration has restrictions regarding the lateral velocity variations and can generate strong migration artifacts, significantly decreasing the data quality. The Kirchhoff Migration was performed in a New Job Flow with VISTA's Kirchhoff Migration module. One of the most crucial settings for the migration algorithm is the aperture width, which defines the lateral width (in traces) of the diffraction hyperboles in the seismic section. The migration process was tested iteratively with varying parameter settings. All setting parameters of the final 2D Kirchhoff migration are summarized in Table 4.6

Table 4.6 Parameters of 2D Kirchhoff migration module

Used Setting	Parameter
Stacked Data	Data Input
100%	% of RMS Velocity to use
5	Trace distance
35	Max. dip angle
90	Max. (one sided) # of Traces

The Finite-Difference (FD) Migration is based on the solution of the scalar wave equation and the downward continuation of the wavefield towards the reflection point, which is equivalent to the downward movement of the receivers into the subsurface (Claerbout, 1985). Compared to the Kirchhoff migration, the algorithm of the FD migration requires considerably more computing time. It produces good results up to a 65-degree structural dip. The Finite-Difference Migration was carried out in a new Job Flow with the 2D FD Migration module. Necessary settings are to make regarding the trace distance, the maximum dip of reflectors, and the so-called tan step, which defines the finite difference calculation intervals. The migration process was tested iteratively with varying parameter settings. All setting parameters of the final 2D Finite Difference Migration are summarized in table 4.7

Figure 4.23 illustrates a stacked section of line M73-1-GeoB07-292 before and after applying the 2D Kirchhoff migration. Diffraction hyperboles collapsed during the process. Furthermore, the migrated section showed an increased spatial resolution.

However, the 2D Kirchhoff algorithm made a 'ringing' like migration artifacts, which decreased the overall quality of the seismic data considerably (Figure 4.23B).

Table 4.7 Parameters of 2D Finite Difference Migration module

Used Setting	Parameter
Stacked Data	Data Input
100%	% of RMS Velocity to use
4 m	Trace distance
1 ms	Tau Step
50 traces	Taper Pad
Filtered 45-65 degree	Type of Solution

Figure 4.24 shows a stacked section of the line M73-1-GeoB07-224 before and after applying the 2D Finite Difference Migration. The seismic section also shows that the migration process was successful. Diffraction hyperbolas were removed from the data. The overall spatial resolution is increased (Figure 4.24B). A significant difference between the 2D Kirchhoff and 2D FD migration is the amount and appearance of migration artifacts. The FD migration produced significantly fewer migration artifacts compared to the Kirchhoff algorithm.

Figure 4.25 shows a stacked section of the line M73-1-GeoB07-232 before and after applying the 2D Finite Difference Migration. It can be observed that the migration process was also successful. The overall spatial resolution of the seismic section has increased. But, the algorithm produced many migration artifacts in the shape of smiles (Figure 4.25B).

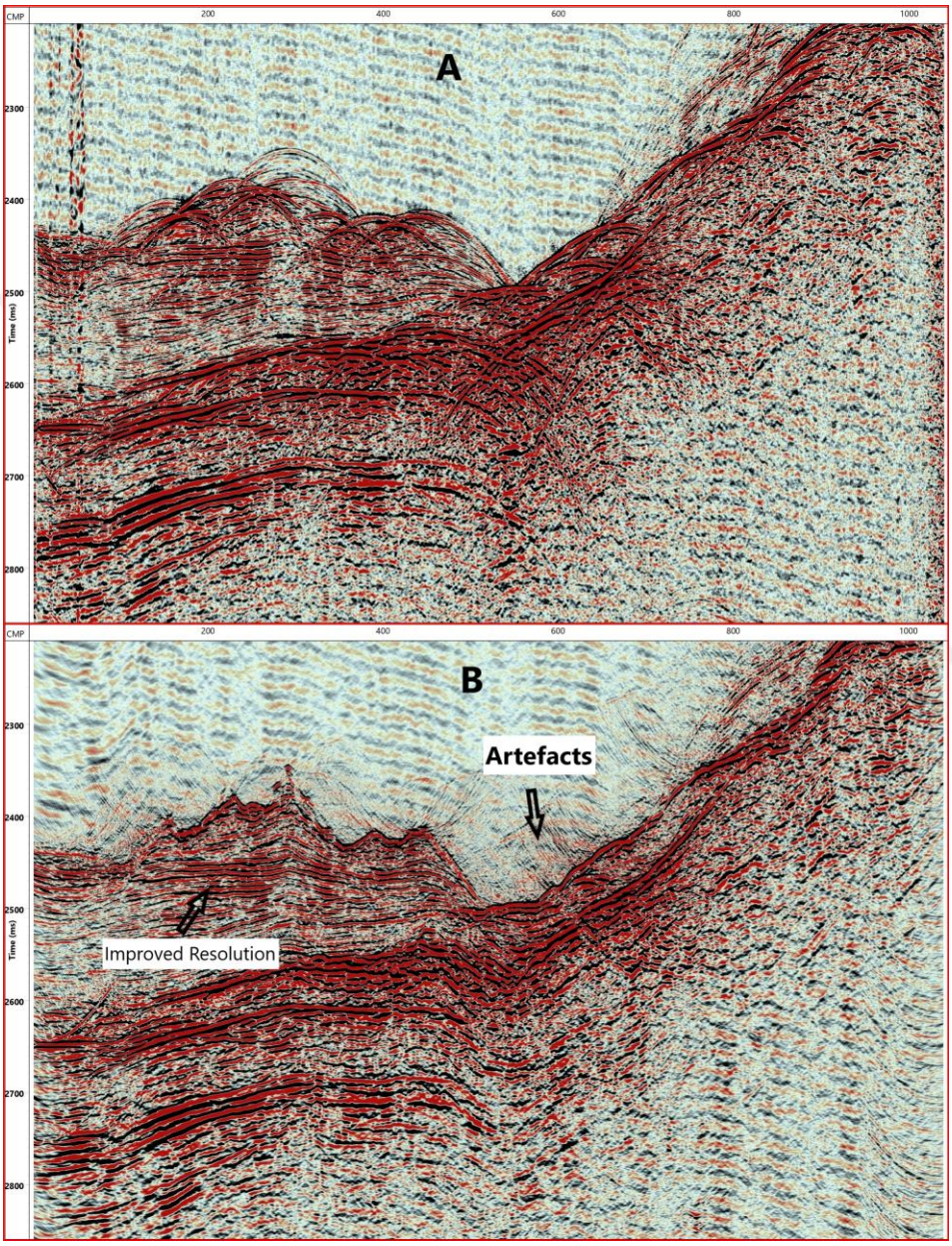

Figure 4.23 Stack section of line M73-1-GeoB07-292 before and after applying the 2D Kirchhoff migration.

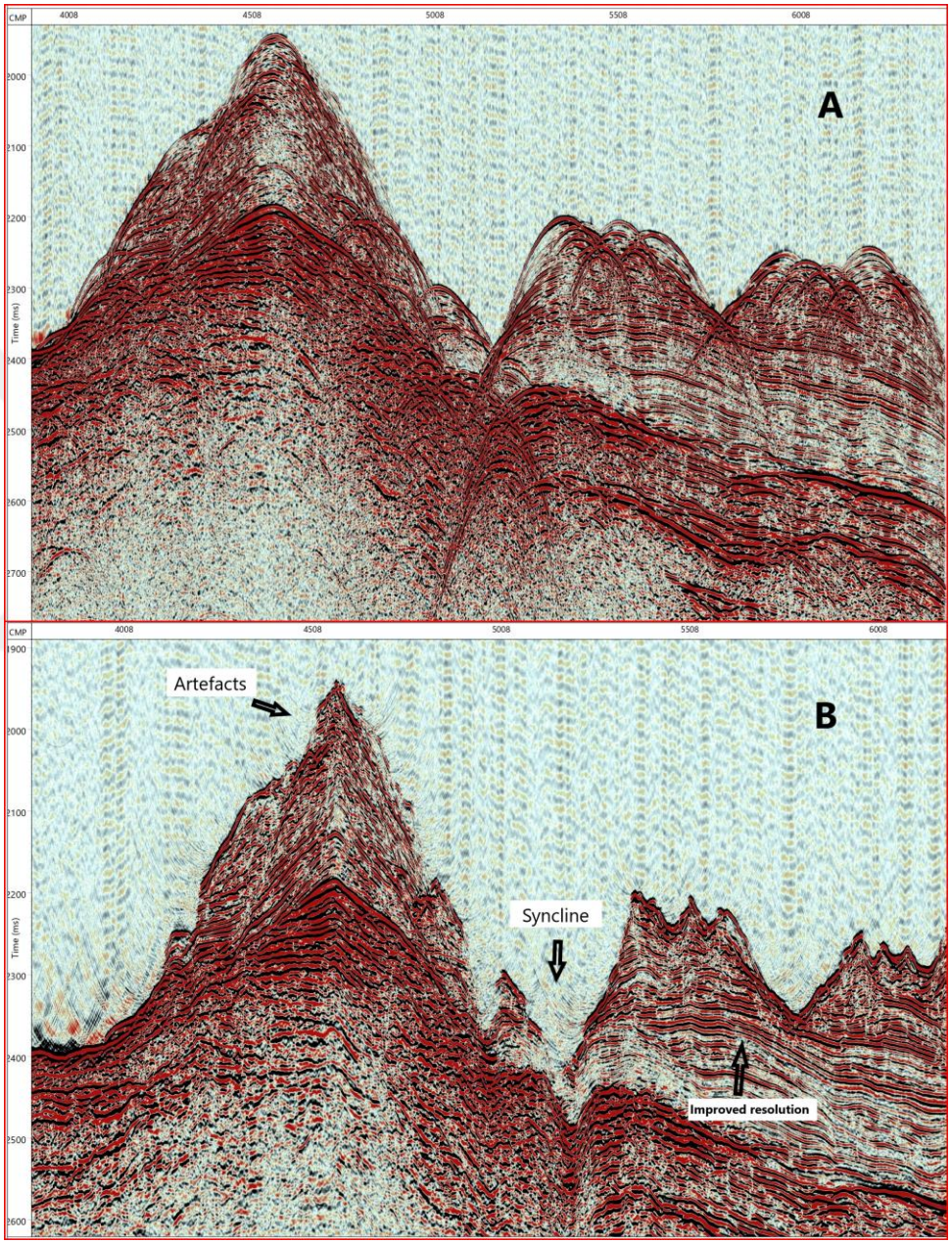

Figure 4.24 Stacked section of the line M73-1-GeoB07-224 before and after applying the 2D Finite Difference Migration.

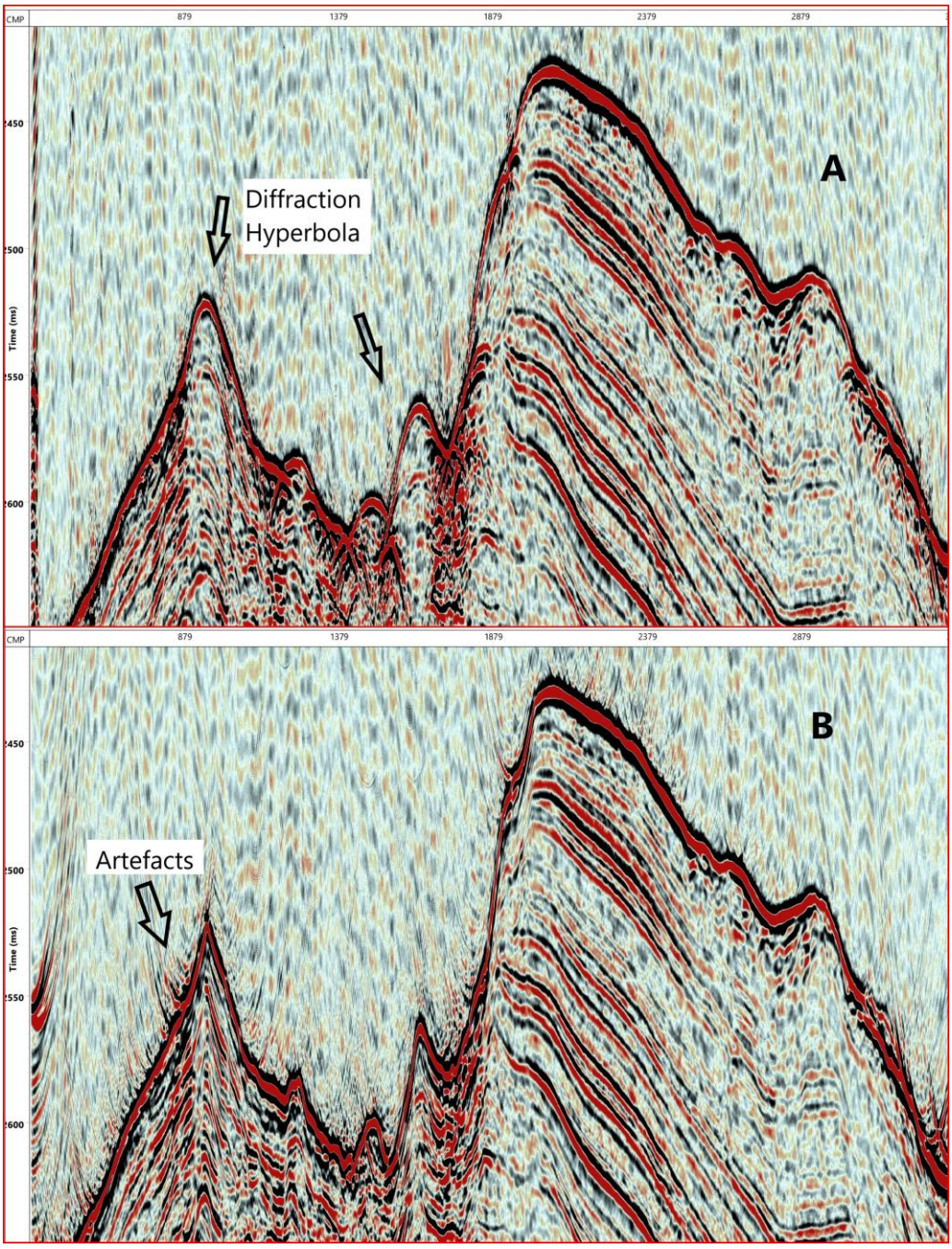

Figure 4.25 Stacked section of the line M73-1-GeoB07-232 before and after applying the 2D Finite Difference Migration

4.1.15. White noise elimination

Marine seismic data can contain so-called white noise, randomly occurring and unpredictable. Eliminating random noise is vital in seismic data processing as it can significantly improve the quality of the data. The white noise suppression was operated by using the module 4D-DEC in VISTA.

Since white noise appears randomly, it is almost impossible to predict it, the 4D-DEC module uses the fact that the noise signal shows a similar appearance in neighboring traces. This information was used to detect and clear the white noise from the data. In detail, the algorithm works by employing principal component decomposition in the time domain. By stacking the traces within a defined time and space window, the principal dip is detected by the sharpness of the resulting stack. The resulting stack is of low frequency because the data is only approximately linear. To produce a high-frequency model, each trace is cross-correlated with the stack. Subsequently, this model is subtracted from the input seismic data. This procedure is repeated three times in a row within the same Job Flow, using varying window lengths and maximum dip settings. The output of the previously run 4D-DEC module was used as input for the next run. The output of the last module, containing the calculated noise component, is subtracted from the original input data using the Subtract Data module in VISTA. All setting parameters for each of the three 4D-DEC modules are summarized in Table 4.8

The results of the 4D-DEC process are illustrated in figures 4.26. Figure 4.26 shows a stacked section of line M73-1-GeoB07-280. In principal 4D- DEC process was successful. Significant parts of the white noise could be removed, resulting in a more precise appearance of the reflectors. But, the algorithm produced some artifacts, which are especially visible in the water column. The resolution of the seafloor reflector was slightly decreased, and a ringing effect of the seafloor reflector was added to the seismic data.

The 4D-DEC process was carried out several times with varying parameters regarding window length and dip.

Table 4.8 Parameters of 4D-DEC module

Used Setting	Parameter
Stacked data	Data Input
100/150/200	Window Length Time (ms)
15/20/25	Window Length Traces
8/8/8	Maximum Dip
25/25/25	Maximum Static
1	Wavelet Amplitude Smoothing
1	Wavelet Static Smoothing
All CMP #	Dip Calculation based on

4.1.16. Exporting data and IHS Kingdom

In order to allow interpretation of the seismic lines processed, each profile has to be exported from VISTA in SGY data format. Subsequently, 17 processed seismic lines were loaded into the IHS Kingdom software. The SGY data has to be assigned to coordinate datasets of the individual lines to achieve the proper geographical positioning of the dataset in the IHS Kingdom.

To interpret the seismic dataset, the IHS Kingdom software was used. Using the IHS Kingdom, an interpretation of the seismically imaged geology of the area of investigation was made possible. The primary approach relied on horizon or fault tracing. Tracing the most important horizons and faults throughout the entire dataset induced the possibility of facies analysis and identification.

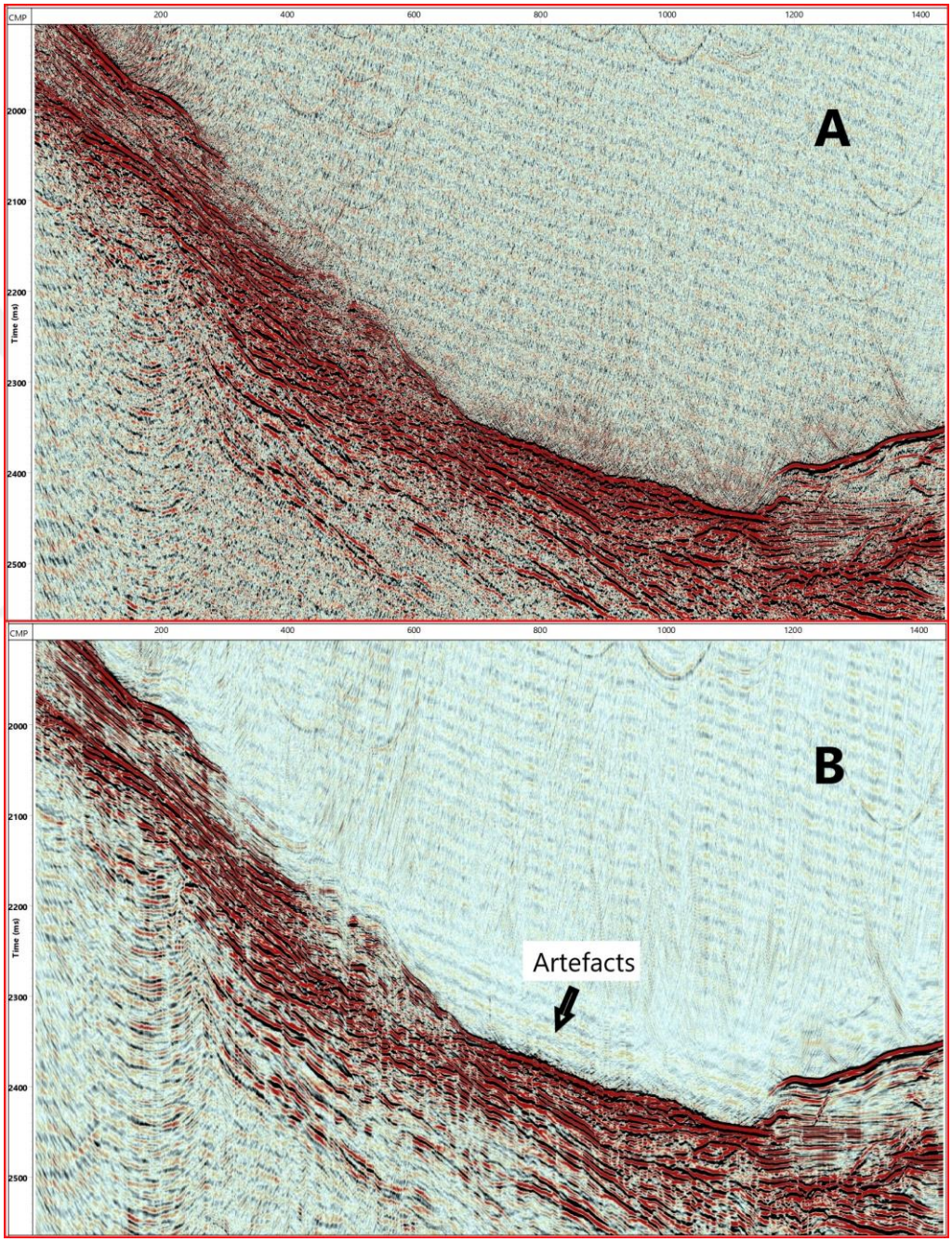

Figure 4.26 Before (A) and after (B) application of the 4D-DEC function.

5. DATA OBSERVATIONS AND DESCRIPTION

To give an insight into the geologic evolution of the study area, the seismic appearance will be investigated and interpreted for lithologic properties. Therefore, seismic facies analysis for understanding the geology is applied. By applying the main principles of seismic facies analysis, hypotheses about the processes affecting the area can be drawn.

The fundamental idea of seismic facies analysis is the concept that seismic reflections compare the stratification of sediments or their post-sedimentary changes, and therefore, e.g., pelagic and hemipelagic sediments, which possess "greater lateral continuity of lithology and physical properties parallel to deposition than across depositional surfaces" (Sangree, 1979). This concept implies that laterally continuous seismic reflections with the same attributes and properties derive from similar depositional environments and have been subject to similar processes (Badley, 1985; Sangree, 1979).

To identify these reflections, computerized attribute identification is applied. Thereby, a given seismic section can be recognized by seismic attributes possessed by individual reflections and the overall configuration and two-dimensional geometry of these reflections as an association of reflections. In seismic facies analysis, the following parameters should be considered: reflection amplitude, frequency, reflection continuity, position (regional setting), external form, internal configuration, reflection termination, size, formation thickness, slope break, reflection smoothness, special waveform pattern, appearance, reflection polarity, an areal association of seismic facies units, an abundance of reflections, line direction (dip or strike section), acoustic impedance, bright spots(e.g., Sheriff and Margaret, 1980; Brown et al., 1982; Badley, 1985; Brown, 2011;).

For sedimentary facies interpretation and seismic facies analysis, the position is a spatial indicator because numerous sedimentary bodies exist in characteristic locations.

For example, large reefs are usually found at continental shelf margins or the edge of platforms (Bubb and Hatlelid, 1977), and deep-water fans are found in deep-sea basins and slopes. Based on the interpretation of the regional seismic line, the position of the seismic facies unit can be defined, after which the sedimentary facies can be concluded according to existing sedimentary facies models (e.g., Berg, 1982; Catuneanu et al., 2009).

The external form of the units was divided into seven classes, i.e., mound, fan, sheet, wedge, bank, lens, and concave (Sangree and Widmier, 1977).

The amplitude of single reflections provides information about the degree of reflectivity related to its reflection coefficient. It is controlled by the contrast of p-wave velocity and the wet bulk density at the individual interface between two media. It is described as high, medium, or low amplitude. High amplitude, for example, hints at a low degree of interbedding of units and resembles clear separability of lithological units (Badley, 1985; Sangree, 1979).

The polarity of a reflection depends on the sign of change in seismic impedance, as a product of p-wave velocity and wet bulk density, and indicates potentially the presence of gas or fluids. The seafloor, for example, holds a positive polarity reflection since the upper layer possesses a lower density than the lower layer, while the transition from gas-free sediments above to gas-bearing reservoir sediment below shows negative polarity (Badley, 1985).

Continuity is closely linked to the degree of consistency of bedding and the steadiness of depositional processes throughout the horizontal extent of a reflector (Badley, 1985).

Reflection frequency in the context of facies analysis is related to geological attributes of the reflectors, e.g., spacing. Thus, it depicts lateral changes in lithology and depositional processes in time (Sangree, 1979).

5.1. Seismic Data Description

The analysis of the seismic reflection profiles in the study area allowed the identification of 5 horizons, 5 major depositional units, and 3 sub-units. Tables 5.1 and 5.2 show details of the analyzed surfaces and units. These analyses are mainly based on the structure, amplitude, continuity, and frequency of reflectors in the seismic sections.

Horizon S (seafloor) is the uppermost reflector in the dataset. It is characterized by a high amplitude reflector, revealing high continuity throughout the dataset. Due to its seismic appearance, horizon S will be referred to as seafloor.

On the profiles at the Middle Valley S horizon running parallel to the slope shows a general trend of tilt increase towards the north and north-east. In the profile M73-1-GeoB07-234 (Figure 5.8), because of the topography, Horizon S rapidly increases towards the north from a depth of 2750 ms TWT to 2400 ms TWT. However, in the direction north, this increase terminates at an abrupt drop in depth from about 2400 to 2900 ms TWT over a horizontal distance of 1800 m. Further to the north of that drop, a minor rise of about 100 ms TWT can be detected on Line M73-1-GeoB07-234 (Figure 5.8). Following the rise, further to the north and north-east, on Lines GeoB07-226, 228, 234, Horizon S shows an almost horizontal trend continuing at a depth of between 2800 and 2650 ms TWT.

On the Slide Complex area, Horizon S shows an entirely different trend. It is almost impossible to follow Horizon S on the way to the south and east parts of the lines because of its low frequency and low amplitude. On the profile M73-1-GeoB07-224 (Figure 5.11), Horizon S decreases its depth from 2350 ms TWT to 1950 ms TWT and again dips rapidly towards the east at a depth of 2400 ms TWT and this change happens over a horizontal distance of 4000 m.

Location		Reflection characteristics	Geometrical characteristics	Seismic Units		Color code
Upper Valley	Middle Valley			Example from data	Name	
At signal penetration limit	Yes	Low Frequency, Low to Medium Amplitude, Semi-continuous, Reflection-less to Subparallel reflectors	Concordant, bounded by H1	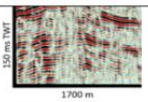	PRE-MES	Light Pink
At signal penetration limit	Yes	Medium Frequency, High to Medium Amplitude, Semi-continuous, Subparallel to Hummocky reflectors	Bounded by H2 and H1	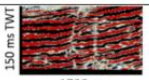	U-1	Light Orange
Yes	Yes	Medium Frequency, Low Amplitude, Continuous, Parallel reflectors	Bounded by H3 and H2	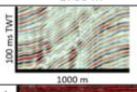	U-2	Light Blue
Yes	Yes	Medium to High Frequency, Medium to High Amplitude, Continuous reflectors		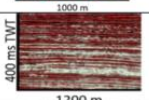	U-3	
		Medium to High Frequency, Medium to High Amplitude, Continuous, Parallel to slightly Divergent reflectors	Bounded by H4 and H3	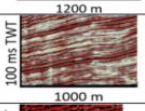	U-3A	Dark Green
		High Frequency, High amplitude, Semi-continuous to Discontinuous, Subparallel reflectors	Bounded by Seafloor and H3	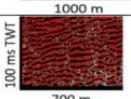	U-3B	Yellow
		High Frequency, High amplitude, Continuous, Parallel reflectors	Bounded by H5 and Seafloor	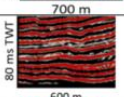	U-3C	Light Green
Yes	No	Low to Medium Frequency, Medium to High Amplitude, Discontinuous to Semi-	Bounded by Seafloor and H5	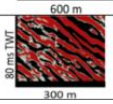	U-4	Red

Table 5.1 Identified depositional units from the study area.

Surfaces		Seismic descriptions	Color code
Label	Name		
H1	Horizon 1	Low Amplitude, Discontinuous	Dark Blue
H2	Horizon 2	Medium to High Amplitude, Semi-continuous, Subparallel to the H1	Red
H3	Horizon 3	Medium Amplitude, Continuous, Subparallel to the H2	Blue
H4	Horizon 4	High amplitude, Continuous, Parallel to the seafloor	Pink
H5	Horizon 5	Low amplitude, Semi-continuous	Light Green
S	Seafloor	High amplitude, Continuous, Effected by side echoes	Green

Table 5.2 Identified surfaces, reference from Figure 5.8, 5.9, 5.10, 5.11

After passing Upper Valley Horizon S is losing its depth from 2350 ms TWT to 1950 ms TWT and again dipping rapidly towards to east at a depth of 2400 ms TWT, and this change happens over a horizontal distance of 4000 m. Further to the east, it decreases depth again, and from 2200 ms TWT until the end of the profile shows slight, rapid changes like up and downs. On lines M73-1-GeoB07-276 (Appendix x) and M73-1-GeoB07-304 (Figure 5.10), Horizon S has a general trend of dipping towards the south. On profile M73-1-GeoB07-304 (Figure 5.8), Horizon S is dipping moderately towards the south throughout the whole profile. It is increasing its depth from 1700 ms TWT to 2700 ms TWT.

Figure 5.1 shows the depth maps of Horizon S. It is observed all over the study area. The surface generally dips to the south and southeast. The depth range is increasing from the Upper Valley to the Middle Valley. Depth varies from 1.526 s TWT in the north to 2.895 s TWT towards the south.

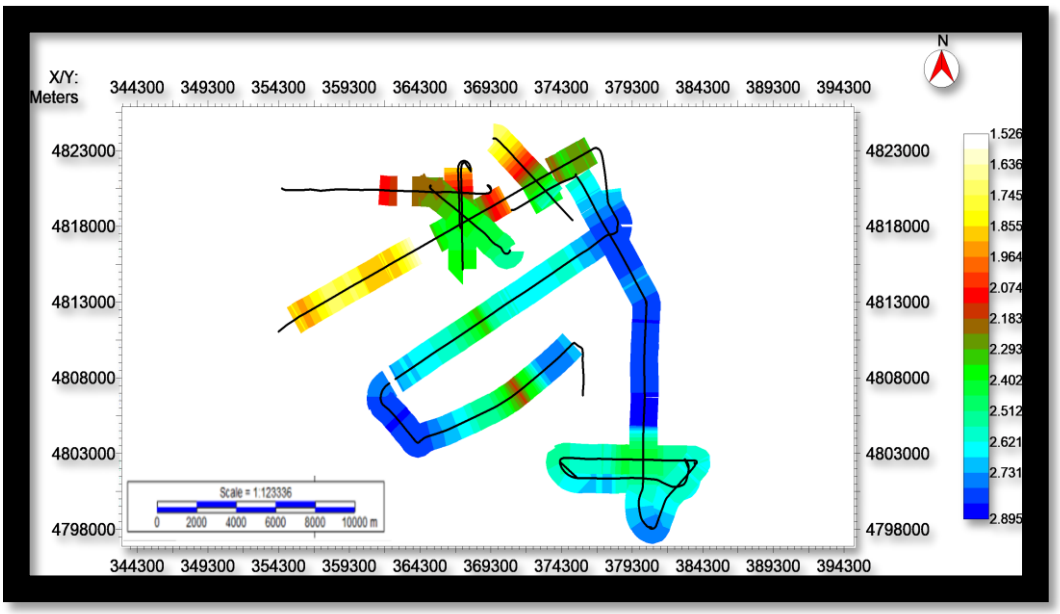

Figure 5.1 Depth map of Horizon S (seafloor). Colorbar unit is TWT (s).

Horizon H5 shows a low amplitude and semi-continuous to continuous reflection. It crosses seismic units U-3C and U-4. Erosive features were observed on Horizon H5 on profile GeoB07-304 (Figure 5.8). Horizon H5 is less widespread, mainly focused on an area of Slide complex and dipping towards the south.

Horizon H4 exhibits a completely different seismic appearance from Horizon H5. Horizon H4 shows a medium to high amplitude reflection. Throughout the entire dataset, it displays high continuity and parallels to the seafloor. Horizon H4 crosses seismic unit U-3 and all subunits of it: U-3A, U-3B, and U-3C. It is located 100-120 ms TWT below Horizon H5. In some areas, this difference becomes even less than 50ms TWT.

Figure 5.2 demonstrates the depth map Horzion H4. The surface is mainly detected in the north, north-east, and south directions. Horizon H4 is visible only in two profiles towards the west.

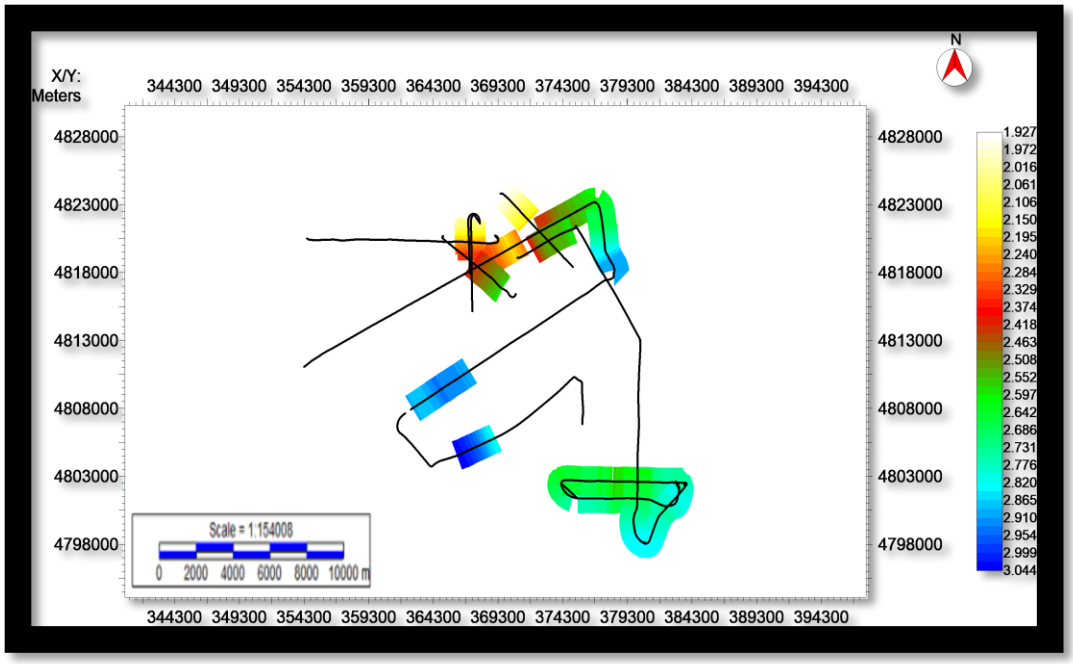

Figure 5.2 Depth map of Horizon H4. Colorbar unit is TWT (s).

Horizon H3 displays medium amplitude and semi-continuous to continuous reflection. It is subparallel to the Horizon H4 and located 200-400 ms TWT below it (Figure 5.3). It is the second most observed surface in this study. Depth ranges from 2.093 s TWT in the north to 3.220 s TWT towards the south.

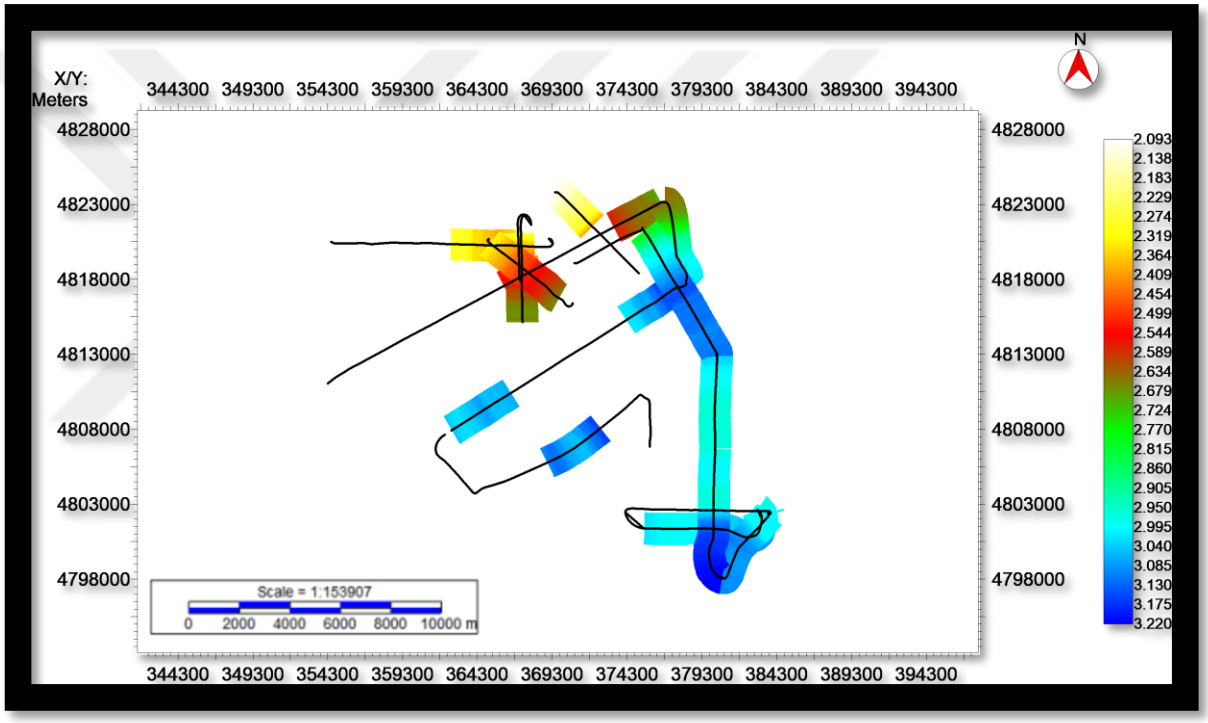

Figure 5.3 Depth map of Horizon H3. Colorbar unit is TWT (s).

The seismic appearance of *Horizon H2* is medium to high amplitude. It shows semi-continuous reflection. It is located 300 ms TWT below Horizon H3 and is widely spread, especially in the Middle Valley area (profile GeoB07-234, Figure 5.8).

Horizon H1 is only distributed in the Middle Valley area. Even in this area, it is challenging to follow Horizon H1 because it shows the low amplitude and discontinuous reflection.

5.1.1. Seismic Units

Seismic Unit Pre-Mes

The seismic appearance of Seismic Unit Pre-Mes (Savoye is dominated by low to medium amplitude reflectors (Figure 5.8 and 5.9). Continuity of individual reflectors within Seismic Unit Pre-Mes is semi-continuous. The frequency of reflectors throughout the unit is low. Configuration of reflectors in Seismic Unit Pre-Mes changes from reflection-less to subparallel reflectors (Figure 5.8 and 5.9).

Seismic Unit U-1

Throughout Seismic Unit U-1, the configuration of reflectors shows medium frequency. Reflector amplitude is high to medium (Figure 5.8, 5.9 and 5.10). Continuity of individual reflectors within Seismic Unit U-1 shows semi-continuity. Configuration of reflectors in Seismic Unit U-1 is characterized by subparallel to hummocky reflectors (Figure 5.8, 5.9 and 5.10).

Seismic Unit U-2

Seismic Unit U-2 shows low amplitude reflectors. Throughout the unit, reflectors are continuous (Figure 5.8, 5.9, 5.10 and 5.11). The reflector configuration shows a medium frequency of reflectors. Configuration of reflectors is characterized as parallel (Figure 5.8, 5.9, 5.10 and 5.11).

Seismic Unit U-3

A medium to high reflector frequency characterizes seismic Unit U-3 frequency (Figure 5.8, 5.9, 5.10 and 5.11). The reflectors composing Seismic Unit U-3 show semi-continuity to continuity throughout the unit. Furthermore, Seismic Unit U-3 is characterized by medium to high amplitude reflectors. Because of changing reflector amplitude and configuration Seismic Unit U-3 can be divided into 3 separate subunits due to their seismic appearance:

- **Seismic Subunit U-3A** is characterized by medium to high amplitude and frequency reflectors, which show parallel to slightly divergent layer configuration within the layers (Figure 5.8, 5.9 and 5.10).
- **Seismic Subunit U-3B** incorporates reflectors showing the highest amplitude throughout the dataset. Reflectors composing the subunit show subparallel layering. Continuity is semi-continuous to discontinuous (Figure 5.8 and 5.11).
- **Seismic Subunit U-3C** is characterized by high amplitude reflectors showing parallel reflection configuration. Seismic Subunit U-3C is represented by higher amplitude and frequency reflectors, while reflector configuration is parallel (Figure 5.8, 5.9, 5.10 and 5.11).

Seismic Unit U-4

Throughout Seismic Unit U-4, the configuration of reflectors shows low to medium frequency. The seismic appearance of Seismic Unit U-4 is dominated by medium to high amplitude reflectors. Reflectors are discontinuous to semi-continuous. The configuration of reflectors is convergent(Figure 5.10 and 5.11).

5.1.2. Spatial distribution of Seismic Units

Seismic Unit U-1

As going more deeper through TWT, the seismic dataset becomes more reflection-less and thus makes it challenging to identify units, and Seismic Unit U-1 is also one of them (Figure 5.4). It is only determined in the southern lines beneath the area of Middle Valley. Thickness ranges from 0.175 s TWT in the north to 0.329 s TWT.

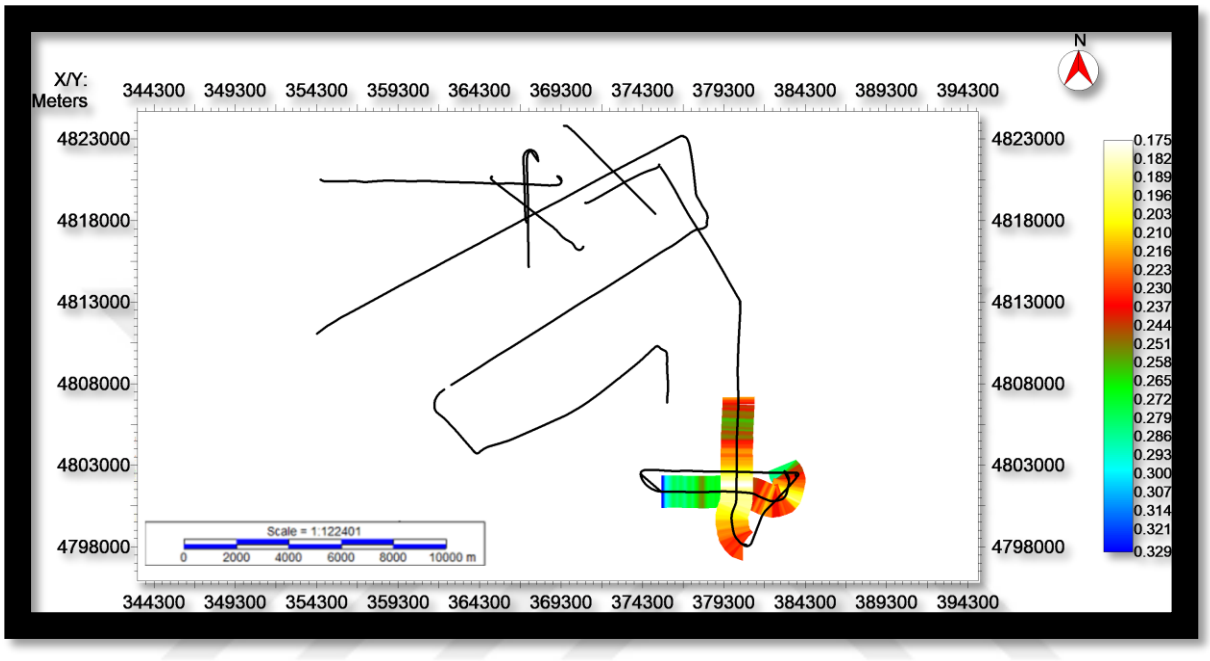

Figure 5.4 Thickness map in (s) TWT of Seismic Unit U-1.

Seismic Unit U-2

Horizon H2 and Horizon H3 bound this seismic unit U-2 entire study area. At its southern end, Seismic Unit U-2 is inclined towards the southeast.

Seismic Unit U-2 is only determined in a few lines on the north. The TWT is lowest in the north direction, increasing towards the south (Figure 5.5). Regarding the thickness of the Seismic Unit U-2, it remains constant at around 0.212 s TWT in the E-W direction.

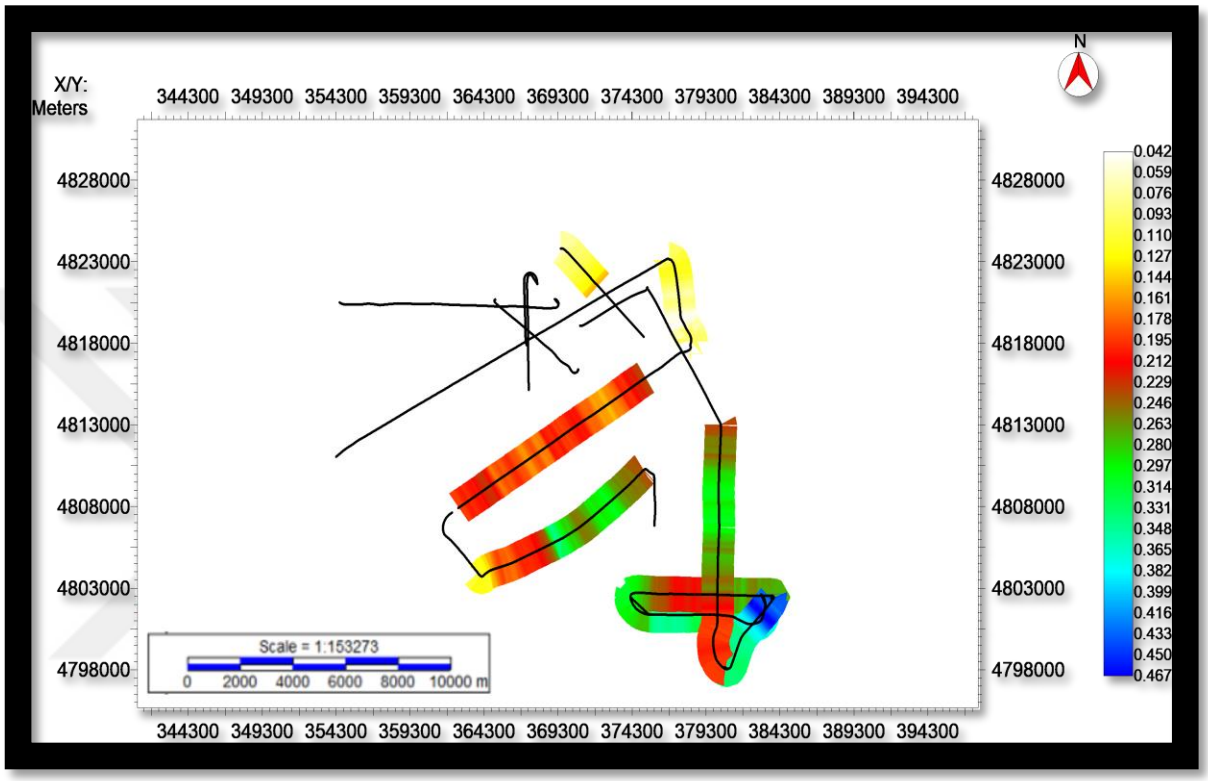

Figure 5.5 Thickness map in (s) TWT of Seismic Unit U-2.

Seismic Unit U-3

Seismic Unit U-3 can be detected all over the study area. Both horizontal and vertical distribution of Seismic Unit U-3 and its corresponding subunits in the study area is characterized by a higher variation in N-S and E-W directions which indicates that the thickness of Seismic Unit U-3 is controlled by the underlying topography of horizon H3. Seismic Unit SU1 and its subunits show an inclination towards the south direction. Seismic Unit SU1 shows the lowest depth at around 0.040 s TWT in the northwest direction. To the south, the TWT of Seismic Unit SU1 increases along the southward inclined southern terrace (Figure 5.6).

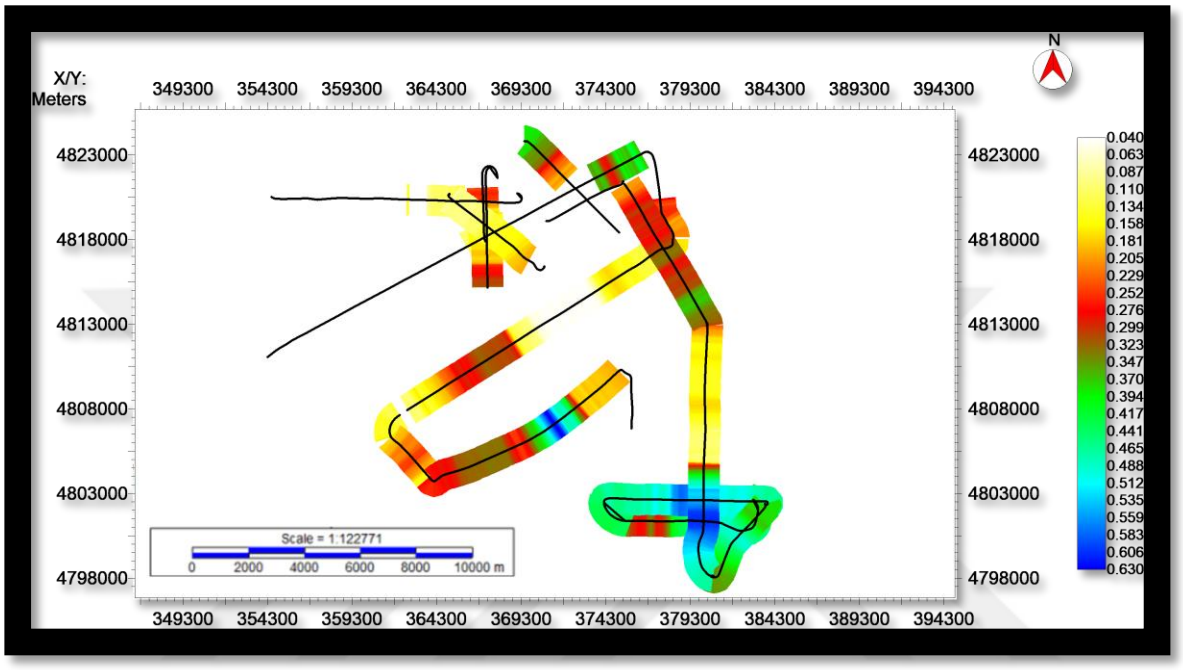

Figure 5.6 Thickness map in (s) TWT of Seismic Unit U-4.

Seismic Unit U-4

Seismic Unit U-4 is concentrated on the area of slide-dominated topography on the north-eastern lines and mostly on line M73-1-GeoB07-224, 276, 304 (Figure 5.8; 5.10; Appendic x). Isopach map demonstrates that the TWT is lowest in the west and increasing again towards the east (Figure 5.7). N-S variation of Seismic Unit U-4 over neighboring lines is quite low. Thickness in this unit is also controlled by the topography of the unit's base, Horizon H5.

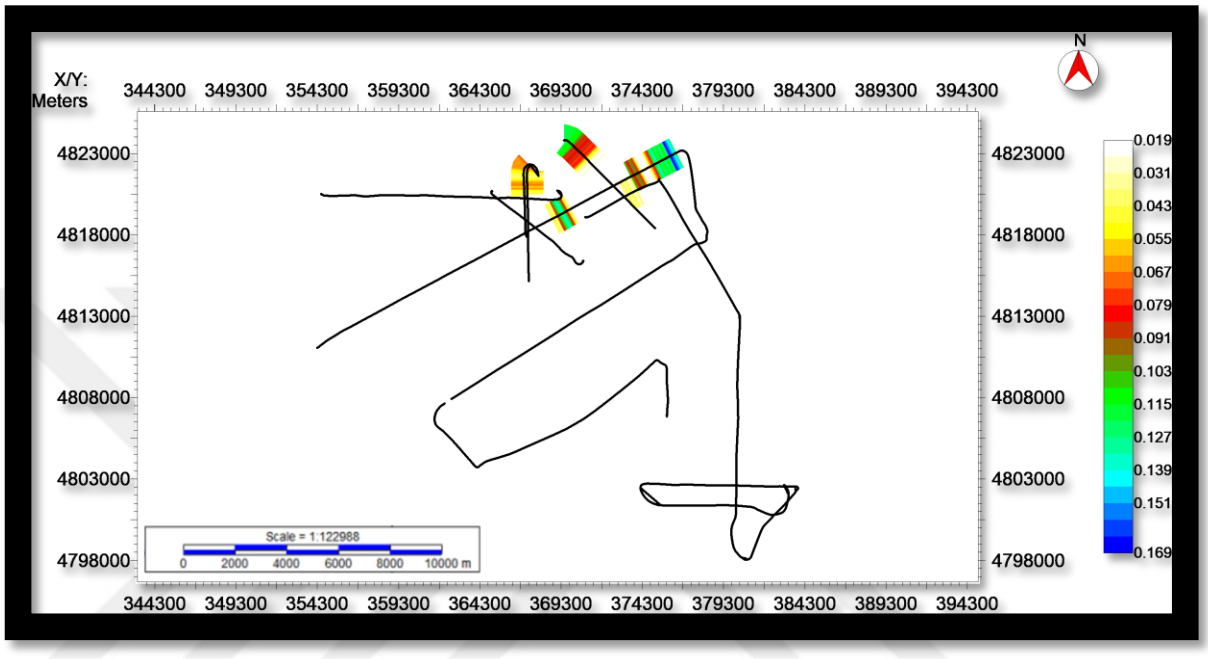

Figure 5.7 Thickness map in (s) TWT of Seismic Unit U-4.

5.1.3. Exemplary Profiles

Profile M73-1-GeoB07-234

The distribution of seismic units on Line M73-1-GeoB07-234 is characterized by the separation of the line into two different areas. The VSR is the southernmost area, followed by the area of Middle Valley in the north (Figure 5.8; Appendix x).

The VSR is dominated by Seismic Unit U-3 and its corresponding Seismic Subunits U-3A and U-3C. Beneath the seafloor, Seismic Subunit U-3A shows a thickness of 100 ms TWT throughout the VSR area (Figure 5.8). It is truncated by the seafloor at the transition to the area of Middle Valley in the center of the line.

Its top boundary is the seafloor, while the bottom boundary is a high amplitude concordant reflection Horizon H4 towards the transition area (Figure 5.8). Seismic Subunit U-3A shows a thickness of 350 to 400 ms TWT over the VSR area. At the transition to the area of Middle Valley, Seismic Subunit U-3A ends 100 ms TWT down to the seafloor, and Seismic Subunit U-3B starts. It continues until the end of the line with a thickness of around 100 to 200 ms TWT (Figure 5.8). The base of Seismic Subunit U-3B and U-3A is the same and given by a concordant medium amplitude, continuous reflector Horizon H3. Beneath, Seismic Unit U-2 can be detected throughout the whole profile, revealing a thickness of 200 to 250 ms TWT. It is bounded by Horizon H2 from below, which is configurated medium to high amplitude and semi-continuous reflection. Under this horizon, Seismic Unit U-1 was revealed, and as Seismic Unit U-2, it also covers the entire profile. The inner structure of unit U-1 is dominated subparallel to hummocky.

The lowermost part of the profile is identified as Seismic Unit Pre-Mes. The base of Seismic Unit Pre-Mes is marked by the limit of penetration of the seismic dataset. Its top boundary is Horizon H1 which is only followed from south to the middle of the line

because of low amplitude and discontinuous reflection. The geometry of the Seismic Unit Pre-Mes, however, shows wavy characteristics reflection-less to subparallel reflectors.

Profile M73-1-GeoB07-231

Line M73-1-GeoB07-231 is located along the VSR. From west to east, these areas are VSR zone (Figure 5.9). Distribution of seismic units changes along the line between areas. Beneath the seafloor, Seismic Subunit U-3C is most abundant. It reveals a thickness of 120 to 150 ms TWT, decreasing towards the west (Figure 5.9). At the bottom, it terminates at a high amplitude Horizon H4 reflection (Figure 5.9). Seismic Subunit U-3A decreases in thickness from 300 ms TWT in the east to about 200 ms TWT in the west, entire the profile. The geometry of the seismic unit is subparallel to parallel, well-layered reflections. The lower termination of the seismic unit is characterized by a subparallel medium amplitude reflection Horzion H3 (Figure 5.9). Beneath, Seismic Unit U-2 is defined. Its thickness remains almost the same from west to east at around 300 ms TWT and is running parallel to the Seismic Units U-3A. The inner structure differs because of less amplitude than the upper units. The base of the U-2 is marked by a medium to low amplitude concordant reflector Horzion H2.

Beneath Seismic Unit U-2, Seismic Unit U-1 has been detected. It shows a thickness of 300 ms TWT, thinning towards the east. At the lowermost part of the line (3800 ms TWT to down), Seismic Unit Pre-Mes is revealed. Its base is given by the limit of penetration of the seismic system.

Profile M73-1-GeoB07-304

Line M73-1-GeoB07-304 is crossing the area of the Slide complex; that is why separation of the line is not necessary (Figure 5.10). The line exclusively shows seismic units covering the slide area.

The uppermost unit is Seismic Unit U-4 which toplaps the seafloor. It starts at 1700 ms TWT and decreases until 2400 ms TWT, dipping to the southwest. It shows a thickness of about 100 ms TWT in the northwest direction, and throughout the seismic line is thinning towards to southwest (Figure 5.10). It vertically enters other lines and truncates them. The vertical distribution is changing 300 ms TWT down, but horizontally it does not reach even until the end of the profile. The geometry of reflectors is convergent at Seismic Unit U-4. The base is given by a low amplitude semi-continuous reflection Horzion H5 which is hard to follow, and by Horizon H3 towards to southwest.

Beneath, Seismic Subunit U-3C comes. This unit shows a thickness of less than 100 ms TWT, and it covers the area of one-third of the profile (Figure 5.10). Its lower bound is a high amplitude reflector Horzion H4. As Horzion H5, Horzion H4 also ends near to middle of the profile. Then Seismic Unit U-3A is identified. It has a 250 ms TWT thickness and truncates by Seismic Unit U-4 at the 3500 m horizontal distance. This unit's base is Horizon H3 which is difficult to follow towards the southwest. Seismic Unit U-2 starts with 100 ms TWT thickness at the northwest. To the southwest direction, it is thickening and reaches around 300 ms TWT. Only a little part of Seismic Unit U-3B with the thickness of 150 ms TWT is detected at the southwest. Its reflectors onlap the Seismic Unit U-2. Its top boundary is seafloor, but because of rough topography, the seafloor was not tracked in the southwest direction. As going down through TWT, Seismic Unit U-1 was identified with more than 100 ms TWT thickness. The top boundary is Horizon H2 with medium to high amplitude. Its base and the deeper structures are not imaged well because of the limit of penetration of the seismic system.

Profile M73-1-GeoB07-224

Line M73-1-GeoB07-224 is the longest seismic profile in this study, approximately 26.5 km. Only half of the profile, especially the northeast part, was studied. The distribution of seismic units on Line M73-1-GeoB07-224 is characterized by the separation of the line into two different areas. The Upper Valley area is the southwest area, followed by the area of the Slide complex towards the northeast (Figure 5.11).

Seismic Subunit U-3B dominates the Upper Valley. Beneath the seafloor, Seismic Subunit U-3A shows a thickness of 200 ms TWT throughout the Upper Valley (Figure 5.11). Its top boundary is seafloor, and a base boundary is a medium amplitude and semi-continuous reflection Horizon H3 (Figure 5.11). Beneath, Seismic Unit U-2 can be detected in the Middle Valley, revealing a thickness of 150-200 ms TWT. Due to the reflection-less seismic data set, it is challenging to identify base boundary and lower seismic units.

In the area of Slide Complex, Seismic Unit U-4 is the uppermost unit. Its top bound is seafloor. At the beginning of the Slide Complex area, because of the anticline shape of the unit, it is hard to define the thickness of the unit. Towards the northeast, the unit gets a thickness of around 100 ms TWT. The unit's base is low amplitude and semi-continuous reflection, Horzion H5.

Below, Seismic Unit U-4 is dominated by Seismic Unit U-3 and its corresponding Seismic Subunits. Seismic Subunit U-3C is present in the area. It shares the same distribution as Seismic Unit U-4. First, it shows an anticline shape, and as going further to the northeast, it gets a thickness of 120 to 150 ms TWT. Horizon H4 with the medium amplitude is the base of Seismic Unit U-3C. Then Seismic Subunit U-3B is detected. It runs from southwest to northeast with 100 to 200 ms TWT thickness. Its base reflection is the same as in the Upper Valley. Horizon H3 is detected in the Slide Complex area also.

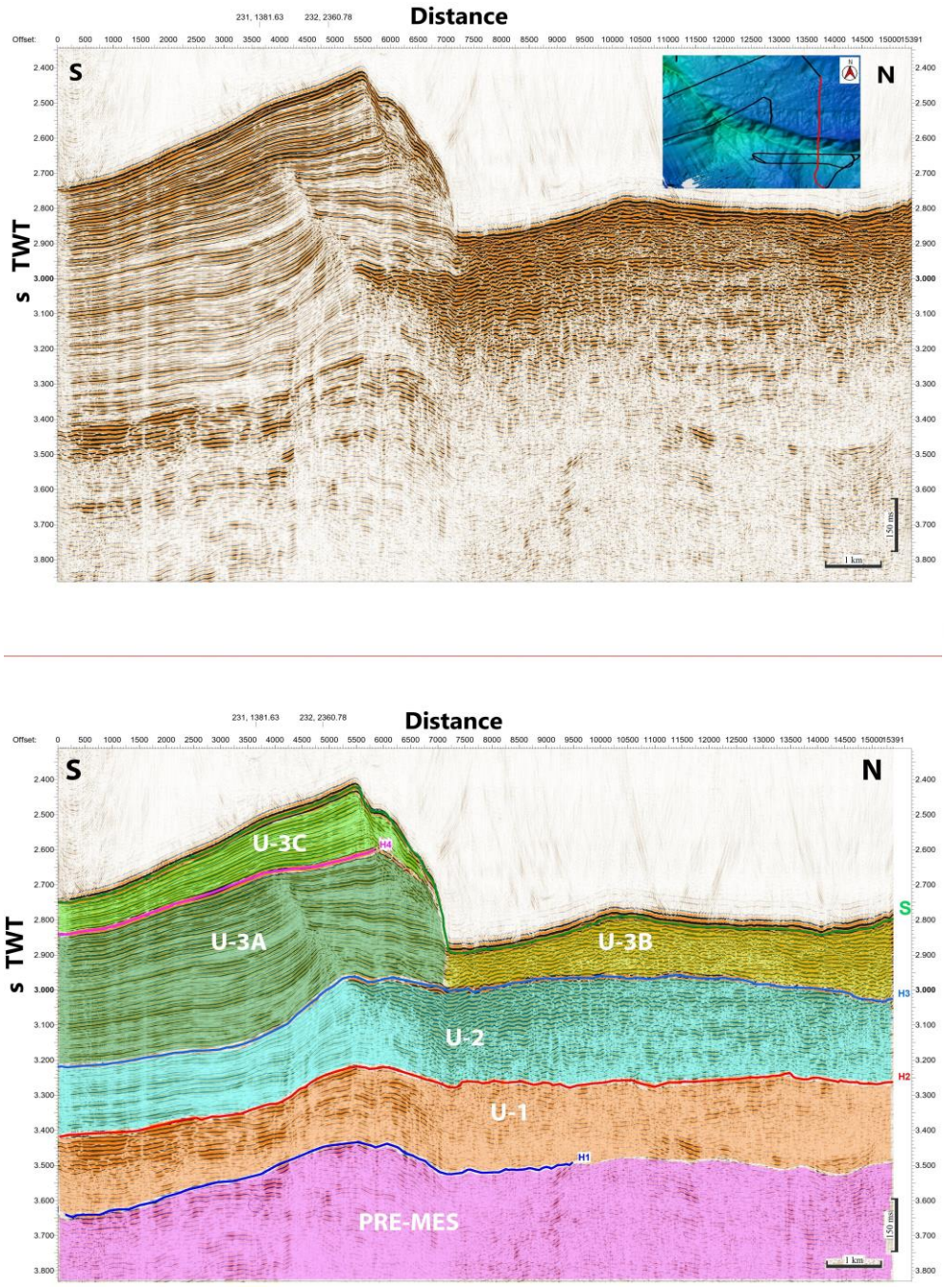

Figure 5.8 Seismic line GeoB07-234 showing the general overview of the units and surfaces

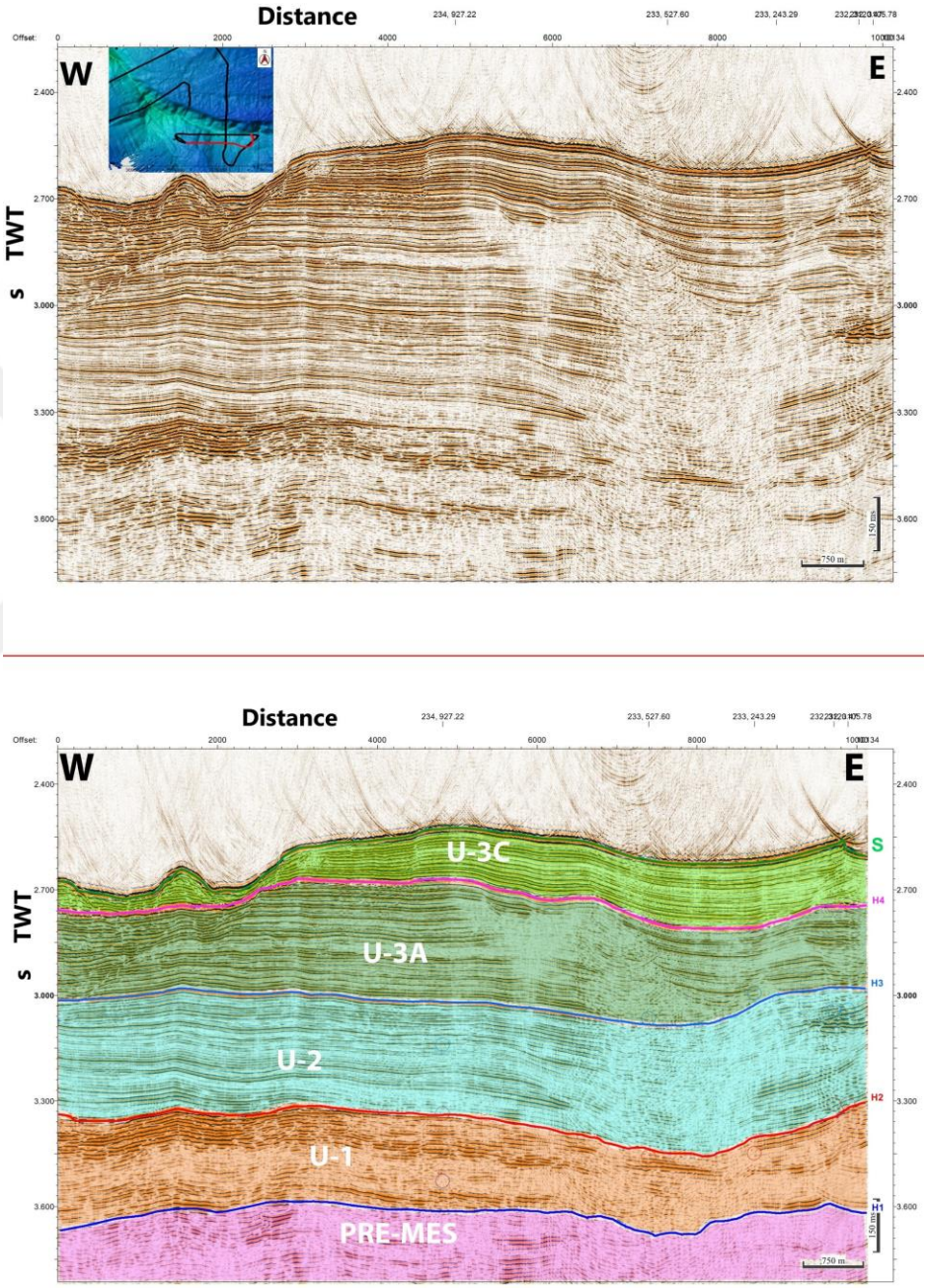

Figure 5.9 Seismic line GeoB07-231 showing the general overview of the units and surfaces

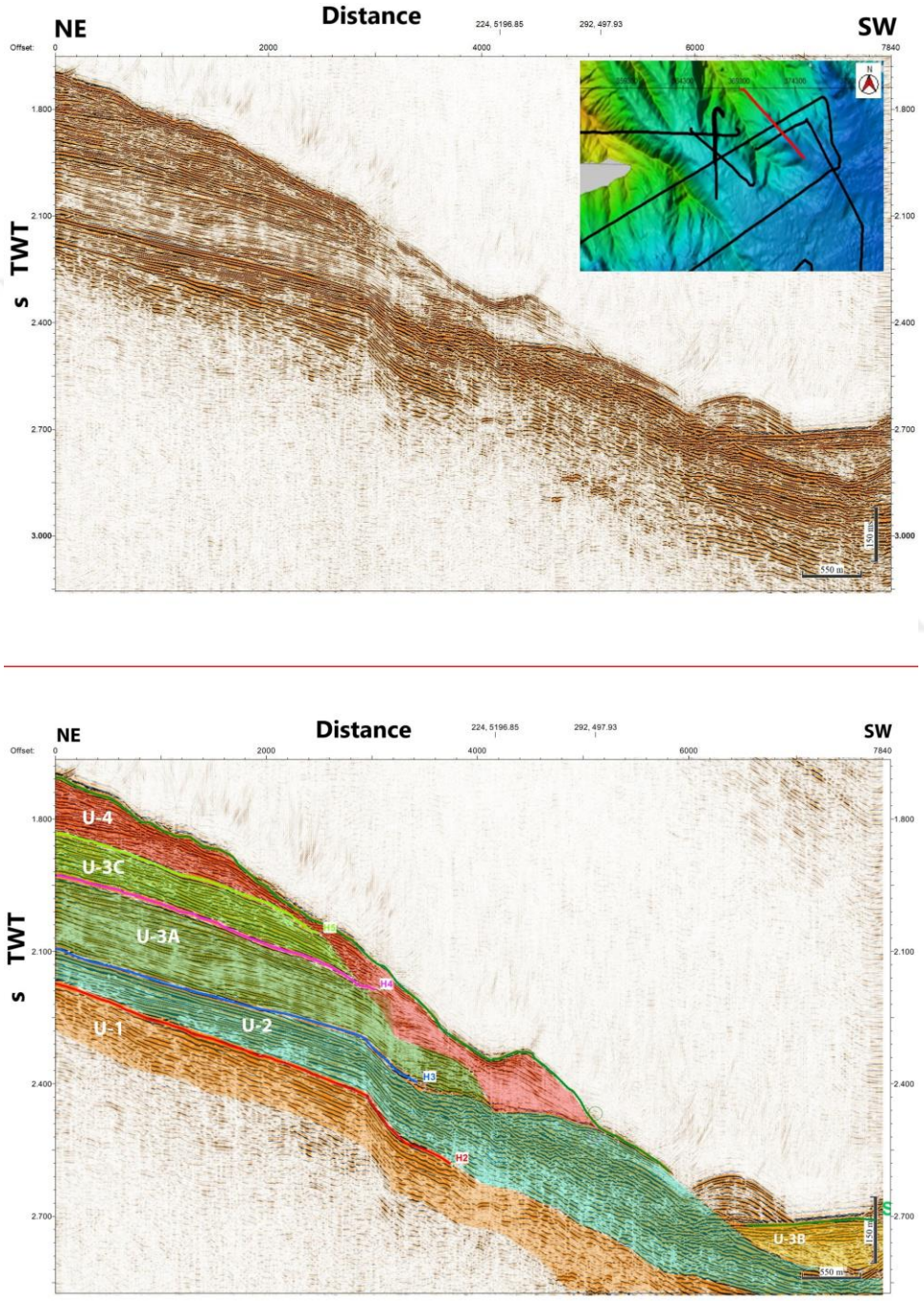

Figure 5.10 Seismic line GeoB07-304 showing the general overview of the units and surfaces

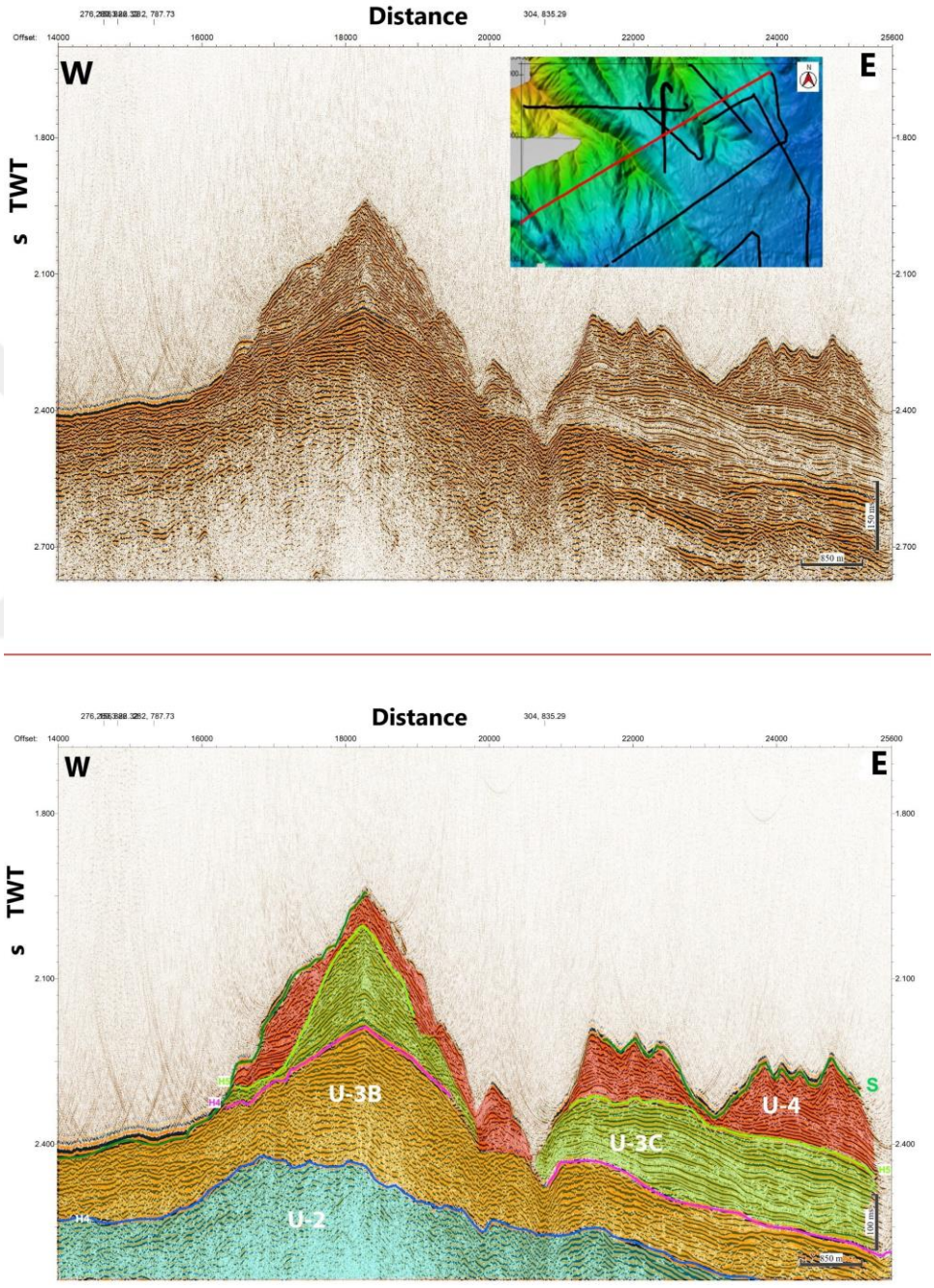

Figure 5.11 Seismic line GeoB07-224 showing the general overview of the units and surfaces

6. DISCUSSION

6.1. Seismic Unit Pre-Mes and Horizon H1

In the Ligurian basin, the sequence of Pliocene-Quaternary sediments that forms the Var fan lies above a moderate reflective horizon - Horizon H1 (named in this study) (Appendix 1), that can be traced throughout the Middle Valley area and corresponds to the top of the upper Messinian evaporates (Savoye et al. 1993).

In previous studies (Malinverno 1981; Sage et al. 2005; J Lofi et al. 2011; Stampfli 1989; García-Castellanos et al. 2009; Bertoni 2006; Bache et al. 2009; J. Lofi et al. 2011; Loget 2006) Horizon H1 is interpreted as the widely described margin erosion surface, which involved all margins in the Mediterranean Sea. Consequently, Seismic Unit Pre-Mes, which is a sediment sequence beneath the Horizon H1, is considered to be Oligo-Miocene deposits, and the overlying units U-1, U-2, U-3, and U-4 represent the Plio-Pleistocene succession (Sage et al. 2005; Lofi et al. 2011; Garcia-Castellanos et al. 2009; Bertoni 2006; Bache et al. 2009; Loget 2006).

But in this study, Horizon H1 has been detected only in the Middle Valley area (Appendix 1), and most of the time, the lowermost part of seismic data is reflection-less (Figure 5.8, 5.9, and 5.10), particularly in the Upper Valley and Slide Complex area. Maybe it becomes smoother towards the lower slope of the basin. So, it was questioned to identify it as a big erosion surface.

Having the less seismic line in the deep water with compare to having a dense seismic grid in shallow water (north area) also affects the study of the southward area.

After the reopening of Gibraltar during the early Pliocene, the Messinian Salinity Crisis stopped, and the Mediterranean basins were rapidly flooded (Loget 2006). The gradual infill of the new accommodation spaces must have occurred in different stages. Several surfaces from the upper units - Horizon H2, H3, H4, H5 inform this.

Above the reflection Horzion H1, the Pliocene-Quaternary column starts to stratify well (Figure 6.1). The lowermost part of the column is more transparent than the upper part (Figure 5.8 and 5.9)(Savoye et al. 1993).

6.2. Seismic Unit U-1

On profile GeoB07-234 (Figure 5.8), Seismic Unit U-1 is subparallel to the present Var Sedimentary Ridge, which is displayed deeper and narrower. It shows a gradual northward migration through time. The marked zone in unit looks like a paleochannel; it follows the stratification and is relatively continuous (Figure 6.1). Generally, there should be erosion or chaos for the paleochannels and should not follow the strata, but it is different here. It might be the fault plane even that is going through the unit. As shown from the image, the lowermost layers are tilted. Probably there is more than just a levee. It could be tectonics involved here, but it needs some proper indications. The reason for the strong amplitude zone can arise from lithology, or it is just a structure. Due to the typical configuration of reflectors within the Seismic Unit U-1, it is interpreted as an area that may be rich with coarse grains or gas trapped here (Figure 5.9 and 6.2). If there is not much clay here, then gas can often be accumulated because there is enough space for bubbles, and they are getting bigger, and big bubbles make high reflection amplitudes.

Paleochannels typically act as pathways for groundwater movement and provide a potential source of groundwater (Subash Chandra et. Al 2019). In previous studies (Savoye et al. 1993, Migeon et al. 2001, Sage et al. 2005), this pattern was identified as paleochannels because the channel-levee system played an enormous role in the paleogeographic evolution of the Var turbidite system (Migeon et al. 2001).

This zone was detected throughout the crest of Var Sedimentary Ridge and in the Middle Valley. It shows a strong reflection and continuous patterns within the Seismic Unit U-1. However, the seismic lines in the Middle Valley area are not dense enough to properly assess the distribution of this seismic pattern.

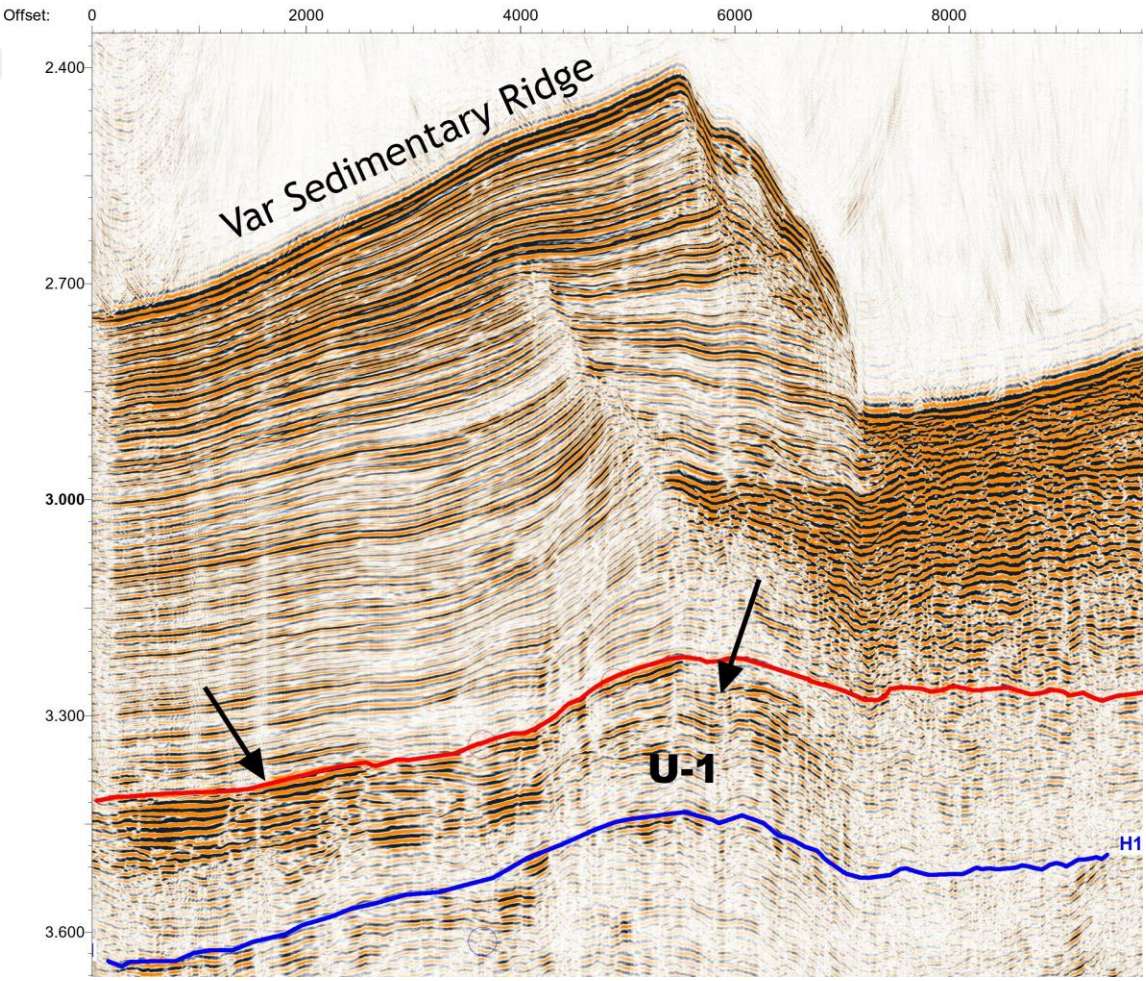

Figure 6.1 Seismic section from GeoB07-234 shows marked zone on Seismic Unit U-1.

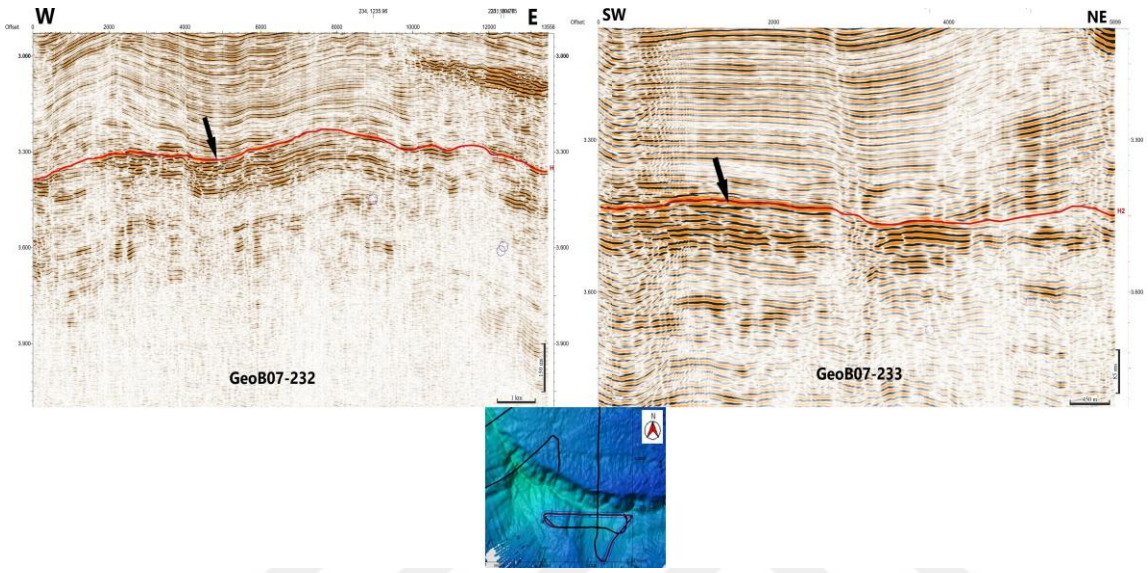

Figure 6.2 Seismic sections from GeoB07-232 and 233 show marked zones on Seismic Unit U-1.

6.2. Sedimentation Patterns on Landslide Complex Area

Line GeoB07-276 which passes “Landslide Complex area” (Förster, A. et al., 2007) displays smooth headwall patterns containing debrites and hemipelagic silty clays with pebbles (Figure 6.3). Tilted layering and numerous headwalls were observed. Here, the material is tent to future landsliding in case of seismic loading or any event destabilizing the sediment (Förster, A. et al., 2007).

On profile GeoB07-304 (Figure 5.10), sliding-induced features and the glide plane are visible because of the high resolution in the seismic data set. Those features were detected on Seismic Unit U-4, which was identified as a mass wasting unit in this study. Several incisions with a rough seafloor above the headwall area were detected from seismic data, which might result from multiple small failure events or older sliding activity.

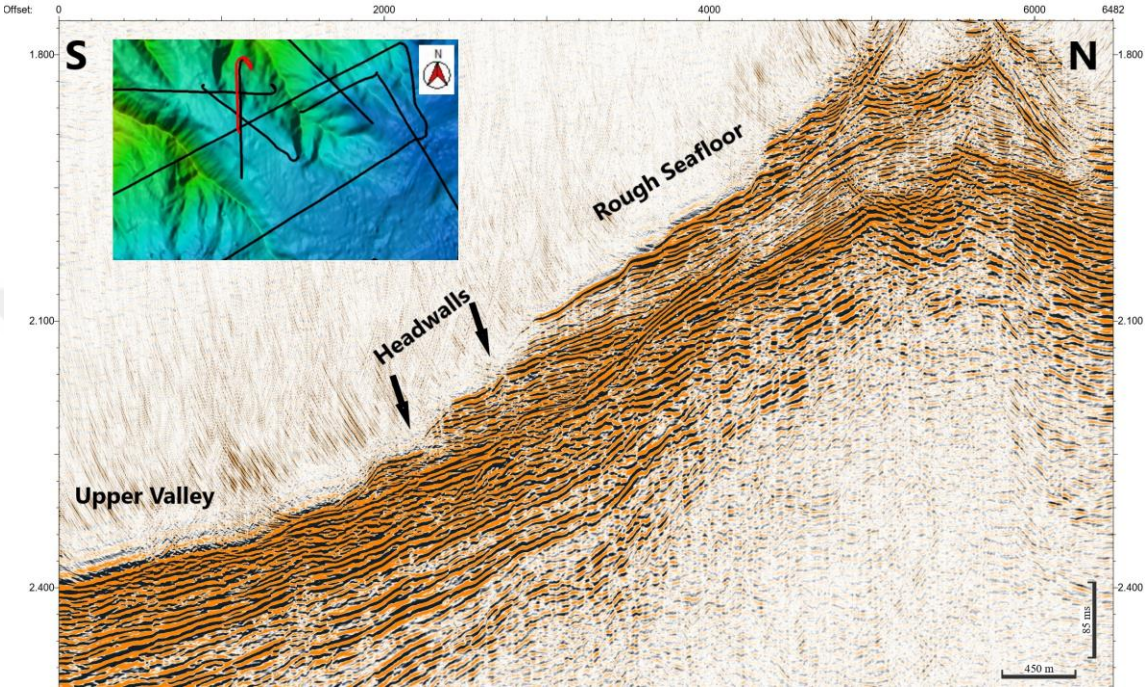

Figure 6.3 Profile GeoB07-276, headwall patterns.

So, the different thicknesses of sediment removal and the sedimentological features could be explained by various time-shifted slide events with the distortion of strata along curved slide surfaces (Förster, A. et al., 2007).

As going towards the south in the seismic profile GeoB07-280 (Figure 6.4) across the landslide, some deposits along the slope appear to have failed but, in the core, no proof has been discovered for debrites (Förster, A. et al., 2007). Instead, very stiff silty-clay sediments covered by hemipelagic sediments were recovered (Kopf et al. 2008). This contradiction may be explained by shallow core data (length: 1.7 m) or stiff silty-clay material - older sediment that has been unroofed when the slide complex formed.

In the map Profile GeoB07-304 (Figure 5.10) is located further away from the Var fan valley.

This zone is not connected to sediment sources from rivers or canyons but is covered by hemipelagic sediments (Klaucke and Cochonat 1999). Therefore, less frequent but more voluminous landslide movement might be general here (Förster, A. et al., 2007).

For Förster et al. (2010) the evolution of the Landslide Complex was happened by sequential multi-phase mass wasting with enhanced failure frequency.

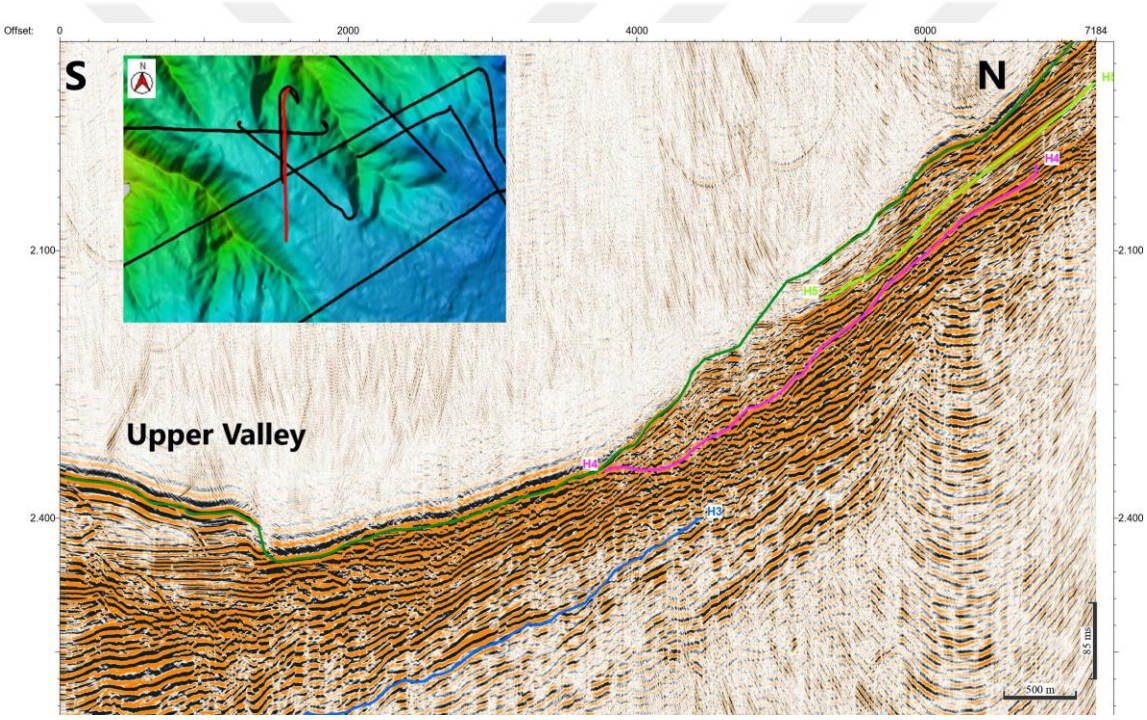

Figure 6.4 Profile GeoB07-280.

On profile GeoB07-235 (located farthest northeast direction of the study area) towards the south, a strange seismic pattern that looks like a block is noticed (Figure 6.5). After checking this zone on the bathymetry map, we will see blocks that are all orientated in the same direction to the west. These blocks relatively have a space between each other, and it is also known that there have been sediment waves (Savoye et al. 1993), so the currents can shape part of the region. It resembles a constructive pattern, which is sitting on top of strong reflection and building up.

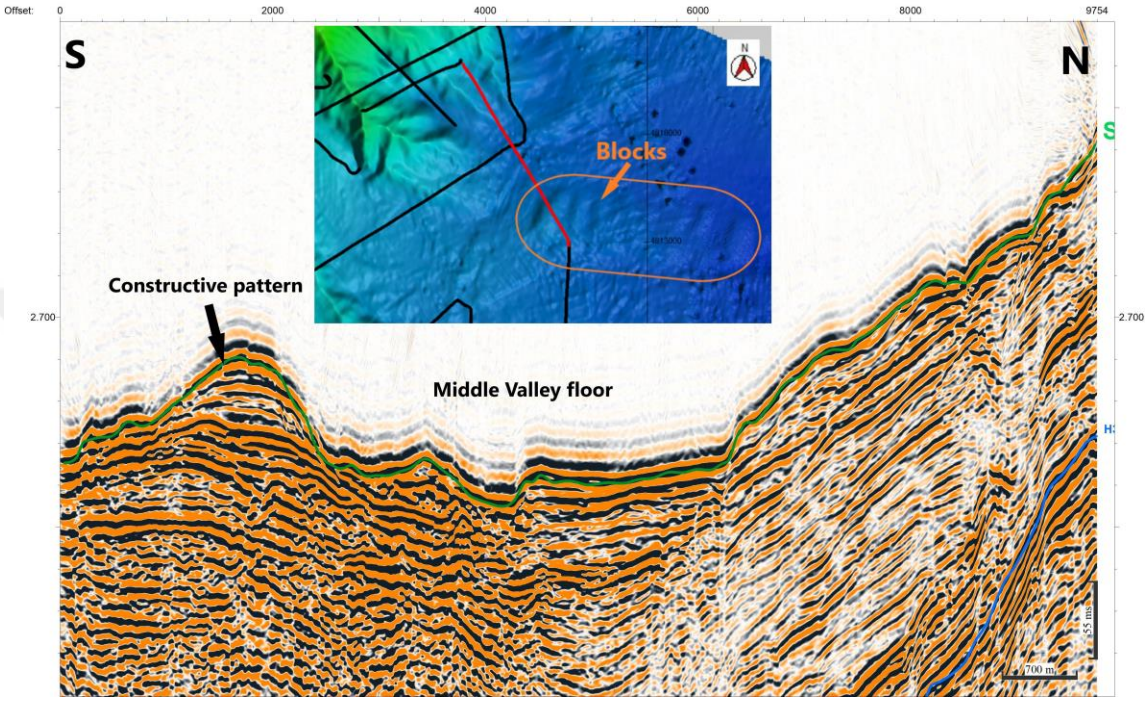

Figure 6.5 Constructive seismic pattern on Profile GeoB07-235.

On profile GeoB07-225 (Figure 6.6), which goes more into of the Middle Valley on direction of north to south, several indications for mass wasting processes, such as the failed deposits was detected. That's why it is difficult to follow the seafloor horizon. Here forced folding also was detected on the Seismic Subunit U-3C, stretching the layers, so maybe the whole margin has some indication for creeping.

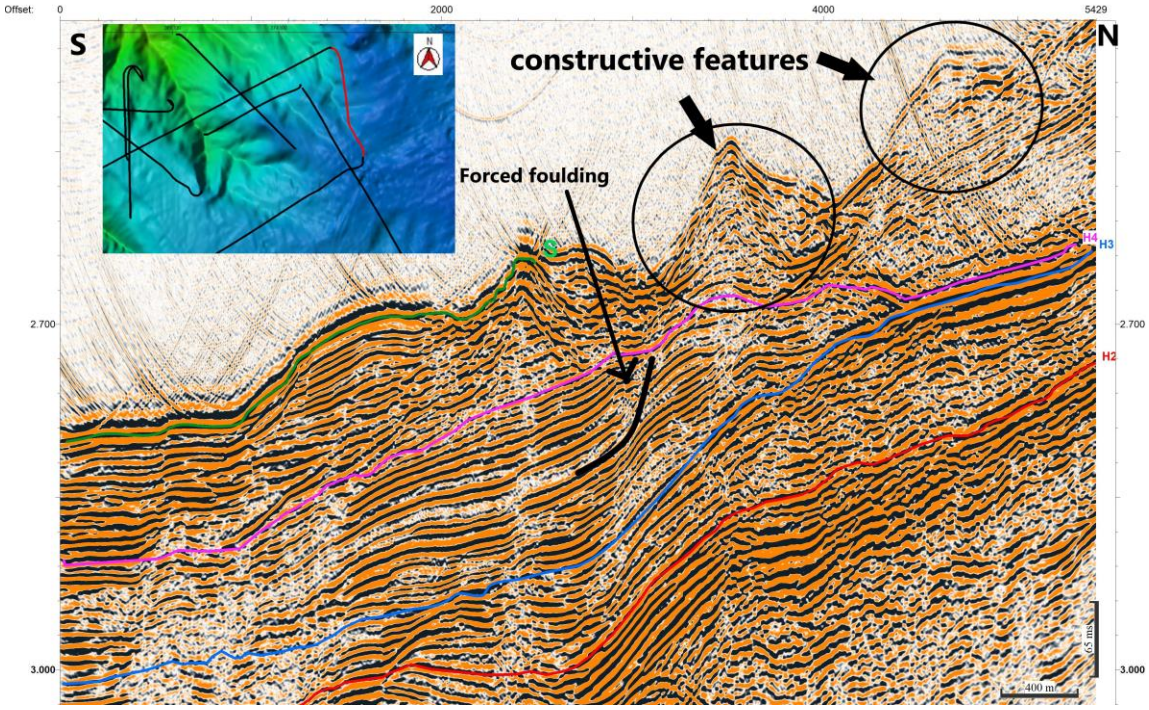

Figure 6.6 Constructive seismic pattern and forced foulding on Profile GeoB07-225

Line GeoB07-224 the longest profile in this expedition (Figure 5.11 and Appendix 2), passes from west to east, enters into the Landslide Complex area too. There are two massive units where the Upper Valley passes among them. This view probably there is an interaction of flows, so that means they are a kind of levee, not a classical one (Figure 5.11). Because here we have a flow from two sides. These are constructive units. They definitely build up, getting steeper and higher over time. The stratification is good internally. There is no real unconformity, no erosion. Between the valleys, the accumulation is going on.

As going towards the east on this profile, a weird seismic pattern has appeared (Figure 5.11). The sedimentary succession is getting more extreme from below to the top, apparently. On Seismic Subunit U-3C, reflections are well stratified, then on top of that, erosion starts (Seismic Unit U-4), and these features gradually go up (Figure 5.11). The

seafloor is truncated a lot. Some of these incisions are the main pathways which feed the big main channel. The bathymetry picture tells the structure looks like an erosive network, a mountain (Figure 5.11). But the seismic reflection data shows it is constructive. But these features may be like more levees, silty to sandy units, which build up.

6.3. Seismic Unit U-3

Figure 5.8 shows amplitude decrease on Seismic Subunit U-3A on profile GeoB07-234. This white zone can be a fault plane which is not easy to image. After looking carefully, apparently, some layers are continuous, and some horizons are almost interrupted. Maybe it is a combination of mass wasting(deformation) and sedimentation happening simultaneously, and stretching makes for loose reflection amplitude, which is caused by subsidence. If sedimentation happens at the same time as when the lower unit is subsiding, we can get a pattern like that and may call it a Growth Fault (Figure 6.7). After flattening the seafloor horizon with the help of a tool from the IHS Kingdom, we will see the relative thickness variation (Figure 6.8). Divergent patterns and sudden angle changes are identified for the layers, which happen when the subsidence is acting (creating accommodation space).

Another example from profile GeoB07-227 (Figure 6.9) part of the blocks are moving out of the plane, and because of that, some reflectors do not match anymore. These fault-like patterns that are so observable could be caused by the creeping of the material, not by vertical movement. So clear that there is a fault plane, but they are not classic tectonics faults; they are faults forming as part of a downslope movement. Due to that, the fault terminates in that area (Figure 6.9).

The growth fault is typical for an environment where sediments are weak, particularly on a margin with a slope angle (Doglioni et al. 1998, Kuecher et al. 2001). The main driving

forces of the growth faults are the deferential sediment load and the low-density layers. Growth faults are located mainly within passive margin sedimentary wedges where tectonic forces have minimum or no effect. Growth faults are connected directly to the subsidence in the coastal and continental shelf areas (Kuecher, G.J; Roberts H. H; Thompson, M. D.; Matthews, I. 2001).

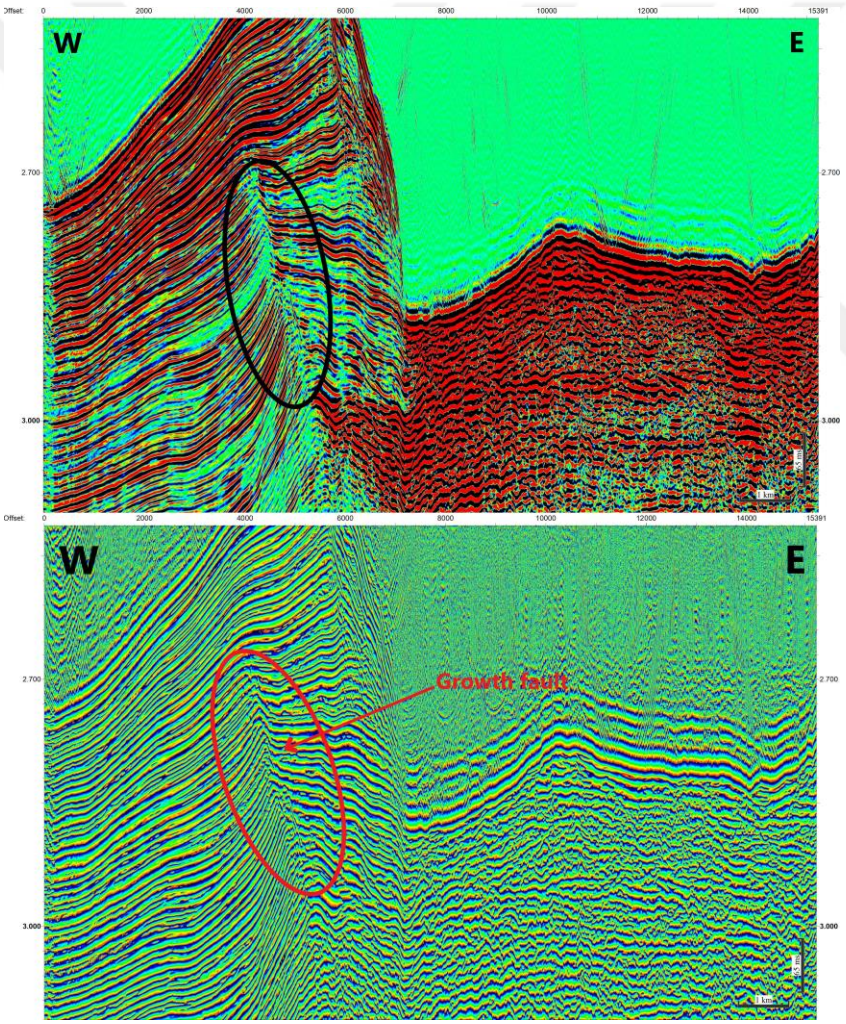

Figure 6.7 Growth Fault on Profile GeoB07-234. Seismic attribute is on Phase view on below picture.

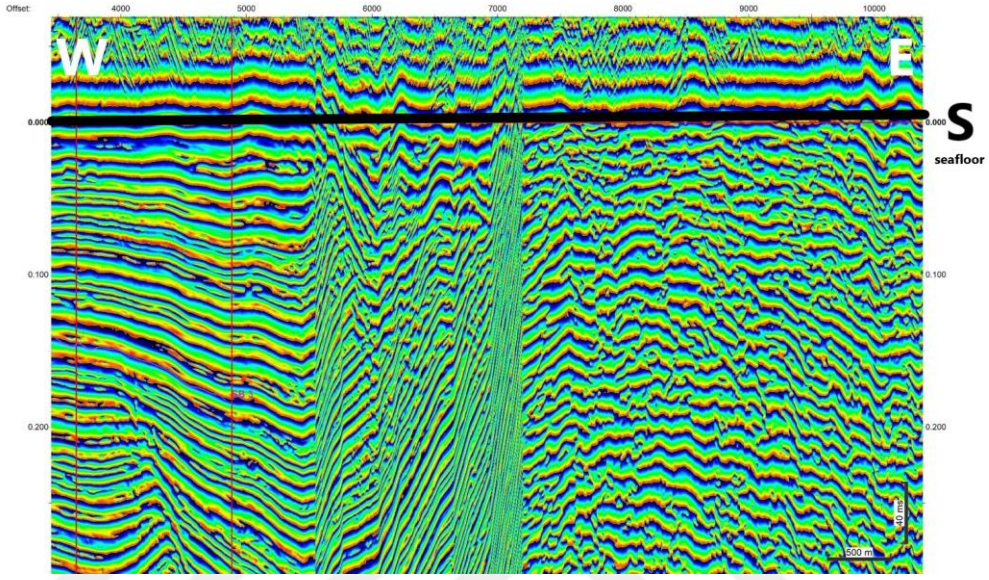

Figure 6.8 After flattening the Seafloor ,the Growth Fault zone on Profile GeoB07-234. Seismic attribute is on Phase view on this picture.

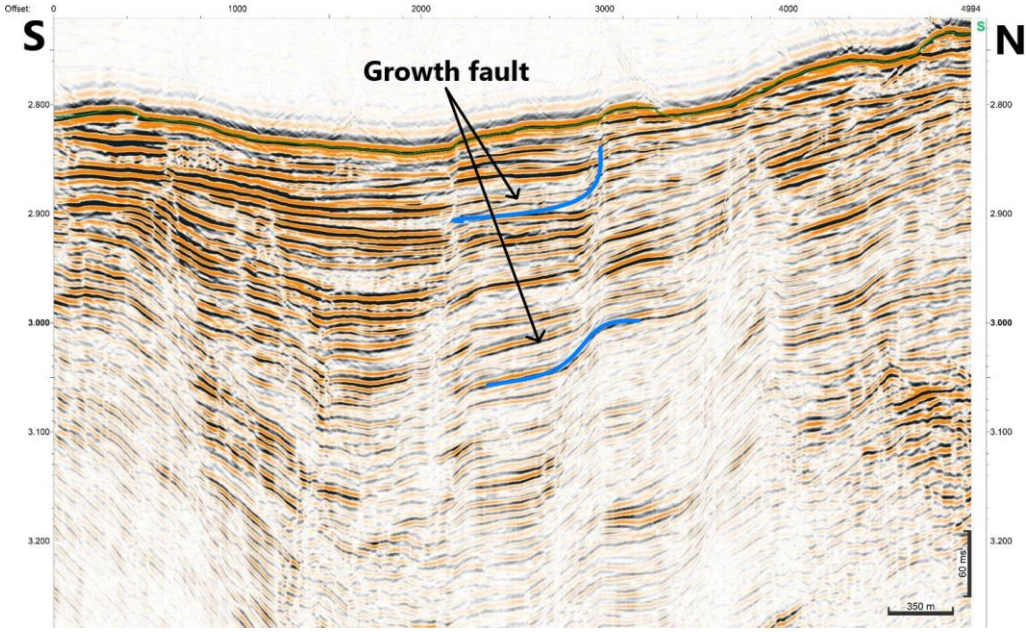

Figure 6.9 The Growth Faults on Profile GeoB07-227.

On profile GeoB07-231 (Figure 5.9), on the Seismic Unit U-3A, depression starts under Horizon H4 in the west direction (Figure 6.10). There is a flat horizon; then the slope changes to a different slope angle. However, some of the reflectors are still continuous. It can be a chaotic movement. Maybe it is the valley flank or plane which develops due to mass-wasting. Because there could be a headwall and some tilted strata, and then a little bit of chaos coming (Figure 6.10). The material that left the headwall is lying in there. This black dotted line could be a part of the fold system or may call it forced folds. The forced folds may impact seismic reflection amplitudes in different ways. It is basically an interruption of the reflection or the weakening of reflection amplitude (Zühlsdorff, V. Spiess 2006). The overall shape and trend of forced folds will be dominated by the shape of the forcing basement peak, the folding is the result of fault movement within the cover sediments (Suppe, 1983). There is also a kink because of minor slope failure. It can interpret as an element of the mass-wasting process (Figure 6.10).

Some sort of chaos, smiles, and side echoes are visible as going in the east direction on Seismic Subunit U-3C and U-3A, which can indicate the erosion of transport (Figure 5.9 and Figure 6.10).

In Migeon et al. 2011 this zone was mentioned as synsedimentary faults located below the VSR. The superficial faults gradually converge at depth, are located above some larger-scale faults that affect the paleochannels, and are rooted on top of the Messinian evaporites. In this thesis, this seismic pattern was seen almost in all seismic lines: Profile GeoB07-231, 232, 233, 234 parallel to the crest of the Var Sedimentary Ridge towards the west (Figure 5.8, 5.9, 6.10, Appendix x, x).

On further north seismic lines, along the Var sedimentary ridge, low to medium sediment waves appear on Seismic Subunit U-3C, in the east direction on the profile GeoB07-233 (Figure 6.11). The ridges probably consist of poorly disturbing material as coherent and continuous reflections are still observed. Although the coverage with seismic lines of the

area is insufficient to assess the behavior and nature of these patterns, they seem to be a common feature along the ridge. For instance, in the Var sedimentary ridge, large-scale sediment waves developed (Savoye et al. 1993). For Migeon et al. (2006) and Savoye et al. (1993), this feature's formation mechanism has a connection with gravity flows over-spilling from the valley. Urgeles et al. (2011) show that these undulated features could originate from hyperpycnal flows, bottom currents internal waves, or longshore currents. Hyperpycnal flows are known to form these features (Förster 2011).

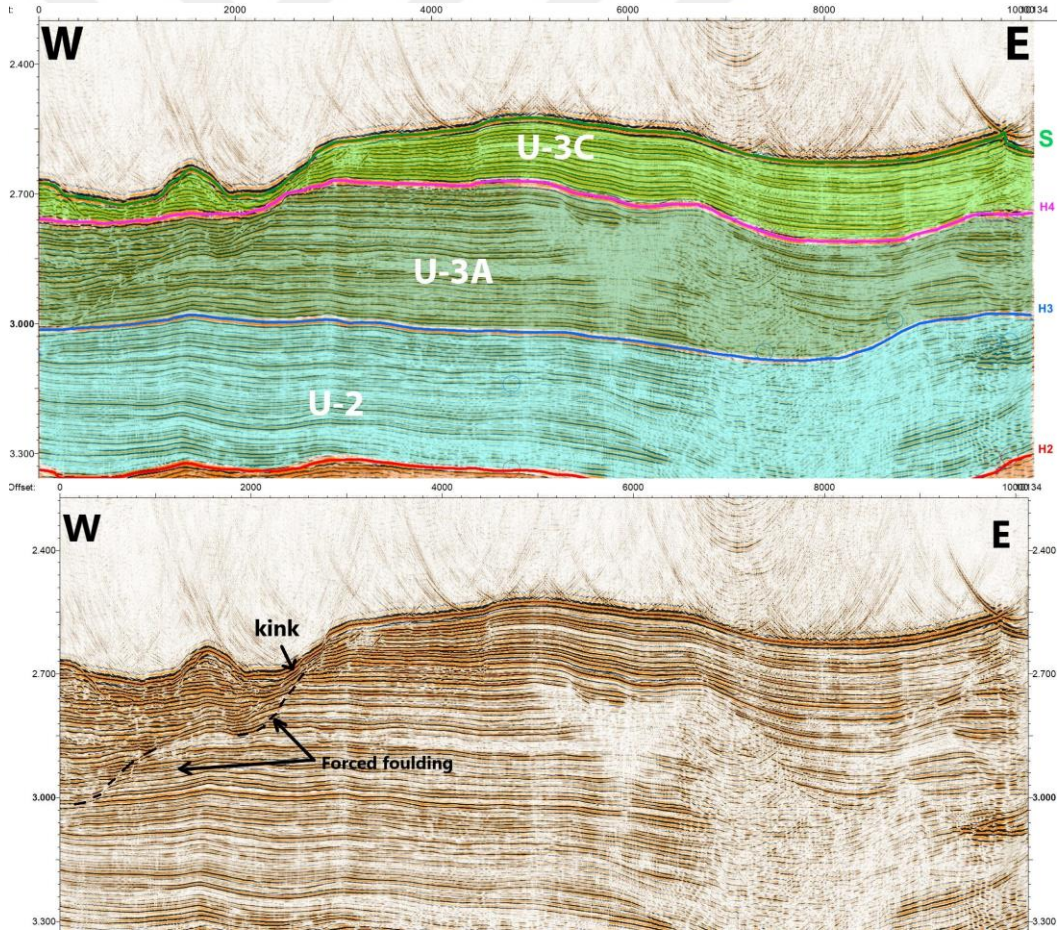

Figure 6.10 Forced foulding on Profile GeoB07-231.

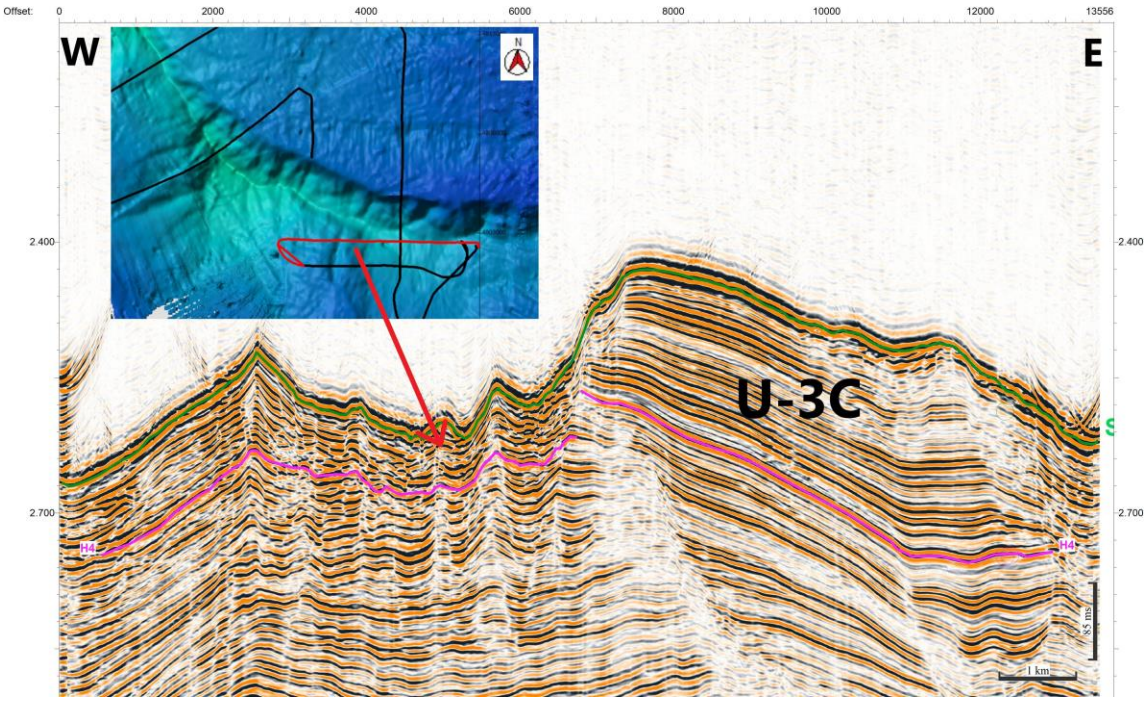

Figure 6.11 Wavy structure on Seismic Unit U-3C on Profile GeoB07-232.

Some sort of chaos, smiles, and side echoes are visible as going in the east direction on Seismic Subunit U-3C and U-3A, which can indicate the erosion of transport (Figure 5.9 and Figure 6.10).

In Migeon et al. 2011 this zone was mentioned as synsedimentary faults located below the VSR. The superficial faults gradually converge at depth, are located above some larger-scale faults that affect the paleochannels, and are rooted on top of the Messinian evaporites. In this thesis, this seismic pattern was seen almost in all seismic lines: Profile GeoB07-231, 232, 233, 234 parallel to the crest of the Var Sedimentary Ridge towards the west (Figure 5.8, 5.9, 6.10, Appendix x, x).

On profile GeoB07-231 (Figure 5.9), on the Seismic Unit U-3A, depression starts under Horizon H4 in the west direction (Figure 6.10). There is a flat horizon; then the slope

changes to a different slope angle. However, some of the reflectors are still continuous. It can be a chaotic movement. Maybe it is the valley flank or plane which develops due to mass-wasting. Because there could be a headwall and some tilted strata, and then a little bit of chaos coming (Figure 6.10). The material that left the headwall is lying in there. This black dotted line could be a part of the fold system or may call it forced folds. The forced folds may impact seismic reflection amplitudes in different ways. It is basically an interruption of the reflection or the weakening of reflection amplitude (Zühlsdorff, V. Spiess 2006). The overall shape and trend of forced folds will be dominated by the shape of the forcing basement peak, the folding is the result of fault movement within the cover sediments (Suppe, 1983). There is also a kink because of minor slope failure. It can interpret as an element of the mass-wasting process (Figure 6.10).

7. CONCLUSION

The first objective of this thesis was to perform the seismic processing steps to the deepwater 2D multichannel seismic dataset from offshore Ligurian Margin accurately. The processing content is based on enhancing the signal-to-noise ratio to get an interpretable seismic data set. Since the dataset was acquired in a geologically complicated area shaped by canyons and steep-sided gully systems, the seismic data has several processing challenges regarding velocity analysis and migration. A carefully completed geometry calculation and the following binning process obtained a high fold of coverage. A high horizontal and vertical resolution was achieved by using small bin sizes. Although to have a rough bathymetry and complex geology, a velocity analysis that is critical for subsequent processing steps could be performed correctly.

Due to some preparatory work, which includes software learning, the processing took a long time to finish. In brief, through a tailored and dedicated seismic processing flow, it was possible to improve the data quality significantly.

Ligurian Margin is a relatively special region (North-western Mediterranean) which means it is not easy to explain some processes. That is why this thesis is under the name of inventory of mass wasting, which represents the documentation of mass wasting patterns and sediment features no matter the exact geological origin. This thesis has a part of an attempt to understand the connection between the deposits and deeper areas and the original deposits where the failure masses were coming from. So the second objective of this study was to gain an insight into the lower slope of the Ligurian Margin area, characterized by its active tectonics and frequent mass wasting. In order to enable the interpretation and investigation of mass wasting, a dataset consisting of 17 multichannel seismic lines was used. These lines cover the Landslide Complex, VSR, and the Upper and Middle Valley. The study area shows a complex inner structure influenced by multiple features.

Significant mass wasting events influence the Landslide Complex area in the north. Also, seismicity, sediment input, and background sedimentation are controlling factors of the landslide's topography.

Seismic facies description has been done correctly, and seismic units were identified in the study area. Next to that, certain depositional and transport processes are discussed.

Accurate age dating of the timing of slope failure is always an extremely challenging task (Vizcaino et al., 2006; Gracia et al., 2010; Urlaub et al., 2013;). In a recent investigation based on 68 large and well-studied landslides worldwide, Urlaub et al. (2013) noted that age uncertainties are significant for a large part of the databases, and dating is usually of poor quality. Various uncertainties still exist about the exact age dating of the landslide event, which is generally because of samples' availability and the method used.

So, Regarding giving the geologic age to the identified seismic units and sea-level changes, it could not be studied in this thesis because there are a few reasons. On the one hand, the shelf is extremely narrow. There is no prograding sequence on the shelf to demonstrate some changes over time (Savoye et al. 1993). Being in the Mediterranean water is different from being in the open ocean. Another reason is that the margin is extremely steep, the slope angle is very high, and the region is famous for several earthquakes. Over time, a high amount of sediment transport decoupled with sea level, triggered by mass wasting. Beyond that, it is not possible with the data that we have to put ages on seismic units. That is why this thesis is more about descriptional things, understanding the processes, and describing sediment distribution. In brief, seismic patterns that are detected in this study not can be easily connected to the sea-level changes rather, they could be more chaotic.

About having an erosive feature or not of the Horizons that bound the seismic units in this thesis is not easy to discuss, at least in classical content. For example, between Seismic Unit U-3C and Seismic Unit U-3A (Figure 5.9 and 6.10), there is a deformation of

sediments which is not a fault but is a disruption, and it is stretching. Consequently, most of these boundaries between undeformed and deformed sediments are similar. The reason for sediment deformation can be creep. On the steep slope, the sediment is loading with a heavy and strong force, and it is not reacting in a brittle way because the material is soft and unconsolidated (Förster, A., 2011). Sediments are just stretched, moving downslope but not too much, which keeps the structure.

REFERENCES

Al-Chalabi, M. (1973): Series approximations in velocity and traveltime computations Geophys. Prospect. 21, pp. 783-795.

Anthony, E., 2007. Problems of hazard perception on the steep, urbanised Var coastal floodplain and delta, French Riviera. Méditerranée, 108.

Anthony, E. & Julian, M., 1997. The 1979 Var Delta landslide on the French Riviera: a retrospective analysis. Journal of coastal research, 13(1), pp.27–35.

Bache, F., Olivet, J. & Gorini, C., 2009. Messinian erosional and salinity crises: view from the Provence Basin (Gulf of Lions, Western Mediterranean).

Bertoni, C. & Cartwright, J., 2006. Controls on the basinwide architecture of late Miocene (Messinian) evaporites on the Levant margin (Eastern Mediterranean).

Calder, B., 2003. Automatic statistical processing of multibeam echosounder data. International Hydrographic Review.

Calder, B., 2013. Center for Coastal & Ocean Mapping NOAA-UNH Joint Hydrographic Center.

Cassidy, M.., Uzielli, M. & Lacasse, S., 2008. Probability risk assessment of landslides: A case study at Finneidfjord. Canadian Geotechnical Journal, 45(9), pp.1250–1267.

CIESM, 2011. Marine geo-hazards in the Mediterranean F. Briand, ed. CIESM Workshop Monographs, 42(February), p.192.

Daniel Arraiz – 2013 - Geologic Evolution of the Nice Slope, France. Ligurian Margin – Western Mediterranean Sea (M.Sc. thesis)

Dondurur, D. (2018): Acquisition and Processing of Marine Seismic Data. Elsevier Inc. Amsterdam.

K.K.Eriş et al., 2007. The timing and evolution of the post-glacial transgression across the Sea of Marmara shelf south of İstanbul.

Förster, A., 2011. Geotechnical measurements to characterise slope sediments and to identify landslide mechanisms and their impact on ecosystems. University of Bremen.

Förster, A. et al., 2007. Mass wasting dynamics at the deeper slope of the Ligurian Margin. , 2007(July).

Förster, A. et al., 2010. Mass Wasting Dynamics at the Deeper Slope of the Ligurian Margin (Southern France). In D. Mosher et al., eds. Submarine Mass Movements and Their Consequences SE - 6. Springer Netherlands, pp. 67–77.

García-Castellanos, D. et al., 2009. Catastrophic flood of the Mediterranean after the Messinian salinity crisis. Nature, 462(7274), pp.778–81.

Harris, P.. & Whiteway, T., 2011. Global distribution of large submarine canyons: Geomorphic differences between active and passive continental margins. Marine Geology, 285(1-4), pp.69–86.

Klaucke, I., Savoye, B. & Cochonat, P., 2000. Patterns and processes of sediment dispersal on the continental slope off Nice, SE France. Marine Geology, 162(2-4), pp.405–422.

Kopf, A. et al., 2008. Report and Preliminary Results of Meteor Cruise M73/1: LIMA-LAMO (Ligurian Margin Landslide Measurements & Observatory), Cadiz, 22.07.2007 - Genoa, 11.08.2007, Bremen.

Larroque, C. et al., 2001. Active and recent deformation at the Southern Alps – Ligurian basin junction. Netherlands Journal of Geosciences / Geologie en Mijnbouw, 80, pp.255–272.

Larroque, C., Lépinay, B. & Migeon, S., 2010. Morphotectonic and fault–earthquake relationships along the northern Ligurian margin (western Mediterranean) based on high resolution, multibeam bathymetry and multichannel seismic-reflection profiles. Marine Geophysical Research, 32(1-2), pp.163–179.

Lofi, J et al., 2011. Atlas of the Messinian seismic markers in the Mediterranean and Black Seas, Paris: Mém. Soc. géol.. fr., n.s., 179 and World Geological Map Commission.

Lofi, J. et al., 2005. Erosional processes and paleo-environmental changes in the Western Gulf of Lions (SW France) during the Messinian Salinity Crisis. Marine Geology, 217(August), pp.20–24.

Lofi, J. et al., 2011. Refining our knowledge of the Messinian salinity crisis records in the offshore domain through multi-site seismic analysis. Bulletin de la Societe Geologique de France, 182(2), pp.163–180.

Masson, D.. et al., 2006. Submarine landslides: processes, triggers and hazard prediction. Philosophical transactions. Series A, Mathematical, physical, and engineering sciences, 78 364(1845), pp.2009–39.

Michael Schwartz – 2016 - Seismo-acoustic investigation of mass wasting at the Makran accretionary prism offshore Pakistan (M.Sc. thesis)

Migeon, S. et al., 2006. The Var turbidite system (Ligurian Sea, northwestern Mediterranean) —morphology, sediment supply, construction of turbidite levee and sediment waves: implications for hydrocarbon reservoirs. Geo-Marine Letters, 26(6), pp.361–371.

Migeon, S., Cattaneo, A. & Hassoun, V., 2011. Morphology, distribution and origin of recent submarine landslides of the Ligurian Margin (North-western Mediterranean): some insights into geohazard assessment. Marine Geophysical …, 32(March), pp.225–243.

Mosher, D.. et al., 2010. Submarine Mass Movements and Their Consequences D. Mosher et al., eds. Advances in Natural and Technological Hazards Research, 28, pp.1–8.

Mulder, T. et al., 1998. The Var Submarine System: understanding Holocene sediment delivery processes and their importance to the geological record. In M. . Stoker, D. Evans, & A. Cramp, eds. Geological Processes on Continental Margins: Sedimentation, Mass Wasting and Stability. London: Spec. Publ. Geol. Soc, pp. 145–166.

Mulder, T., Savoye, B. & Syvitski, J.P.., 1997. Numerical modelling of a mid-sized gravity flow: the 1979 Nice turbidity current (dynamics, processes, sediment budget and seafloor impact). Sedimentology, pp.305–326.

Normark, W.., Moore, J.. & Torresan, M.., 1993. Giant volcano-related landslides and the development of the Hawaiian Islands. In pp. 184–196.

Rashpal SINGH – 2019 – Processing and Interpretation of 3D High-Resolution Multichannel Seismic Data from Offshore Nice, Southern France (M.Sc. thesis)

Sage, F. et al., 2005. Seismic evidence for Messinian detrital deposits at the western Sardinia margin, northwestern Mediterranean. Marine and Petroleum Geology, 22(6-7), pp.757–773.

Savoye, B., Piper, D.J.. & Droz, L., 1993. Plio-Pleistocene evolution of the Var deep-sea fan off the French Riviera. Marine and Petroleum Geology, 10.

Sultan, N. et al., 2007. PRISME CRUISE : REPORT AND PRELIMINARY RESULTS REF : IFR CB/GM/LES/08-11 R/V ATALANTE Toulon, 7/10/2007 – Toulon, 7/11/2007, Plouzané.

Suppe, J. (1983). Geometry and kinematics of fault-bend folding,Am.J. Sci.,283, 684–721.

Ting-Wei WU – 2016 - Seismic Processing and Interpretation of the Shallow Ligurian Margin off Nice, for the Landslide Modeling Prospect Combination of geotechnical and 2D seismic lines in the Nice Airport slide area (M.Sc. thesis)

Urgeles, R. et al., 2011. A review of undulated sediment features on Mediterranean prodeltas: distinguishing sediment transport structures from sediment deformation. Marine Geophysical Research, 32(1-2), pp.49–69.

Yilmaz, O. (2000): Seismic Data Analysis: Processing, Inversion, and Interpretation of Seismic Data. Investigations in Geophysics, Band 10. Volume 2. Society of Exploration Geophysicists. Tulsa, Oklahoma.

Zliou, H. (2014). In Practical Seismic Data Analysis (pp. 172-203). Cambridge: Cambridge University Press.

Zühlsdorff, V. Spiess 2006. Sedimentation patterns, folding, and fluid upflow above a buried basement ridge: Results from 2-D and 3-D seismic surveys at the eastern Juan de Fuca Ridge flank.

APPENDICES

Appendix 1: Depth map of Horizon H1.

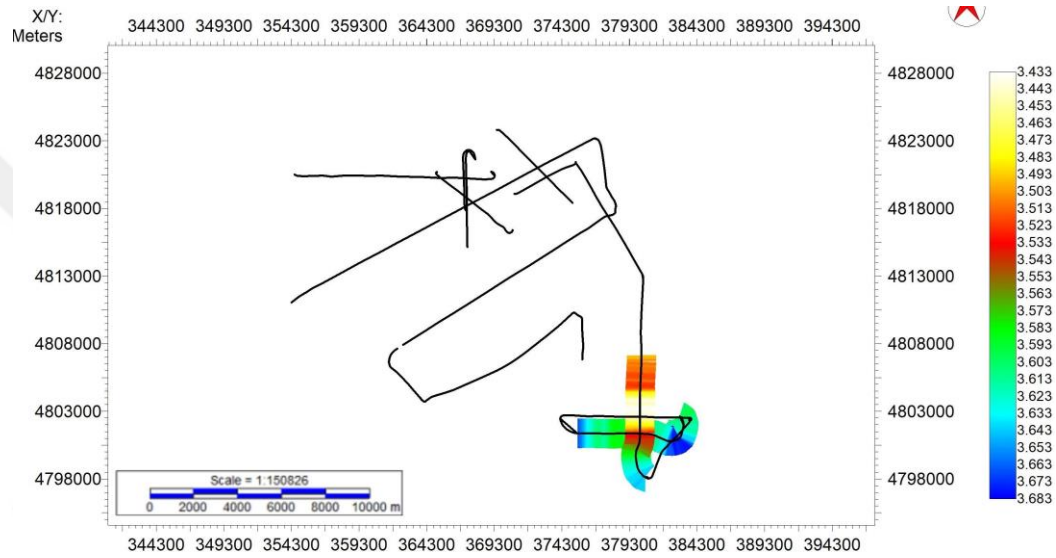

Appendix 2: Seismic section of Line M73-1-GeoB07-224.

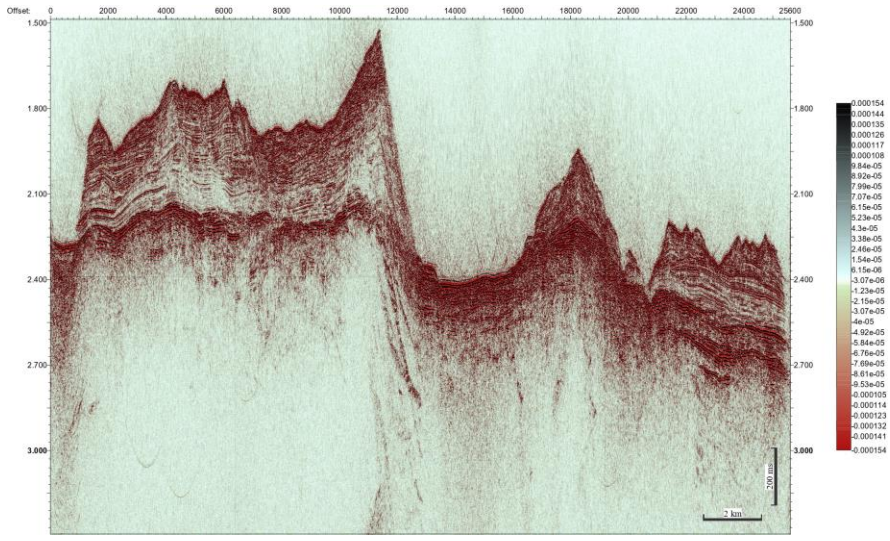

Appendix 3: Seismic section of Line M73-1-GeoB07-225.

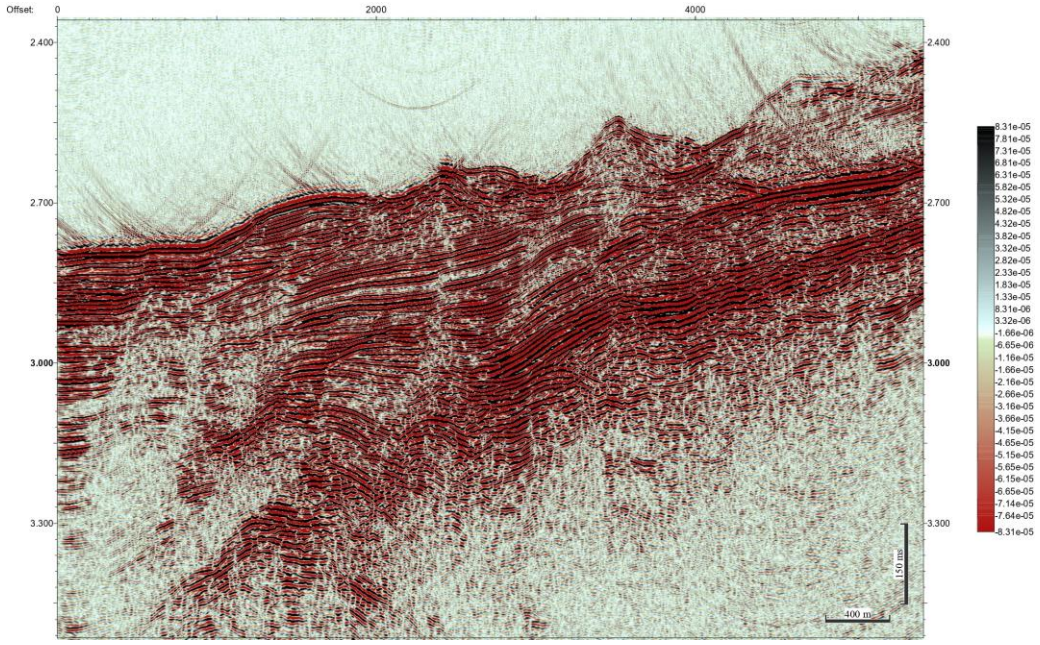

Appendix 4: Seismic section of Line M73-1-GeoB07-226

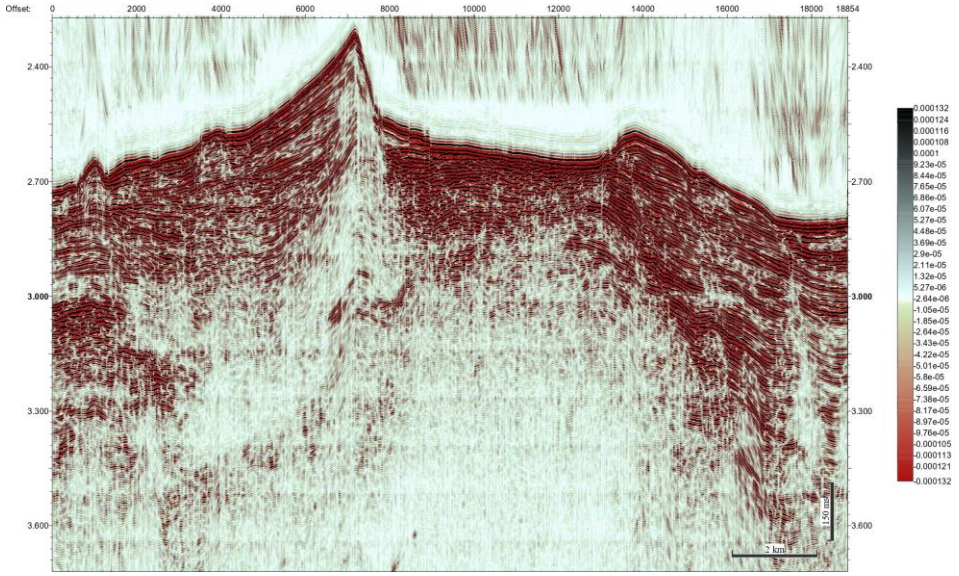

Appendix 5: Seismic section of Line M73-1-GeoB07-227

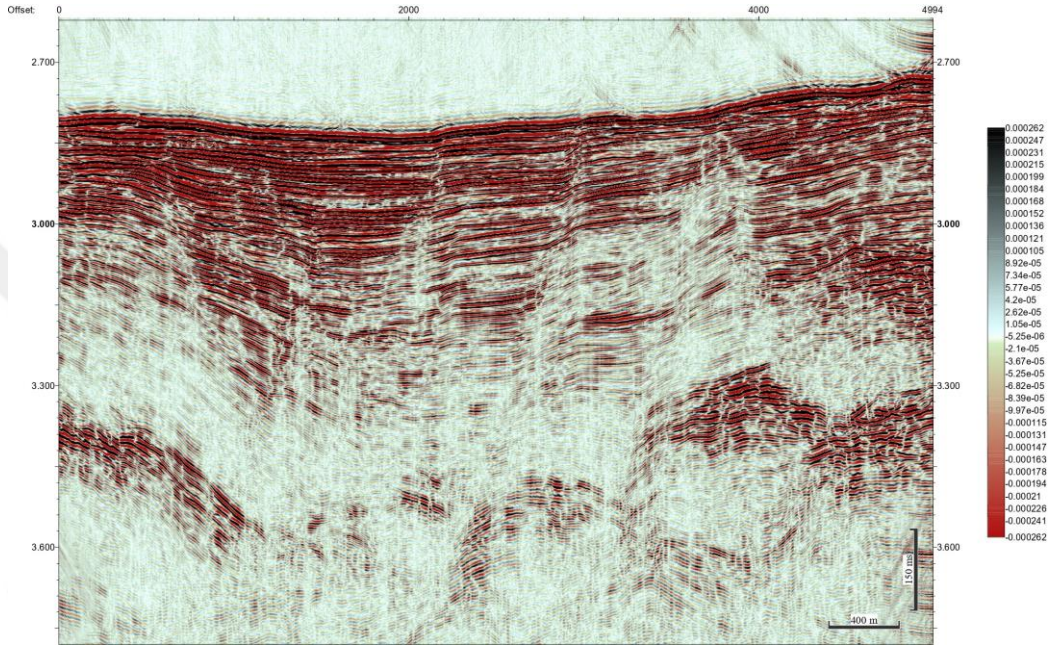

Appendix 6: Seismic section of Line M73-1-GeoB07-228

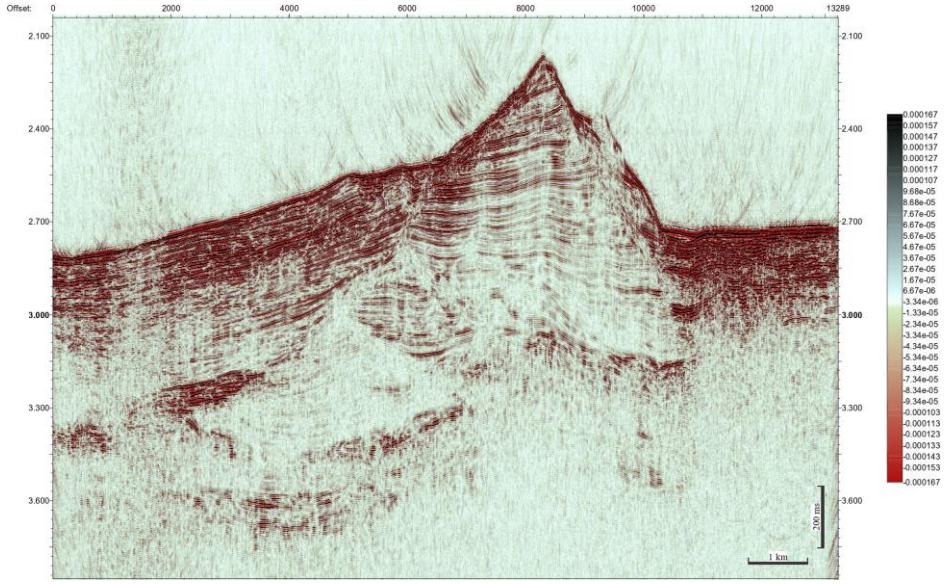

Appendix 7: Seismic section of Line M73-1-GeoB07-229

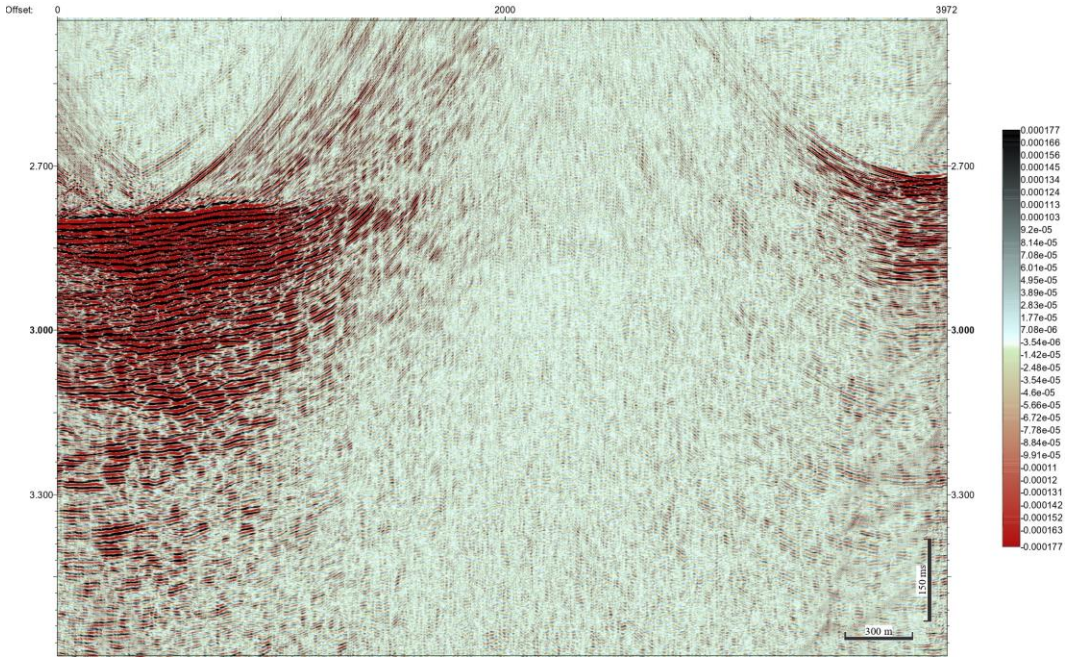

Appendix 8: Seismic section of Line M73-1-GeoB07-231

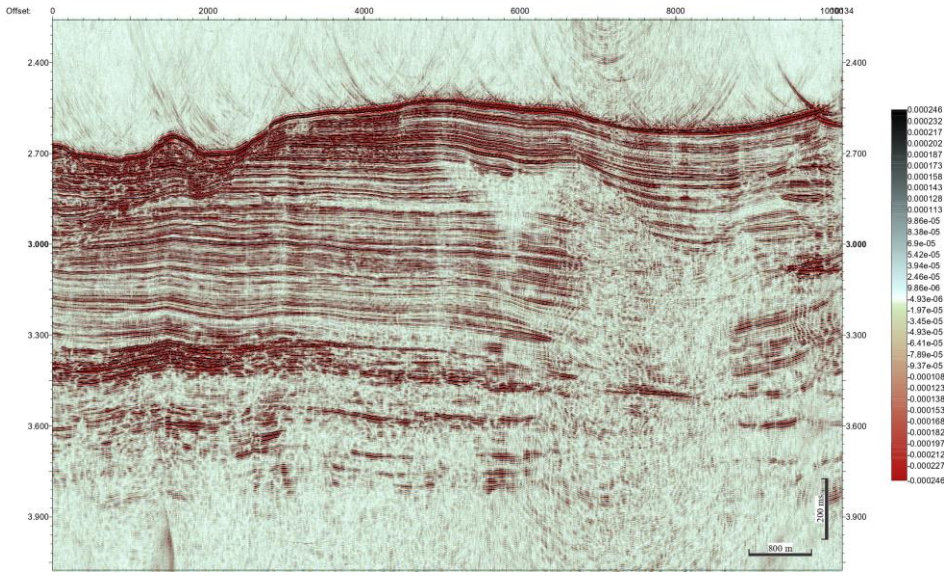

Appendix 9: Seismic section of Line M73-1-GeoB07-232

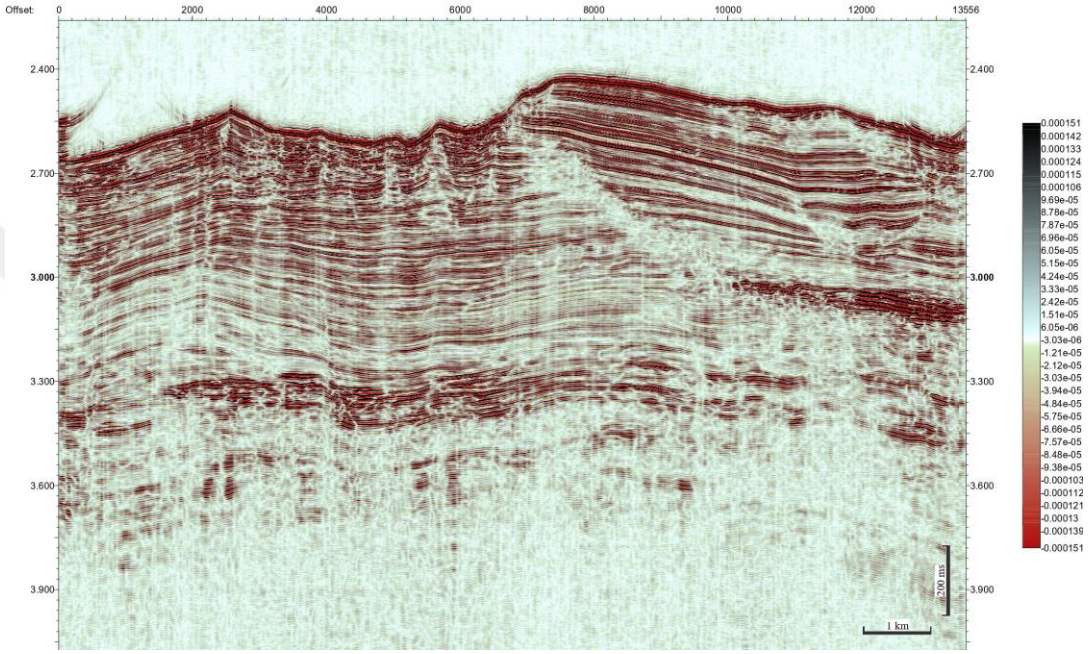

Appendix 10: Seismic section of Line M73-1-GeoB07-233

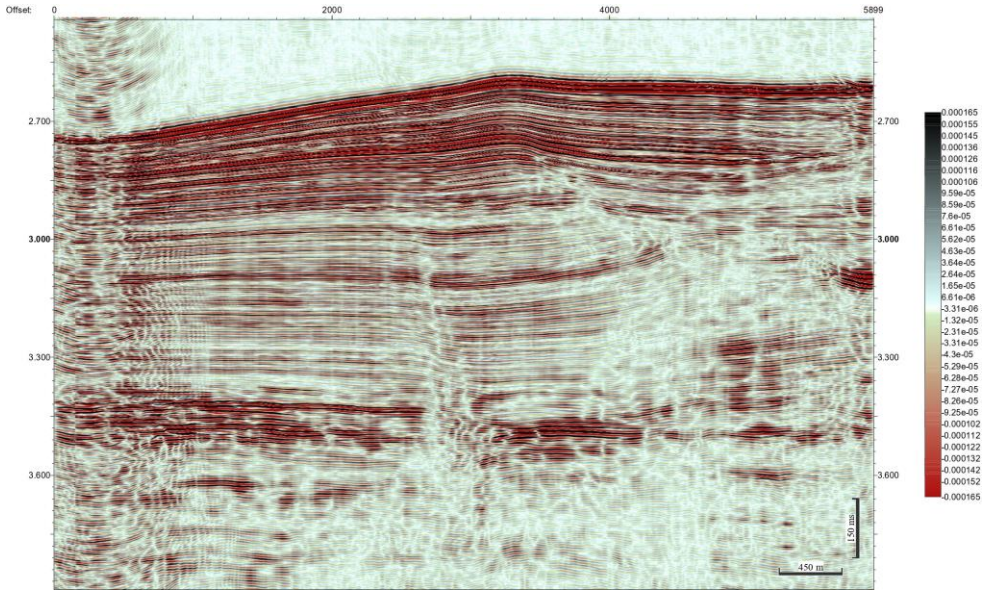

Appendix 11: Seismic section of Line M73-1-GeoB07-234

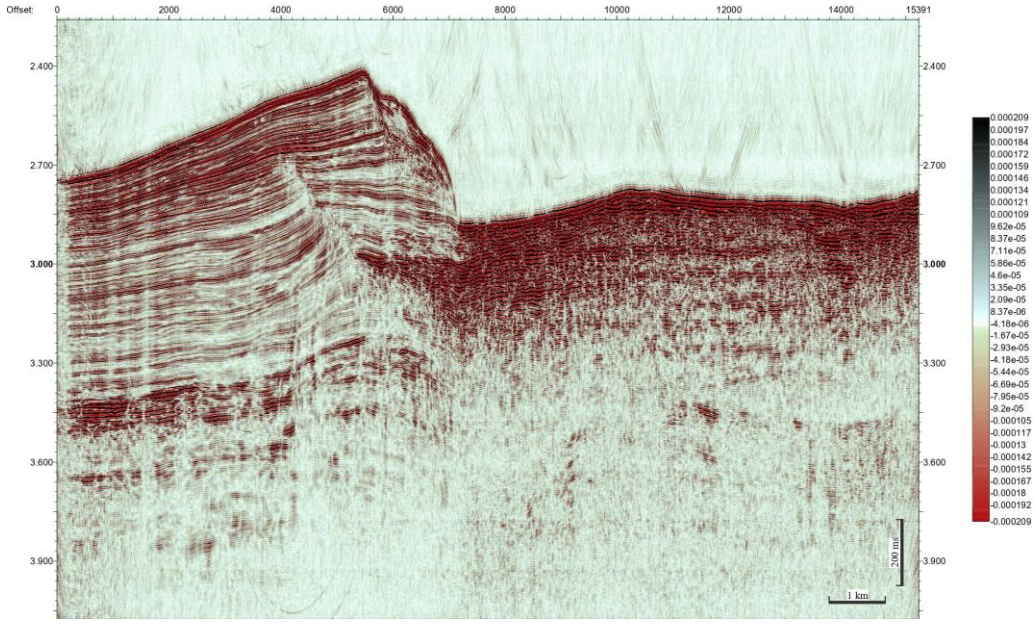

Appendix 12: Seismic section of Line M73-1-GeoB07-235

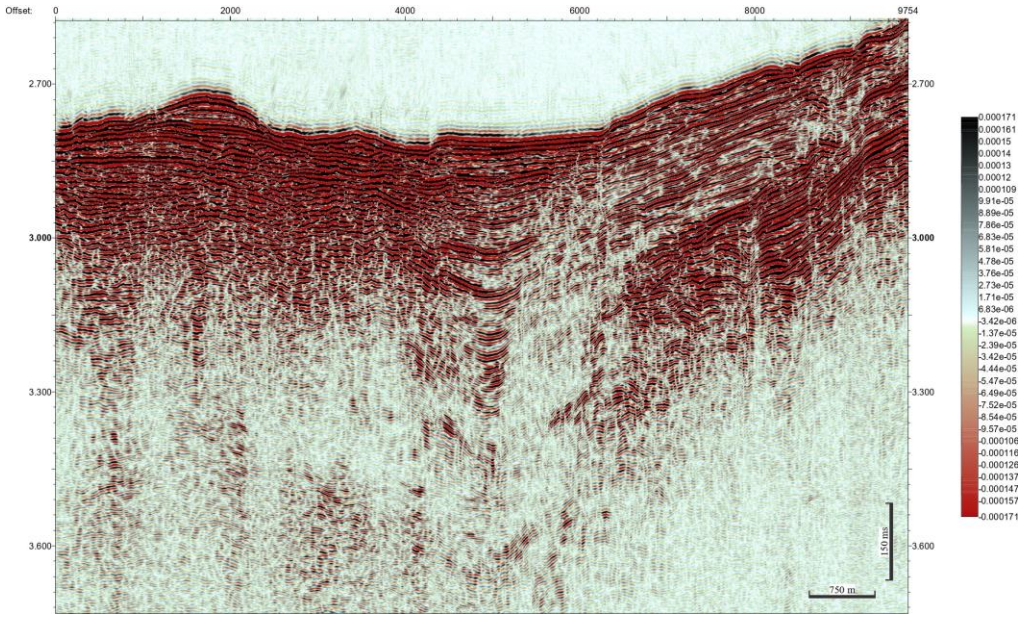

Appendix 13: Seismic section of Line M73-1-GeoB07-243

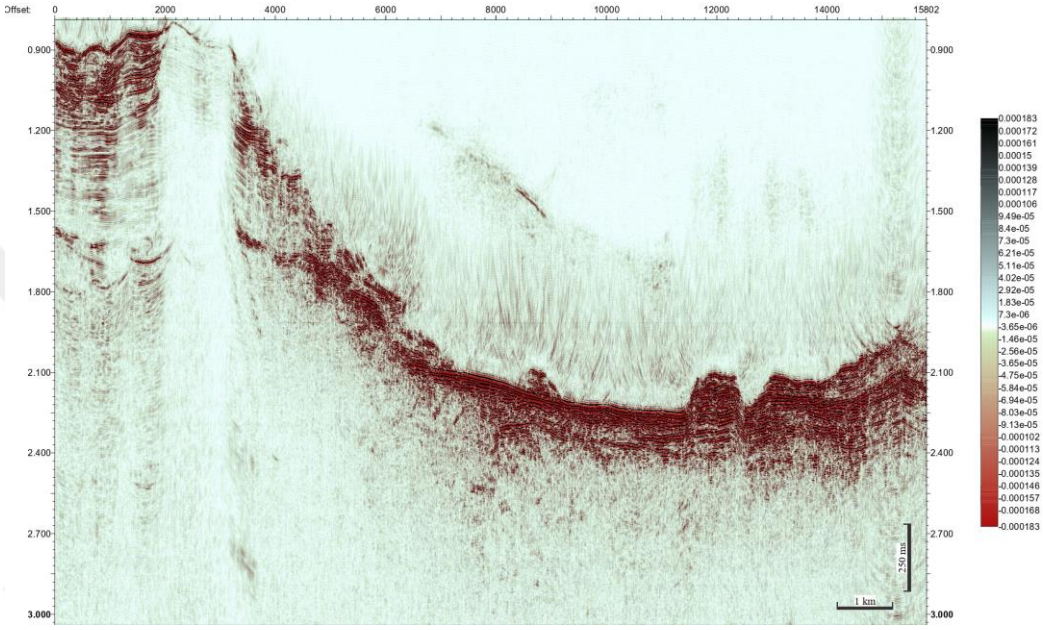

Appendix 14: Seismic section of Line M73-1-GeoB07-276

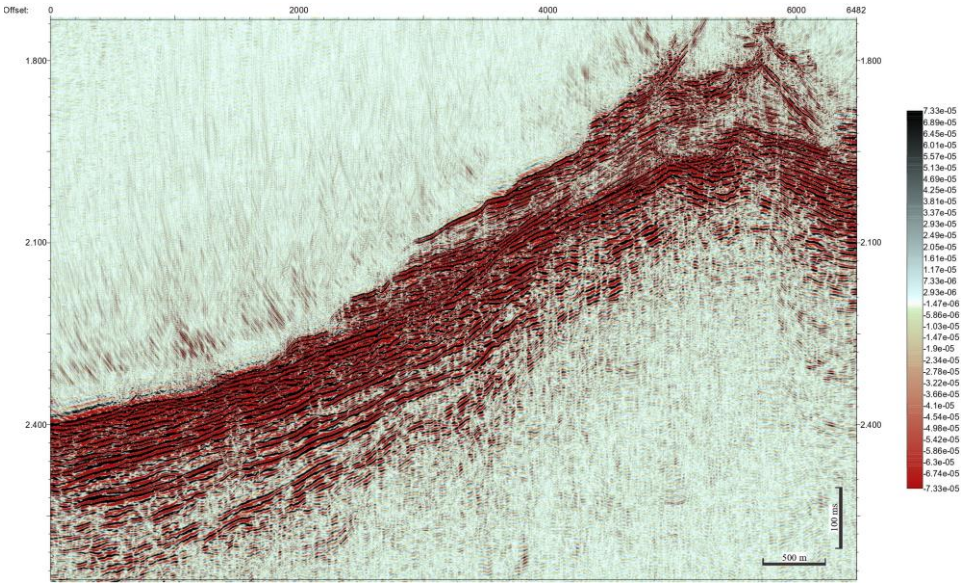

Appendix 15: Seismic section of Line M73-1-GeoB07-280

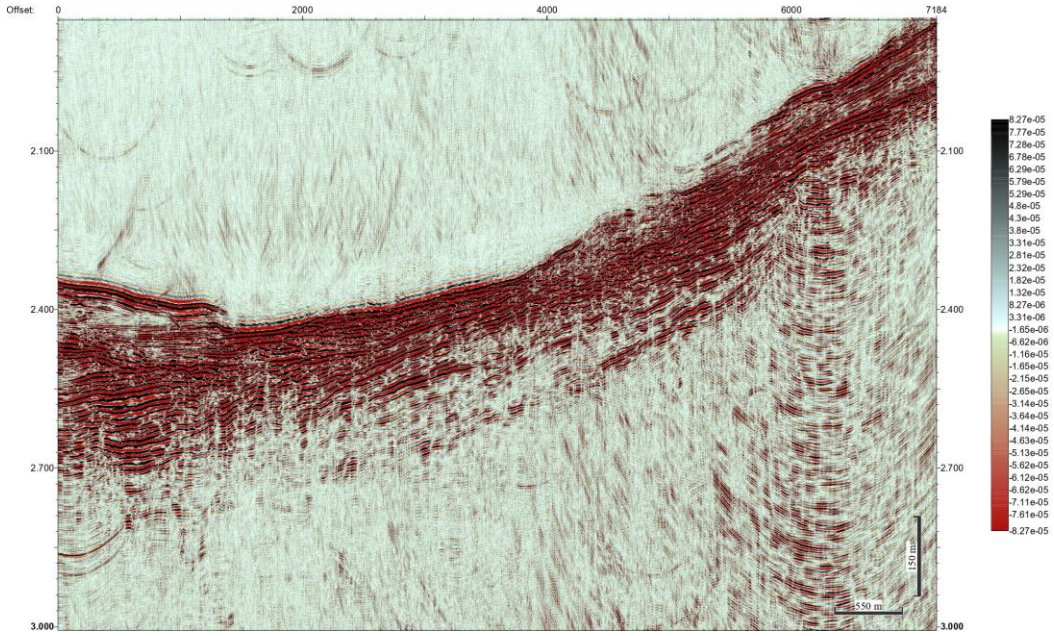

Appendix 16: Seismic section of Line M73-1-GeoB07-282

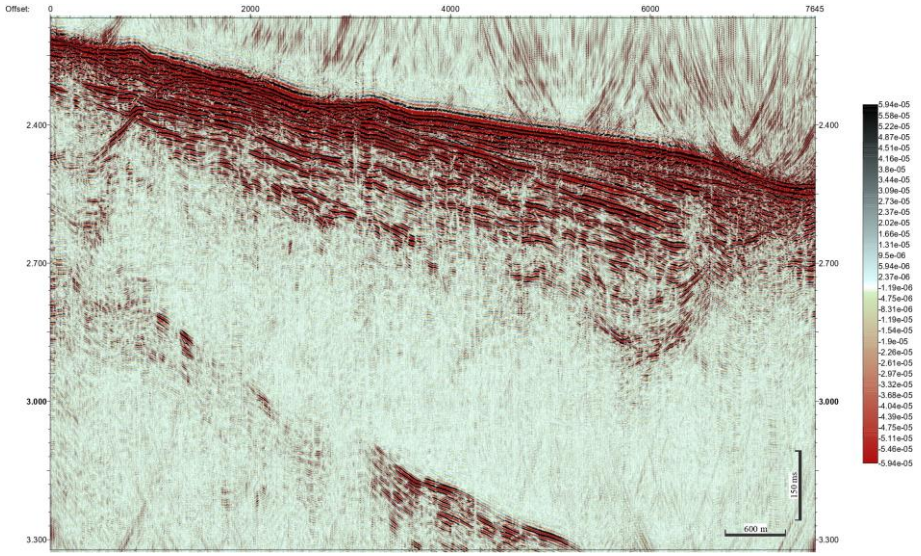

Appendix 17: Seismic section of Line M73-1-GeoB07-292

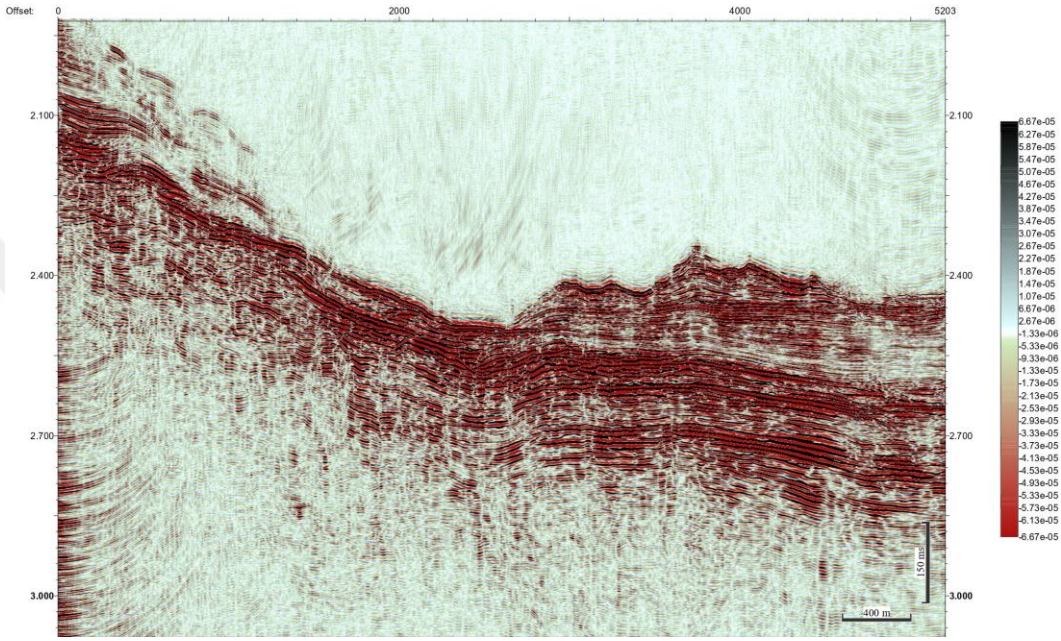

Appendix 18: Seismic section of Line M73-1-GeoB07-304

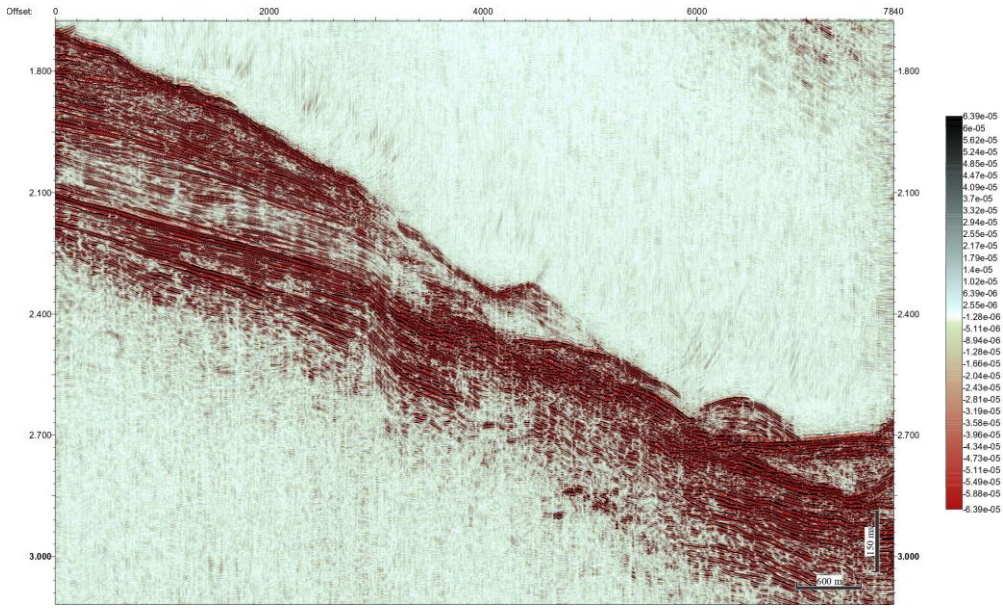

CURRICULUM VITAE

Name and Surname : Rashid Ahmadov

EDUCATION

B.Sc. : Azerbaijan State Oil and Industrial University

Petroleum Engineering

PROFESIONAL EXPERIENCE

- "Geologist / Subsurface Engineer" position at "Atkins Germany" from 01.05.2022 to present
- "Geophysical student assistant" position at "Fraunhofer-IWES" between 01.02.2022 – 30.04.2022 dates
- "Graduate Summer Intern" position at "SOCAR" between 02.07.2018 – 10.09.2018 dates
- "Production Engineering Intern" position in "SOCAR" between 30.01.2018 – 30.04.2018 dates
- "Field Engineer" position in "AzFEN" between 30.06.2017 – 04.09.2017 dates